Modeling and Application of Non-Uniform Engineering Structures Coupled with FGM and Piezoelectric Materials in Stability Enhancement and Energy Harvesting

by

Alireza Keshmiri

A Thesis submitted to the Faculty of Graduate Studies of

The University of Manitoba

in partial fulfilment of the requirements of the degree of

DOCTOR OF PHILOSOPHY

Department of Mechanical Engineering

University of Manitoba

Winnipeg, Manitoba, Canada

Abstract

Dynamic analysis of non-uniform beams with tapered geometry and functionally graded material properties to achieve a better design for stability enhancement and energy harvesting applications is the main interest and focus of this thesis.

A powerful and reliable theoretical model to derive the vibration response of nonlinearly tapered beams with axially functionally graded material properties within the framework of classical Euler–Bernoulli beam theory is developed and presented. The effect of geometry and material properties variation for different nonlinear profiles is comprehensively studied.

It is demonstrated that piezoelectric layers and their coupling effect in addition to the non-uniform geometry, significantly enhance the stability of the smart non-uniform beam. The effects of compressive follower force, geometry taper ratio, boundary condition, and external piezoelectric voltage on flutter and buckling capacities of the non-uniform beam are examined.

In addition, the model is also employed to present an analytical approach for development of a non-uniform piezoelectric energy harvester. It is applied to surface bonded piezoelectric beams with non-uniform geometry and material variation profiles to derive the dynamic response of the structure to external environmental excitations and efficiently harvest the subsequent mechanical vibration energy. It is proved that the non-uniform configuration improves the

electromechanical outputs. Additionally, an array of non-uniform harvesters is deployed to design a wideband piezoelectric energy harvesting system. It is shown that with the proposed formation, the system can optimally function over a wide frequency domain.

Lastly, two new energy harvester configurations by using piezoelectric stacks are analytically developed. By benefiting from in-plane piezoelectric polarization, electrical outputs compared to a conventional harvester are considerably improved. At the end, an initial optimization model by using simulation-based optimization technique and machine learning algorithms is presented.

Acknowledgment

I would like to deeply acknowledge the people whose contributions have made my graduate experience at the University of Manitoba a successful and great one.

Firstly, I am thankful to my knowledgeable supervisor Dr. Nan Wu. I would like to thank him for his support and guidance during the past three years. There are many things I have learned from him that I will treasure for the rest of my life.

Next, I really thank my committee members, Dr. Jun Yang, Dr. Young-Jin Cha, and Dr. Malcolm Xing. They gave me great support and guidance in the committee meetings, candidacy exam, and final oral defense.

I would like to thank my mom and dad for the sacrifices they made and their unconditional love. I would not be able to become who I am today without their support. I also thank my sister Arezoo for always being there for me and I wish her the very best throughout her life.

Finally, I would like to sincerely thank my best friend and also beautiful and lovely wife, Ghazal. Her warm and unconditional support and encouragement makes everything possible for me. She is the best thing ever happened to me.

This research is based upon work supported by the University of Manitoba, Research Manitoba, and Natural Sciences and Engineering Research Council of Canada (NSERC).

Contents

List of Tables

List of Figures

Fig. 6-26 GA convergence graph. (a) Base excitation frequency φ_1=100rad/s. (b) Base excitation frequency φ_2=200rad/s.

List of Abbreviations

FGM	Functionally Graded Material
FEM	Finite Element Method
ADM	Adomian Decomposition Method
AMDM	Adomian Modified Decomposition Method
PZT	Piezoelectric Zirconate Titanate
PVDF	Polyvinylidene Fluoride
PMN-PT	Lead Magnesium Niobate-Lead Titanate
MEMS	Micro Electromechanical System
SDOF	Single Degree of Freedom
FRF	Frequency Response Function
ANN	Artificial Neural Network
GA	Genetic Algorithm
RMS	Root Mean Square

List of Nomenclature

D	Electric displacement vector	Coulomb/m^2
e^{σ}	Dielectric permittivity tensor at constant stress	Farad/m
d^d	Direct piezoelectric coefficient tensor	Coulomb/N
d^c	Converse piezoelectric coefficient tensor	m/V
σ	Stress vector	N/m^2
ε	Strain vector	dimensionless
E_e	Electric field vector	V/m
S^E	Elastic compliance tensor	m^2/N
x	Position variable along length of the beam	m
t	Time variable	s
ρ	Mass density	kg/m^3
E	Young's elasticity modulus	N/m^2
A	Cross-sectional area	m^2
w	Transverse deflection	m
I	Second moment of area	m^4
L	Length	m
b	Width	m
h	Thickness	m

m	Geometrical taper ratio	dimensionless
β	Rigidity taper ratio	dimensionless
α	Density taper ratio	dimensionless
V	Electric voltage	V
K	Spring stiffness	N/m
Y	Base motion amplitude	m
φ	Base motion frequency	rad/s
j	Unit imaginary number	dimensionless
C_s	Strain rate damping coefficient	N.s/m
ω	Natural frequency	rad/s
ω_d	Damped frequency	rad/s
N_p	Total number of piezoelectric patches	dimensionless
C_p	Piezoelectric capacitance	Farad
r	Circular cross-section radius	m
R_L	Resistive load	Ω
η	Efficiency factor	dimensionless
P^e	Electric power	W

List of Copyrighted Materials

1. Section 2.1 and chapter 4 of this thesis are reproduced with some modifications from [A. Keshmiri, N. Wu, Q. Wang "Vibration analysis of a nonlinearly tapered cone beam using Adomian decomposition method", International Journal of Structural Stability and Dynamics, 18(7), 1850101, 2018] with permission from the "World Scientific Publishing Co Pte Ltd" and [A. Keshmiri, N. Wu, Q. Wang "Vibration analysis of non-uniform tapered beams with nonlinear FGM properties", Journal of Mechanical Science and Technology, 32(11), 5325-5337, 2018] with permission from the "Springer Nature". I hereby declare that this section of the thesis includes material that is the result of joint research. Dr. Nan Wu and Dr. Quan Wang assisted and supervised the work as I did the modeling and writing.
2. Section 2.3 and chapter 5 of this thesis are reproduced with some modifications from [A. Keshmiri, N. Wu "Structural stability enhancement by nonlinear geometry design and piezoelectric layers", Journal of Vibration and Control, 25(3) 695–710, 2019] with permission from the "SAGE Publications". I hereby declare that this section of the thesis includes material that is the result of joint research. Dr. Nan Wu assisted and supervised the work as I did the modeling and writing.

3. Section 2.4 and 6.1 of this thesis are reproduced with some modifications from [A. Keshmiri, N. Wu, Q. Wang "A new nonlinearly tapered FGM piezoelectric energy harvester", Engineering Structures, 173, 52-60, 2018] with permission from the "Elsevier B.V.". I hereby declare that this section of the thesis includes material that is the result of joint research. Dr. Nan Wu and Dr. Quan Wang assisted and supervised the work as I did the modeling and writing.

4. Section 2.4, 6.1, and 6.2 of this thesis are reproduced with some modifications from [A. Keshmiri, N. Wu "A wideband piezoelectric energy harvester design by using multiple non-uniform bimorphs", Vibration, 1(1), 93-104, 2018] with permission from the "MDPI". I hereby declare that this section of the thesis includes material that is the result of joint research. Dr. Nan Wu assisted and supervised the work as I did the modeling and writing.

5. Section 2.4 and 6.3 of this thesis are reproduced with some modifications from [A. Keshmiri, X. Deng, N. Wu "New energy harvester with embedded piezoelectric stacks", Composites Part B: Engineering, 163, 303-313, 2019] with permission from the "Elsevier B.V.". I hereby declare that this section of the thesis includes material that is the result of joint research. Dr. Nan Wu and Dr. Xiaowei Deng assisted and supervised the work as I did the modeling and writing.

6. Section 6.4 of this thesis is reproduced with some modifications from [A. Keshmiri, S. Bagheri, N. Wu "Simulation-Based Optimization of a Non-Uniform Piezoelectric Energy Harvester with Stack Boundary"]. This manuscript is in the preparation process. I hereby declare that this section of this thesis includes material that is the result of joint research with Shahriar Bagheri in the Sound & Vibrations Lab at the University of Manitoba. I worked on the mechanical modeling process and organization of the research work while Shahriar performed the optimization modeling and analysis. Dr. Nan Wu assisted and supervised the work.

Chapter 1

1 Introduction

Dynamic behavior of geometrically and materially non-uniform engineering structures because of capability to optimize weight and strength has numerous applications in various engineering and industrial fields such as mechanical, electrical, civil, aerospace, and marine. This research aims to provide a reliable analytical model capable of solving the governing dynamic equation of a nonlinearly tapered beam with axially functionally graded material (FGM) properties. Moreover, by coupling piezoelectric materials to the non-uniform structure, substantial improvement in stability behavior and also energy harvesting properties compared to the uniform smart beam can be achieved. For stability enhancement, the piezoelectric material is used as an actuator which induces local strain in the smart structure. As an energy harvester, the piezoelectric material acts like a sensor converting mechanical vibration into electrical energy.

In view of the above, this research presents a theoretical model to investigate the dynamic characteristics of non-uniform engineering structures with stability enhancement and vibration energy harvesting applications.

1.1 Thesis Objectives and Contributions

This thesis reports a reliable theoretical model for the free and forced vibration analysis of nonlinearly tapered piezoelectric coupled beams with axially FGM properties and general boundary conditions based on Euler–Bernoulli beam theory valid for any slender beam that allows ignoring shear deformation and rotatory inertia. First, the general non-uniform beam vibration model is used to study the flutter and buckling of a piezoelectric coupled beam with non-uniform geometry subjected to a compressive follower force. It is demonstrated that nonlinear tapered geometry along with the localized strain produced by embedded piezoelectric actuators, significantly improve the stability of the smart structure. The model is also employed to present an analytical approach for development of a non-uniform piezoelectric energy harvester. It is applied to surface bonded piezoelectric beams with nonlinear geometry and material variation profiles to derive the dynamic response of the smart structure and harvest the subsequent vibration energy. It is proved that the non-uniform pattern considerably increases the electromechanical outputs. Following the same idea and design philosophy, a group of non-uniform harvesters is suggested to design a wideband piezoelectric energy harvesting system. The proposed system can be generalized to different beam quantities and conversion principles to cover particular frequency ranges. Another design idea to increase the electrical outputs of conventional energy harvesters is to utilize piezoelectric stacks. Higher electrical voltage/charge output can be achieved from the in-plane polarization of piezoelectric elements. In addition, the suggested composite harvester with embedded piezoelectric stacks is more desirable for power harvesting from large forces. Based on the same idea, an optimized design of a piezoelectric energy harvester platform with piezoelectric stacks embedded in the base by using neural network and genetic algorithm is presented.

The main novelty of the research work is development of a mechanical model which has included non-uniform geometry and accounted for the variable material properties of the structure rather than a uniform and homogeneous configuration. The presented method is capable of delivering the analytical vibration mode shape functions and natural frequencies of a non-uniform piezoelectric coupled beam. For the first time in the literature, it is showed that nonlinear geometry coupled with the embedded piezoelectric actuators enhances the flutter and buckling capacities and hence improves the stability behavior of the structure. Moreover, once the non-uniform design coupled with piezoelectric sensors is used as an energy harvester, it can substantially increase the electromechanical outputs in a wide frequency domain. Lastly, two innovative energy harvester configurations by using piezoelectric stacks are developed and presented.

1.2 Thesis Organization

The thesis is organized to provide a brief review of the background and problem description, theoretical analysis and modeling process, design considerations, simulations and discussion, and lastly, the final outputs and results of the research.

Chapter 1 introduces the initial idea behind this research and also the objective of this work. Chapter 2 reviews the background and current practices related to the subjects of this study. Chapter 3 is about the basic mathematical model used and developed to efficiently solve the governing partial differential equation. Chapter 4 provides the theoretical free and forced vibration analysis of Euler-Bernoulli beam with nonlinearly tapered geometry and axially FGM properties. Chapter 5 presents the analytical stability analysis of a piezoelectric coupled beam with non-uniform geometry. Chapter 6 provides the comprehensive theoretical development of four different piezoelectric energy harvesting systems. First, the electromechanical solution of a non-uniform energy harvester is analytically presented. Then the model is used to design a broadband piezoelectric energy harvesting system capable of generating high electrical outputs over a wide frequency domain. To end the chapter 6, two new composite energy harvester configurations by using piezoelectric stacks are theoretically developed and presented. Finally, chapter 7 summarizes the report and briefly talks about the areas for future improvement.

Chapter 2

2 Backgrounds and Literature Review

In this chapter, first a brief review about vibration analysis of non-uniform engineering structures with a special emphasis on beams is provided. Then FGMs are thoroughly introduced and their background, mechanical properties, and applications are investigated. The concept of piezoelectric materials and their controllable effect on dynamic behavior of engineering structures is discussed. Next, research works on flutter and buckling analysis of non-uniform beams and columns are reviewed. Next, a broad survey on piezoelectric energy harvesting from ambient sources and various vibrational energy harvesters is presented. Lastly, existing constraints and issues are highlighted and the motivations behind this research work are explained.

2.1 Non-uniform Engineering Structures

Engineering structures with variable cross-sectional profile have abundant engineering and industrial applications due to weight and strength optimization capability. Therefore, vibration analysis of non-uniform beams with nonlinear tapered geometry and FGM properties in an effort to achieve a better design is of interest to many researchers [1]. The literature on the dynamic response of general non-uniform structures is limited. The review of previous works under two main categories of geometrically non-uniform beams and beams with FGM properties is followed.

2.1.1 Geometrically Non-uniform Beams

This section of the thesis is reproduced with some modifications from [A. Keshmiri, N. Wu, Q. Wang "Vibration analysis of a nonlinearly tapered cone beam using Adomian decomposition method", International Journal of Structural Stability and Dynamics, 18(7), 1850101, 2018] with permission from the "World Scientific Publishing Co Pte Ltd".

Modeling of non-uniform beams has been an interest to many researchers. For the very first time, a general solution for some cases of variable cross-section beams was presented where the depth and width are of the power function form [2]. Then the lateral vibration of bars with uniform and variable sectional area using integral method was investigated [3]. Later, an analytical solution for the motion differential equation of beams with constant depth and the width that varies in an exponential manner was obtained [4].

In the study of transverse vibration of cantilever non-uniform bars, upper and lower bounds for natural frequencies were introduced [5]. Bessel functions were also employed to find the solution for vibration of beams with different cross-sections and some specific tapering functions [6]. Mabie and Rogers did some work on the vibrational analysis of linearly tapered beams. They also solved the governing differential equation in terms of Bessel functions [7]. Klein presented a new method based on finite element method (FEM) and Rayleigh-Ritz analysis for free vibration analysis of beams with non-uniform characteristics. She estimated the continuous non-uniformity function by a step function for each substructure [8]. By using differential transform method and Hamilton's principle, the differential equation of motion for a linearly tapered rotary beam by coupling between bending and torsional vibration was obtained and solved [9]. For a linearly tapered beam element with various sectional shapes, Gupta derived displacement functions from the equation of motion and calculated stiffness and mass matrices [10]. Lee et al. presented an integral form solution for the dynamic response of a linearly tapered beam by using the Green function in Laplace transform domain [11]. Similarly but based on Frobenius method, a direct solution to the mode shape function of Euler-Bernoulli beam with wedge and cone geometry was found [12]. Furthermore, general elastic ends were introduced to the vibration problem and it was solved with differential transformation method [13].

In addition, vibration analysis of an exponentially tapered beam along the width with constant thickness was investigated by defining an upper bound for bending natural frequencies [14] and introducing the tip mass effect [15]. Recently, the eigenvalue problem of a non-uniform beam using collocation technique based on Bernstein pseudospectral approach was solved [16] and also a size-dependent formulation for beams with nonlinear geometry variation was developed based on the second strain theory [17]. In summary, dynamic response of linearly non-uniform beams has been investigated using many different numerical methods. However, most of them like Klein's approach [8] need domain discretization and dealing with bulky systems of equations [11].

An important problem to deal with in the vibration analysis is the physically correct solution of a nonlinear system modeled by ordinary or partial differential equations [1]. The mathematical model used and developed in this research is based on Adomian decomposition method (ADM). ADM is intended to solve partial differential equations avoiding the restrictive assumptions or linearization to allow solutions of more realistic models [18]. A few researchers utilized the same methodology to derive the vibration response of beams. Lately, Adomian modified decomposition method (AMDM) was used for the vibration analysis of a linearly tapered Euler-Bernoulli beam [19]. Furthermore, solutions to eigenvalue vibration problem of a uniform beam under various end conditions [20] and a multi-stepped beam [21] based on ADM were proposed.

From the above review, it is clear that different models and methods were proposed to study the vibration response of tapered beams with simple geometrical variations. However, non-uniform beams with a general geometry variation function are not analytically investigated [1].

2.1.2 Functionally Graded Materials

This section of the thesis is reproduced with some modifications from [A. Keshmiri, N. Wu, Q. Wang "Vibration analysis of non-uniform tapered beams with nonlinear FGM properties", Journal of Mechanical Science and Technology, 32(11), 5325-5337, 2018] with permission from the "Springer Nature".

FGM is a relatively new type of material characterized by continuous variation of material properties along desired spatial directions which are designed to achieve an effective functional performance. FGM structures due to their capability to optimize weight, strength, and stability have significant applications in various engineering fields [22].

Japanese scientists endeavour in order to find thermal barrier materials led to FGMs in 1984 [23]. Due to the smooth variation of mechanical properties in one or more directions, FGMs allow preserving high specific stiffness and avoiding the main disadvantages of composite laminates like delamination caused by strain singularity between two totally different materials [22]. Because of many advantages over the classical composites, FGMs have attracted huge attentions in modern industries [24]. Typically, they are a combination of ceramics and different metals [25]. Although there are many research studies on elasticity theory of plates and shells with FGM properties, the literature on the vibration analysis of FGM beams is quite limited [26].

For axially FGM beams with uniform geometry, a few studies working on free vibration analysis [27] and stability analysis [28] of exponentially graded beams exist. By expanding the mode shape function as a power series, a closed-form vibration solution for uniform beams with axially polynomial inhomogeneity in density and elasticity [29] and a new approach by using Fredholm integral equations to analyze linearly tapered and axially FGM beams [30] were introduced. Additionally, vibration response of axially FGM and linearly tapered beams by using FEM [31], [32] and differential transform method [33] was studied and presented. Recently, Fang and Zhou used Chebyshev polynomials as the admissible functions in the Ritz method and studied the free vibration of linearly tapered and axially FGM rotating beams [34].

Previous studies in the literature clearly indicate the importance of vibration analysis of structures with variable geometry and material properties. Although a few studies on the vibration behavior of axially FGM beams with uniform and linearly tapered geometries were conducted, no analytical model was introduced to obtain the vibration response of nonlinearly tapered beams with FGM properties. Here, axially material properties variation is also added to the governing equation.

2.2 Piezoelectric Materials

The crystalline structure of piezoelectric materials allows them to convert external mechanical strain into electrical polarization (direct piezoelectric effect) and conversely transform an applied electrical polarization into mechanical strain (reverse piezoelectric effect). Piezoelectric crystals are composed of positive and negative ions in an alternating fashion. For instance, in the case of Quartz, Oxygen atom is a little bit negatively charged and Silicon atom is a little bit positively charged. The average of all the positive and negative charges is in the middle (center of charge). When the crystal is unstressed, the charges cancel each other out. However, by applying tension or compression, positive and negative charges will shift in opposite directions. As a result, the electric potential is generated.

Intensive research on piezoelectric materials has led to great amount of industrial and manufacturing applications for both direct and reverse piezoelectric effects. Different kind of sensors, detection tools, contact microphones, and microbalances are only a few examples of direct piezoelectric effect. Additionally, the direct piezoelectric effect provides the opportunity to harvest ambient mechanical energy and convert it into usable electrical energy to supply electronic devices. On the other hand, some examples of reverse piezoelectric effect are piezo motors, loudspeakers, scanning microscopes, and ultra-exact positioning systems.

Piezoelectric materials can be categorized to four groups: single crystals, ceramics, polymers, and composites. Generally, single crystals and ceramics have superior piezoelectric properties. In contrast, piezoelectric polymers exhibit more flexibility and wider applications. Last but not the least, piezoelectric composite materials possess a combination of ceramics and polymers electromechanical properties [35].

2.2.1 Conventional Piezoelectric Materials

Currently, the most common piezoelectric material used in energy harvesting is a piezoceramic called lead zirconate titanate, also known as PZT. Normally, piezoceramics have large electromechanical coupling coefficients with high energy conversion rate. However, they are extremely brittle with limited applications. Another well-known piezoelectric material is polyvinylidene fluoride known as PVDF. It is a piezoelectric polymer with substantial flexibility compared to PZT [36]. Piezopolymers have smaller electromechanical coupling coefficients than piezoceramics but they are lighter and more flexible which makes them resilient to large structural deformation, mechanical impact, and shock. Flexible piezoelectric materials are appealing for energy harvesting applications due to large strain capacity that provides more mechanical energy available for conversion to electrical energy.

Typically, piezoceramics are used as actuators and piezopolymers act as sensing materials [37]. But in the case of self-sensing actuators, it is likely to use piezoceramics as well [38], [39]. On the other hand, piezoelectric single crystals like lead magnesium niobate-lead titanate (PMN-PT) due to highly ordered positive and negative ions arrangement have superior piezoelectric characteristics. However, crystal-based energy harvesters are still not very popular because of high cost and brittle structure [35].

2.2.2 Piezoelectric Composite Materials

Normally, a uniform piezoelectric material with an electrode pattern and polling direction toward its thickness (perpendicular to strain axis) is used for energy harvesting. As mentioned, conventional piezoelectric ceramics are extremely brittle. Furthermore, when the actuation and polling directions are aligned, piezoelectric material performs much better. These two major limitations of uniform piezoceramic materials can be eliminated by employing piezoceramic fibers inserted in a polymer matrix. Piezoelectric composites consist of piezoceramic materials in the shape of particles, fibers, and rods embedded in polymer matrix. These new piezoelectric materials are called piezofiber composites and are being developed to overcome many practical restrictions of conventional piezoelectric devices [40], [41], [42]. Piezofiber composites can be fabricated with aligned strain and polling directions and also they have significant flexibility and damage robustness [43].

2.2.3 Constitutive Relations

The constitutive relations for piezoelectric materials are formulated as,

$$D_i = e^{\sigma}_{ij} E_{e\,j} + d^{d}_{im} \sigma_m, \tag{2-1}$$

$$\varepsilon_k = d^{c}_{jk} E_{e\,j} + s^{E}_{km} \sigma_m, \tag{2-2}$$

where D is the electric displacement vector (Coulomb/m^2), e^{σ} is the dielectric permittivity tensor at constant stress (Farad/m), d^d and d^c are direct and converse piezoelectric coefficient tensors (Coulomb/N or m/V), σ is the stress vector (N/m^2), ε is the strain vector (dimensionless), E_e is the external electric field vector (V/m), and s^E is the elastic compliance tensor (m^2/N) [37], [44].

Eq. (2-1) is the sensor equation resulted from direct piezoelectric effect. The piezoelectric sensor under a mechanical stress filed, generates electrical charge. Eq. (2-1) without the coupling term is just the dielectric equation. On the other hand, Eq. (2-2) is the actuator relation based on the reverse piezoelectric effect. Similarly, by neglecting the coupling term, Eq. (2-2) is simply the Hook’s law.

Generally, the elastic compliance matrix is like,

$$S^E = \begin{bmatrix} S_{11} & S_{12} & S_{13} & 0 & 0 & 0 \\ S_{21} & S_{22} & S_{23} & 0 & 0 & 0 \\ S_{31} & S_{32} & S_{33} & 0 & 0 & 0 \\ 0 & 0 & 0 & S_{44} & 0 & 0 \\ 0 & 0 & 0 & 0 & S_{55} & 0 \\ 0 & 0 & 0 & 0 & 0 & S_{66} \end{bmatrix}. \tag{2-3}$$

The dielectric permittivity matrix is of the form,

$$e^{\sigma} = \begin{bmatrix} e_{11}^{\sigma} & 0 & 0 \\ 0 & e_{22}^{\sigma} & 0 \\ 0 & 0 & e_{33}^{\sigma} \end{bmatrix}. \tag{2-4}$$

And the stress vector is like,

$$\sigma = \begin{bmatrix} \sigma_{11} \\ \sigma_{22} \\ \sigma_{33} \\ \sigma_{23} \\ \sigma_{31} \\ \sigma_{12} \end{bmatrix} = \begin{bmatrix} \sigma_1 \\ \sigma_2 \\ \sigma_3 \\ \sigma_4 \\ \sigma_5 \\ \sigma_6 \end{bmatrix}. \tag{2-5}$$

For a piezoelectric sheet, the polling direction is along the thickness which is symbolized by 3-axis and also 1 and 2 axes are in the plane of the sheet. The piezoelectric coefficient tensor is presented as,

$$d = \begin{bmatrix} 0 & 0 & d_{31} \\ 0 & 0 & d_{32} \\ 0 & 0 & d_{33} \\ 0 & d_{24} & 0 \\ d_{15} & 0 & 0 \\ 0 & 0 & 0 \end{bmatrix}. \tag{2-6}$$

This work focuses on two different applications of piezoelectric materials in stability enhancement and energy harvesting. For stability enhancement, the piezoelectric material functions as an actuator which exhibits mechanical deformation when an external electrical field is applied. Bonding or embedding segmented piezoelectric elements in a structure allows the application of localized strain through which the deformation of the whole structure can be controlled [45]. On the other hand, the direct piezoelectric effect is employed for harvesting the ambient mechanical vibration energy and transforming it into electrical energy to supply smart integrated systems [46].

2.3 Structural Stability Enhancement

This section of the thesis is reproduced with some modifications from [A. Keshmiri, N. Wu "Structural stability enhancement by nonlinear geometry design and piezoelectric layers", Journal of Vibration and Control, 25(3) 695–710, 2019] with permission from the "SAGE Publications".

In the theory of elastic stability, which was initiated by Euler, it is assumed that for small axial loads applied on an elastic body, the equilibrium is stable. The whole system is in stability condition up to the point of bifurcation. Subsequently, the primary form of equilibrium turns into an unstable situation [47]. Flutter and buckling are the two leading forms of instability in beam and column structures. Flutter instability corresponds to the limitless increasing of vibrational amplitude occurring beyond a critical airflow speed and causing negative system damping [48] because of interaction of two modes in the system [49]. On the other hand, buckling is a sudden lateral deflection which may occur at a certain critical compressive force even though the stresses in the structure are well below the failure strength of the material [50].

Flutter and buckling analysis of beams or columns has been of interest in the literature of structural mechanics for a large amount of time. Flutter is immense aeroelastic instability for aircraft, wing, and missile structures [48] and same as buckling could result in a catastrophic failure of aeronautical, mechanical, and civil structures [50]. Stability analysis of a uniform column subjected to a follower (tangential) force has attracted much attention as a classical applied mechanics problem. For the very first time, the stability of a cantilever uniform column under a follower compressive force at the free end was investigated [47]. Additionally, some studies considered the structural stability of tapered or stepped members. Non-uniform beams and columns are extensively used in many engineering applications to reach an optimal strength and weight distribution and also to fulfil architectural and functional design desires [50].

Early researches on stability of non-uniform members are mainly focused on linearly tapered beams and columns [50]. As one of the early works in the area, the parametric instability of a beam with linearly variable cross-sectional thickness was studied theoretically and experimentally [51]. Moreover, a numerical method by using energy approach was developed to approximate a lower bound buckling load [52] and then a semi-analytical method based on numerical integration for linearly tapered Beck's columns was introduced [53]. Following these research works, stability of multi-step columns subjected to concentrated and distributed forces was resolved using transfer matrix method [54].

Recently, buckling analysis of linearly web tapered I-beams has been of interest to many researchers by using power series method [55], Ayrton–Perry formulation [56], and FEM [57], [58]. Based on FEM, stability analysis of linearly tapered beams along thickness and width by using various methodologies were also presented [59], [60], [61]. Furthermore, stability analysis of linearly tapered Timoshenko beams is formulated based on transfer matrix and numerical approaches [62], Forbenius method [63], and iterative variational Rayleigh–Ritz method [64].

Smart materials such as piezoelectrics and shape memory alloys have abundant stability enhancement applications. Piezoelectric materials because of active electromechanical characteristics have received more attention and been used tremendously [50]. As an early works in this field, stability analysis of piezoelectric bounded columns by using difference method was formulated to study the flutter and buckling capacity enhancement [49] and crack effect on stability of beams [65]. In order to repair a delaminated vibrating beam, the electromechanical properties of piezoelectric materials were employed to produce a local shear force above the delamination area via an external voltage [66]. Wang and Wu have done a comprehensive review on structural enhancement and repair approaches by piezoelectric materials and shape memory alloys [67].

The literature review shows that there is a few published material in the literature related to the stability problem of non-uniform beams under tangential axial force. However, no analytical consideration is given to beams with nonlinear variable cross-section and attached piezoelectric layers. With the non-uniform geometry and the piezoelectric materials actuation effect, the stability of the smart structure can be considerably enhanced [50].

2.4 Piezoelectric Energy Harvesting

Over the past few decades, the advancement of electronic devices has led to increase in power usage and decrease in battery life that restricts the functionality of electronic devices. In order to extend the electronics life, many researches are being conducted to acquire the needed electrical energy from the environment. Therefore, alternative new, safe, inexpensive, efficient, and green energy sources are essential.

Power harvesting is the fundamental step toward self-powered systems in the current electronics marketplace. Recently, development of micro energy harvesting technologies as an alternative for the conventional batteries has attracted great amount of attention. This micro energy harvesting technology is benefiting from mechanical vibration, mechanical and thermal stress or strain, sun or room light, and human body motion that can generate μW to mW power levels [68]. Some of these energy harvesters are designed to convert the environmental energy sources into usable power form to supply small electronic systems throughout the device lifetime [46]. Although the electrical power generated by these portable energy harvesting devices are still small, the idea gives a new and alternative direction to collect renewable energy from the environment in an easier and more cost-effective way. Great number of such devices can provide considerable power supply for certain needs.

Conversion of ambient energy into electrical energy is accomplished through electromagnetic induction, electrostatic generation, and piezoelectricity [36]. Several studies comparing the performance of these energy conversion methods are published investigating the most efficient energy generation approaches [69], [70], [71], [72]. Despite the fact that the mentioned methods can deliver valuable amount of energy, piezoelectric materials because of small size, custom shape fabrication ability, ease of system integration, and high-power conversion potential have received the most attention [38], [73]. In addition, piezoelectric energy harvesters require no voltage source [69], produce high voltage and low current [74], can harvest energy for all size systems [70], and yield a high electrical power density [71].

2.4.1 Vibration-Based Energy Harvesting

This section of the thesis is reproduced with some modifications from [A. Keshmiri, N. Wu, Q. Wang "A new nonlinearly tapered FGM piezoelectric energy harvester", Engineering Structures, 173, 52-60, 2018] with permission from the "Elsevier B.V.".

As mentioned earlier, energy harvesting from the ambient energy sources has become a dynamic research field and received so much attention in recent years. With decreasing electrical power requirements in wireless electronics and increasing utilization of sensors in different structures, energy harvesting to power sensors at the location without batteries limitations is appealing for various engineering automation and monitoring systems during the sensor lifetime [46].

Alternatively, vibration-based energy scavenging is becoming more attractive due to the fact that vibrational energy unlike other energies could be continuously harnessed beyond time and place limitations [46]. Conversion of mechanical vibration energy into electrical energy can be achieved through three conversion mechanisms: electrostatic, electromagnetic, and piezoelectric [75]. Although electrostatic approach is good for micro electromechanical systems (MEMS), power output level is not efficiently high. Additionally, electromagnetic transduction is not a good choice for small smart systems because of the coils [76].

In opposition, piezoelectric materials have several advantages for vibration power harvesting and are frequently utilized in smart structures as sensors and/or actuators [38]. The direct piezoelectric effect is suitable for harvesting ambient vibration energy and converting it into electrical energy form to power smart integrated systems [77]. Furthermore, even a small external excitation leads to considerable amount of generated voltage without requiring any low-efficient initiation mechanical mechanism [78].

There is huge number of research and review papers that investigated vibration-based piezoelectric energy harvesting from various points of views [35], [36], [79], [80]. Piezoelectric energy harvesters have numerous variable properties that can be controlled and changed to produce electrical energy from the environmental vibration. Most of current research works are focused on efficiency improvement through physical and geometrical configuration, circuitry design, and energy removal techniques. The problem that still needs to be studied and solved is generating sufficient energy to efficiently power the electronic devices.

2.4.2 Energy Harvester Configurations

This section of the thesis is reproduced with some modifications from [A. Keshmiri, X. Deng, N. Wu "New energy harvester with embedded piezoelectric stacks", Composites Part B: Engineering, 163, 303-313, 2019] with permission from the "Elsevier B.V.".

Piezoelectric materials can be configured in many various shapes advantageous for energy harvesting [81]. The composite configuration is the most common and well-known one. A composite structure is an arrangement made from two or more constituent materials with significantly different physical and/or chemical properties. The combination yields a material with characteristics different from the individual components with various specific assets.

A large portion of conventional energy harvester designs are unimorph or bimorph composite structures. A unimorph energy harvester consists of a single piezoelectric layer mounted on a metallic structure. On the other hand, two piezoelectric films with a metallic layer sandwiched between them create a bimorph energy harvester [81]. These two piezoelectric composite energy harvesters operate in the bending mode where the strain direction is perpendicular to the piezoelectric element polling direction using the piezoelectric coefficient d_{31}. There is also another well-known composite piezoelectric design with the stack configuration where strain and piezoelectric polling directions coincide using the piezoelectric coefficient d_{33} that is normally larger than d_{31} [81].

As one of the primary research in this area, Umeda et al. [82] studied the fundamentals of piezoelectric generators and suggested a system that converts mechanical impact into electrical energy through a piezoelectric vibrator. It was demonstrated that the energy efficiency increases with higher mechanical quality factor, bigger electromechanical coupling coefficient, and lower dielectric loss. Then, a device was proposed that generated electricity when exposed to a vibrating environment [83]. Their generator consisted of a mass, damper, and spring which the theoretical model was based on the single degree of freedom (SDOF) approach.

Later, many different energy harvester configurations were developed to effectively improve the efficiency and power generation. A uniform cantilever beam with surface bonded piezoelectric elements transversely vibrating is the most common harvester design. A cantilever energy harvester has a simple structure and provides large strain distribution over the piezoelectric layers. In the beginning, to simply obtain the electrical outputs and simplify the optimization process, SDOF model was used [84], [85], [86]. However, based on Erturk and Inman [87], the prediction error of the relative motion at the tip of the beam as well as the electrical power output is high. It is even worse for higher vibration modes. Consequently, SDOF method requires a correction factor.

As a result, in order to precisely and efficiently model the electromechanical outputs of piezoelectric energy harvesters, it is necessary to use more accurate models that also help to prevent charge cancellation phenomenon [87].

2.4.3 Unimorph Energy Harvester

Many piezoelectric energy harvesters consist of a single piezoelectric layer attached to a host structure, referred to as a unimorph. Johnson et al. [88] presented the design methodology of a unimorph piezoelectric cantilever harvester for transforming machine vibration into electrical energy in order to supply electronic devices with small power requirements. Afterward, a unimorph cantilever energy harvester was fabricated and also an FEM model for low frequency (5-10Hz) energy harvesting applications was developed [89]. The measurements correlated with the finite element results within 12% for resonant frequency and 2% for the output voltage. Furthermore, a unimorph cantilever piezoelectric harvester with different piezoelectric and non-piezoelectric sizes was theoretically examined [90]. They showed that when non-piezoelectric to piezoelectric size ratio is larger than one, maximum open circuit induced voltage could be achieved. On the other hand, the maximum electric power happened at equal non-piezoelectric and piezoelectric lengths.

Later, a small size hybrid vibration-based energy harvester for the human walking motion was designed and presented [91]. Their harvester consisted of a unimorph cantilever and two permanent magnets which transforms the low frequency human movement to high frequency resonance vibration of the harvester. Finally, the mechanical energy provided through human walking is converted to the electric energy. Recently, an interdigitated electrode unimorph piezoelectric cantilever generator is fabricated [92]. Their energy harvester is a laminated structure composed of ten PZT sheets with double and multiple-layer interdigitated electrodes working in the longitudinal vibration mode. The final results implied that embedding more interdigitated electrode layers in the PZT laminate could enhance the energy harvesting performance.

2.4.4 Bimorph Energy Harvester

Another common piezoelectric configuration is bimorph which includes a metallic layer sandwiched between two piezoelectric films. Bimorph piezoelectric cantilevers are often used because they can double the energy output without a major device volume growth [35].

Sodano et al. [93] presented a model investigating a piezoelectric bimorph cantilever beam in bending. The bimorph energy harvester subjected to base excitation estimated the power output accurately. Moreover, a self-powered piezoelectric sensor under vibration was developed [94]. They compared three common types of bending piezoelectric energy harvesters: unimorph, bimorph with series triple layers, and bimorph with parallel triple layers. The comparison of the results indicated higher power generation of unimorph harvester at low excitation frequencies and series triple layers at high excitation frequencies. After that, a bimorph harvester with proof mass working in the flexural mode was analytically studied and energy conversion performance was evaluated [95]. Their numerical results illustrated better power generation with particular physical and geometrical adjustments.

Erturk and Inman presented a closed-form analytical solution for a bimorph cantilever energy harvester with series and parallel connections of piezoceramic elements [96]. They experimentally validated the analytical model of the bimorph structure with a tip mass. Bimorph piezoelectric harvesters have huge applications in energy harvesting field and have attracted great amount of attention in recent years. Various mathematical models for bimorph piezoelectric harvesters are being reported to accurately derive the electromechanical outputs of the structure.

Energy harvesting from ambient fluid flows has also drawn considerable attention. One traditional energy source is wind flow which has been harvested for many years by windmills. But wind flow energy harvesting by piezoelectric materials is a new concept. Inspired by windmill structure, a piezoelectric windmill for electrical energy generation from wind by using bimorph harvesters was suggested [97]. Under a regular wind flow and vibration frequency of 6Hz, power level of 10.2mW was reported. Moreover, a piezoelectric bimorph cantilever attached to a flow disturbing object was analytically modelled in which the driving force for the oscillation is generated by von-Karman vortex street [98]. For the airflow of 35m/s, maximum voltage output of 0.83V and power output of 0.1mW was achieved.

Water flow is another source of energy provided by the environment. In order to effectively harvest the flowing water energy, a piezoelectric bimorph to transform the oceans and rivers flow energy into electrical power was presented [99]. Their piezoelectric bimorph used vortex shedding phenomenon and the generated voltage for a water velocity of 0.5m/s was reported 3V. A numerical model which can be used as a piezoelectric polymer wave energy generator was also presented [100]. The interaction of fluid and structure was coupled with piezoelectric materials. The vibration of the bimorph structure fixed at the ocean ground was achieved through wave motion and pressure difference.

A rectangular cantilever beam with surface bounded piezoelectric layers is the most common structure for piezoelectric energy harvesters. Although cantilever energy harvesters have demonstrated effective and efficient power harvesting applications, many other composite configurations have also been investigated to further improve the efficiency. Roundy et al. [101] indicated that a trapezoidal profile can distribute the strain evenly such that maximum strain is obtained at every point in the piezoelectric energy harvester. They have stated that a harvester with trapezoidal geometry can generate more than twice energy than a harvester with rectangular shape [46]. Moreover, Mateu and Moll [102] analytically compared different rectangular and triangular shaped cantilever bimorph energy harvesters to generate electrical power from walking type excitation. By doing experimental tests, it was determined that an energy harvester with trapezoidal geometry can produce 30% more power compared to the rectangular one [103]. This research aims to design an optimally efficient and cost-effective non-uniform energy harvester that maximizes the generated electrical energy from ambient mechanical vibration [46].

2.4.5 Stack Energy Harvester

This section of the thesis is reproduced with some modifications from [A. Keshmiri, X. Deng, N. Wu "New energy harvester with embedded piezoelectric stacks", Composites Part B: Engineering, 163, 303-313, 2019] with permission from the "Elsevier B.V.".

All the above energy harvesters are using the structural bending to enlarge the strain generated in piezoelectric materials. However, the strain induced by bending is perpendicular to the polling direction of piezoelectric layers and the harvester uses out-of-plane piezoelectric coefficients to generate the electrical energy. It should be noted that d_{31} is usually the lowest piezoelectric coefficient in the constitutive equation of most piezoelectric materials, which limits the energy harvesting efficiency of such harvesters. In addition, the reciprocating bending moment generates both tensile and compressive stresses in the piezoelectric material. As discussed earlier, piezoelectric ceramics with high piezoelectric coefficients are brittle and handle low tensile stress although their compressive strength is very high. In this case, the low durability of traditional harvester designs can be a serious problem with relatively large vibration amplitudes that is expected to obtain high power output.

In order to overcome the first drawback, there is another energy harvester design with the stack configuration, where strain and piezoelectric polling directions are aligned making good use of the in-plane piezoelectric coefficients [81]. Goldfarb and Jones [104] presented one of the primary works in this area and analyzed the electric energy generation efficiency of the piezoelectric stack configuration. They showed that maximum efficiency happens at low frequency, high amplitude, and large load resistance. Then, a theoretical analysis of power generation for PZT wafers stacked in series was presented and the model was verified with simulation and compression tests [105]. An application of the analysis was presented by energy generation inside a knee implant prototype. They concluded that the stack configuration makes it easier to manage the voltage output and resistive load. A stochastic approach using stack configuration for energy harvesting under broadband random excitations was also proposed [106]. They analytically analyzed two cases, harvesting electrical circuit with and without inductor. To maximize the harvested power, they proved that the mechanical damping in the harvester should be minimized and the electromechanical coupling should be as large as possible.

Recently, a piezoelectric stack harvester with a curved force amplification frame and negative tilting angle to convert walking force into electricity was presented [107]. The proposed design can reduce manufacturing complexity, buckling risk, and a large potential energy loss. Compared to an individual piezoelectric stack, their experiments indicated 8 times larger voltage and 112 times larger power outputs. Following the complex harvesters design trend, a flex-compressive piezoelectric energy harvester cell for compressive forces with high load carrying capability was proposed [108]. Their design can be used for large load environments such as highways and railways. Finally, a multilayered stack design that converts the distributed low frequency mechanical excitation energy into electrical energy was lately investigated [109]. Their model allowed accurate estimation of the limiting performance of PZT stack harvesters at various operating conditions.

By stacking a large number of thin piezoceramics together, the structure is more robust and can benefit from the higher coupling coefficient, d_{33}. The stack configuration is suitable for power harvesting from large forces. However, it also has some drawbacks. Typically, the stack configuration has high mechanical stiffness which makes straining of the material a challenge. The commonly used stack configurations are with either less stress/strain generated on piezoelectric elements or complex structure design to gain large stress/strain and power output. A new design combining structural bending and stack piezoelectric element can help to easily realize the large strain, high power output, and good structural reliability as an advanced piezoelectric energy harvester [81].

As can be seen, there is huge number of piezoelectric energy harvester designs to transform the vibrating or moving objects mechanical energy to electrical energy required for small electronic devices. There has been a huge focus on refining the energy harvesters' efficiency by physical and geometrical modifications.

2.5 Discussion, Motivation, and Objectives

From the literature review and to the best knowledge of the author, non-uniform beams with arbitrary nonlinear functions describing the variation of width, thickness, elasticity modulus, and density of the beam along axial direction has not been analytically investigated. Unlike the traditional methods and numerical techniques with linearization, perturbation, approximation, and discretization which all of them lead to huge numerical computations, presented model based on ADM provides the closed-form series solution of vibration mode shapes. Moreover, for simplification of the calculation procedure, a modification in the mathematical process is suggested and applied. This proposed alteration in the

ADM calculation procedure, makes it much more efficient computationally. Compared with earlier models, the main importance of this research can be justified by its generality for beam design and its computational simplicity.

For the stability enhancement purpose, the literature review shows no analytical consideration given to the beams with a nonlinear variable profile. The proposed non-uniform configuration shows stability improvement effects. Furthermore, by attaching piezoelectric materials onto the beam and applying an external electric voltage, stability of the smart structure can be further enhanced due to the local strain induced by piezoelectric layers.

The analytical development of efficient piezoelectric energy harvesters is another objective of this research. The work presented here challenges former energy harvesters and fabricates an advanced energy harvester configuration that functions optimally and effectively on ambient vibration sources. The developed model includes non-uniform geometry and accounts for the FGM property of the energy harvester. When the non-uniform design coupled with piezoelectric sensors is used as an energy harvester, it increases the system electromechanical outputs in a wide frequency domain. Lastly, piezoelectric stacks are deployed to design more robust and effective energy harvesting systems.

The main objectives of this research can be summarized and listed as:

- Development of a mathematical method capable of solving partial differential equations with nonlinear variable coefficients.
- Analytical vibration analysis of nonlinearly tapered and axially FGM beams.
- Stability analysis of nonlinearly tapered piezoelectric coupled beams.
- Design of a piezoelectric energy harvester with nonlinear geometry and FGM.
- Design of a wideband energy harvester by multiple non-uniform bimorphs.
- Design of a composite energy harvester with embedded piezoelectric stacks.
- Optimum design of a new energy harvester platform with piezoelectric stacks.
- Introducing a basic optimization model by using simulation-based optimization technique and machine learning algorithms.

Chapter 3

3 Mathematical Framework

The ADM is an operative mathematical technique for analytical solution of broad class of dynamic systems without linearization or weak nonlinearity assumptions, closure approximations, perturbation theory, or limiting assumptions on stochasticitiy [18]. The main advantage of the decomposition method is that unlike other methodologies and their restrictive assumptions, it does not require massive numerical computations and is physically more accurate and realistic. The solution delivered by ADM is also an approximation, but it does not change the nature of the system [110].

3.1 Adomian Decomposition Method

The solution obtained by ADM is an infinite series, an n-term approximation which serves as a practical and acceptable solution. An accurate solution is often obtained with very small values of n [110]. For numerical purposes, the solution can be enhanced by considering more terms and the response would be the exact solution of the problem if it exists [1], [111].

Additionally, there are some modifications using 'noise terms' to accelerate the rapid convergence of the series and therefore provides a major progress [112],

[113]. For a general explanation of the method, the Adomian [18] approach has been followed here.

Suppose the governing equation has the general form,

$$Ou + Ru + Nu = g, \tag{3-1}$$

where u is the response function, O is the highest order derivative operator, R includes derivatives of less order than O, Nu shows nonlinear terms, and g represents inhomogeneous external terms.

Knowing that O is an invertible nth order differential operator, O^{-1} is basically an n-fold integral. O^{-1} is an n-fold definite integral operator for initial value problems. On the other hand, O^{-1} will be an n-fold indefinite integral for boundary value problems which unknowns can be evaluated from boundary conditions.

Applying the inverse operator O^{-1} to both sides of the Eq. (3-1) leads to,

$$u = f + O^{-1}[g] - O^{-1}[Ru] - O^{-1}[Nu], \tag{3-2}$$

where f represents the terms arising from integration and given conditions.

Based on standard ADM, u is decomposed into $\sum_{n=0}^{\infty} u_n$ and the nonlinear term Nu is replaced by $\sum_{n=0}^{\infty} A_n$, where A_n are Adomian polynomials. Additionally, u_0 is identified as $f + O^{-1}[g]$. Thus, Eq. (3-2) is rewritten as,

$$\sum_{n=0}^{\infty} u_n = u_0 - O^{-1}[R \sum_{n=0}^{\infty} u_n] - O^{-1}[\sum_{n=0}^{\infty} A_n]. \tag{3-3}$$

Finally, the components can be determined recursively,

$$u_0 = f + O^{-1}[g],$$
$$u_{k+1} = u_0 - O^{-1}[Ru_k] - O^{-1}[A_k], \;\; k \geq 0. \tag{3-4}$$

3.2 Adomian Polynomials

The polynomial terms A_n are generated for each nonlinearity [18] and all of u_n components are calculable. If the series converge, the n-term partial sum $U_n = \sum_{i=0}^{n-1} u_i$ will be the approximate solution [110]. Since there is no linearization or weak nonlinearity assumptions, the presented solution will be much more accurate from the physical point of view.

Two formulations for the A_n polynomials are developed and presented [110]. By assuming $Nu \equiv h(u)$, the more convenient format is presented as,

$$A_0 = h(u_0),$$
$$A_1 = u_1 \frac{d}{du_0} h(u_0),$$
$$A_2 = u_2 \frac{d}{du_0} h(u_0) + \frac{u_1^2}{2!} \frac{d^2}{du_0^2} h(u_0), \tag{3-5}$$
$$A_3 = u_3 \frac{d}{du_0} h(u_0) + u_1 u_2 \frac{d^2}{du_0^2} h(u_0) + \frac{u_1^3}{3!} \frac{d^3}{du_0^3} h(u_0),$$
$$\ldots\ldots$$

The final solution provided by ADM is continuous, analytical, and requires no discretization or linearization. As a result, the solution is physically realistic and precise. The decomposition method is even more desirable when the problem includes variable coefficients, independent variables, and nonlinearities.

As a result, ADM is a powerful mathematical technique to provide the analytical solution of various vibrational systems. Although the solution obtained by ADM is an infinite series, an *n*-term approximation usually serves as a practical and acceptable solution [1].

Chapter 4

4 Vibration Analysis of Non-uniform Beams

In this chapter, vibration analysis of geometrically and materially non-uniform beams with general boundary conditions is comprehensively investigated. Numerical examples are provided to show the validity and accuracy of the model. Vibration mode shapes and natural frequencies of nonlinearly tapered cantilever beams with and without axially FGM properties are analytically derived and presented. Finally, nonlinear geometry and FGM effects are examined.

This chapter of the thesis is reproduced with some modifications from [A. Keshmiri, N. Wu, Q. Wang "Vibration analysis of a nonlinearly tapered cone beam using Adomian decomposition method", International Journal of Structural Stability and Dynamics, 18(7), 1850101, 2018] with permission from the "World Scientific Publishing Co Pte Ltd" and [A. Keshmiri, N. Wu, Q. Wang "Vibration analysis of non-uniform tapered beams with nonlinear FGM properties", Journal of Mechanical Science and Technology, 32(11), 5325-5337, 2018] with permission from the "Springer Nature".

4.1 Theoretical Model

The dynamic governing differential equation for the lateral vibration of a non-uniform Euler-Bernoulli beam applicable to slender beams by neglecting shear deformation and rotatory inertia effects, can be expressed by,

$$\rho(x)A(x)\frac{\partial^2 w(x,t)}{\partial t^2}+\frac{\partial^2}{\partial x^2}\left[E(x)I(x)\frac{\partial^2 w(x,t)}{\partial x^2}\right]=f(x,t), \tag{4-1}$$

where x is the position variable along length of the beam, t is the time variable, $\rho(x)$ is the mass density, $A(x)$ is the cross-sectional area, $w(x,t)$ is the deflection function, $E(x)$ is the Young's elasticity modulus, $I(x)$ is the second moment of area, and $f(x,t)$ is the external forcing function [22].

By using torsional K_T and linear K_L springs, general boundary conditions of the beam are defined as,

$$\begin{aligned}&\left[\pm E(x)I(x)\frac{\partial^2 w(x,t)}{\partial x^2}+K_T\frac{\partial w(x,t)}{\partial x}\right]_{x=0\ or\ L}=0,\\ &\left[\pm\frac{\partial}{\partial x}\left(E(x)I(x)\frac{\partial^2 w(x,t)}{\partial x^2}\right)+K_L w(x,t)\right]_{x=0\ or\ L}=0,\end{aligned} \tag{4-2}$$

where L is the length of the beam.

Eq. (4-1) can be expanded as,

$$\begin{aligned}&\rho(x)A(x)\frac{\partial^2 w(x,t)}{\partial t^2}+E(x)I(x)\frac{\partial^4 w(x,t)}{\partial x^4}+2\left[E(x)\frac{\partial I(x)}{\partial x}+I(x)\frac{\partial E(x)}{\partial x}\right]\frac{\partial^3 w(x,t)}{\partial x^3}+\\ &\left[E(x)\frac{\partial^2 I(x)}{\partial x^2}+I(x)\frac{\partial^2 E(x)}{\partial x^2}+2\frac{\partial E(x)}{\partial x}\frac{\partial I(x)}{\partial x}\right]\frac{\partial^2 w(x,t)}{\partial x^2}=f(x,t).\end{aligned} \tag{4-3}$$

Using the normal mode approach, the solution of Eq. (4-3) is assumed to be a linear combination of the normal modes of the beam expressed by,

$$w(x,t) = \sum_{i=1}^{\infty} X_i(x) T_i(t), \tag{4-4}$$

where $X_i(x)$ is the ith mass-normalized eigenfunction and $T_i(t)$ is the ith modal participation coefficient [46]. Clearly, the mass-normalized eigenfunctions satisfy the orthogonality conditions,

$$\begin{aligned} &\int_{x=0}^{L} \rho(x) A(x) X_i(x) X_j(x) \mathrm{d}x = \begin{cases} 1 \rightarrow i = j \\ 0 \rightarrow i \neq j \end{cases}, \\ &\int_{x=0}^{L} X_j(x) \frac{\mathrm{d}^2}{\mathrm{d}x^2} \left[E(x) I(x) \frac{\mathrm{d}^2 X_i(x)}{\mathrm{d}x^2} \right] \mathrm{d}x = \begin{cases} \omega_i^2 \rightarrow i = j \\ 0 \rightarrow i \neq j \end{cases}. \end{aligned} \tag{4-5}$$

Consequently, by substituting Eq. (4-4) into Eq. (4-3), two ordinary differential equations are obtained as,

$$\begin{aligned} &E(x) I(x) \frac{\mathrm{d}^4 X_i(x)}{\mathrm{d}x^4} + 2 \left[E(x) \frac{\mathrm{d}I(x)}{\mathrm{d}x} + I(x) \frac{\mathrm{d}E(x)}{\mathrm{d}x} \right] \frac{\mathrm{d}^3 X_i(x)}{\mathrm{d}x^3} + \left[E(x) \frac{\mathrm{d}^2 I(x)}{\mathrm{d}x^2} + I(x) \frac{\mathrm{d}^2 E(x)}{\mathrm{d}x^2} + \right. \\ &\left. 2 \frac{\mathrm{d}E(x)}{\mathrm{d}x} \frac{\mathrm{d}I(x)}{\mathrm{d}x} \right] \frac{\mathrm{d}^2 X_i(x)}{\mathrm{d}x^2} - \rho(x) A(x) {\omega_i}^2 X_i(x) = 0, \end{aligned} \tag{4-6}$$

$$\frac{\mathrm{d}^2 T_i(t)}{\mathrm{d}t^2} + {\omega_i}^2 T_i(t) = \frac{1}{\omega_i} \int_0^L X_i(x) f(x,t) \mathrm{d}x, \tag{4-7}$$

where ω_i is the ith natural frequency of the structure.

The final solution of the Eq. (4-7) using Duhamel integral can be expressed by,

$$T_i(t) = A_i \cos \omega_i t + B_i \sin \omega_i t + \frac{1}{\omega_i} \int_0^t \int_0^L X_i(x) f(x,t) \mathrm{d}x \sin \omega_i (t - \tau) \, \mathrm{d}\tau, \tag{4-8}$$

where A_i and B_i are constants that can be evaluated from initial conditions.

On the contrary, Eq. (4-6) is an ordinary differential equation with variable coefficients which requires an advanced mathematical tool to be solved. To derive the vibration mode shapes, the ADM is used. First, Eq. (4-6) is rewritten in an operator form,

$$O_x[X(x)] = -2\left(\frac{\frac{\mathrm{d}I(x)}{\mathrm{d}x}}{I(x)}+\frac{\frac{\mathrm{d}E(x)}{\mathrm{d}x}}{E(x)}\right)\frac{\mathrm{d}^3X(x)}{\mathrm{d}x^3}-\left(\frac{\frac{\mathrm{d}^2I(x)}{\mathrm{d}x^2}}{I(x)}+\frac{\frac{\mathrm{d}^2E(x)}{\mathrm{d}x^2}}{E(x)}+2\frac{\frac{\mathrm{d}I(x)}{\mathrm{d}x}}{I(x)}\frac{\frac{\mathrm{d}E(x)}{\mathrm{d}x}}{E(x)}\right)\frac{\mathrm{d}^2X(x)}{\mathrm{d}x^2}+\omega^2\frac{\rho(x)A(x)}{E(x)I(x)}X(x), \tag{4-9}$$

where $O_x=\frac{\mathrm{d}^4}{\mathrm{d}x^4}$ is a fourth order differential operator and the inverse operator L_x^{-1} will be a fourfold integration [1].

Applying O_x^{-1} on both sides of the Eq. (4-9) yields,

$$X(x) = C_1+C_2x+C_3\frac{x^2}{2!}+C_4\frac{x^3}{3!}-O_x^{-1}\left[2\left(\frac{\frac{\mathrm{d}I(x)}{\mathrm{d}x}}{I(x)}+\frac{\frac{\mathrm{d}E(x)}{\mathrm{d}x}}{E(x)}\right)\frac{\mathrm{d}^3X(x)}{\mathrm{d}x^3}+\left(\frac{\frac{\mathrm{d}^2I(x)}{\mathrm{d}x^2}}{I(x)}+\frac{\frac{\mathrm{d}^2E(x)}{\mathrm{d}x^2}}{E(x)}+2\frac{\frac{\mathrm{d}I(x)}{\mathrm{d}x}}{I(x)}\frac{\frac{\mathrm{d}E(x)}{\mathrm{d}x}}{E(x)}\right)\frac{\mathrm{d}^2X(x)}{\mathrm{d}x^2}-\omega^2\frac{\rho(x)A(x)}{E(x)I(x)}X(x)\right], \tag{4-10}$$

where C_1 to C_4 are constants that can be calculated from boundary conditions.

By equating the normal eigenfunction with its decomposition form, $X(x)=\sum_{j=0}^{\infty}X_j(x)$, vibration mode shape functions in the recurrence format is,

$$X_0(x) = C_1+C_2x+C_3\frac{x^2}{2!}+C_4\frac{x^3}{3!},$$

$$X_{k+1}(x) = -O_x^{-1}\left[2\left(\frac{\frac{\mathrm{d}I(x)}{\mathrm{d}x}}{I(x)}+\frac{\frac{\mathrm{d}E(x)}{\mathrm{d}x}}{E(x)}\right)\frac{\mathrm{d}^3X_k(x)}{\mathrm{d}x^3}+\left(\frac{\frac{\mathrm{d}^2I(x)}{\mathrm{d}x^2}}{I(x)}+\frac{\frac{\mathrm{d}^2E(x)}{\mathrm{d}x^2}}{E(x)}+2\frac{\frac{\mathrm{d}I(x)}{\mathrm{d}x}}{I(x)}\frac{\frac{\mathrm{d}E(x)}{\mathrm{d}x}}{E(x)}\right)\frac{\mathrm{d}^2X_k(x)}{\mathrm{d}x^2}-\omega^2\frac{\rho(x)A(x)}{E(x)I(x)}X_k(x)\right]\quad k\geq 0. \tag{4-11}$$

Therefore, all X_k components are evaluated for a specific mode shape. It should be mentioned that as many terms as required can be considered to obtain a more accurate mode shape function [22]. The n-term summation will be the approximate closed-form solution of the differential equation when the series converges [110].

Although the ADM methodology claims that it can handle any kind of variable coefficients in the differential equation, the calculation process can get very heavy due to computation complexity and sometimes impossible to solve because of some singularities in the functions. Therefore, for the transverse vibration of a beam with non-uniformity where $A(x)$, $I(x)$, $E(x)$, and $\rho(x)$ are nonlinear functions, the fourfold integration process in Eq. (4-10) can be intensive and impossible to deal with. In order to make the mathematical integration process possible and much more efficient, nonlinear coefficients of $\frac{\mathrm{d}^3X(x)}{\mathrm{d}x^3}$, $\frac{\mathrm{d}^2X(x)}{\mathrm{d}x^2}$, and $X(x)$ in the Eq. (4-10) should be replaced by simpler functions. In order to do that, Taylor series representations of those nonlinear functions as an infinite summation of terms calculated from the function derivatives values at a particular single point are employed [50]. For a real function $y(x)$ which is infinitely differentiable at a real point a, the Taylor series is the power series presented in Eq. (4-12), where $y^{(m)}(a)$ represents the mth derivative of $y(x)$ evaluated at point a,

$$y(x) \cong \sum_{m=0}^{\infty} \frac{y^{(m)}(a)}{m!}(x-a)^m. \tag{4-12}$$

Hence, $\frac{\frac{\mathrm{d}I(x)}{\mathrm{d}x}}{I(x)}$, $\frac{\frac{\mathrm{d}E(x)}{\mathrm{d}x}}{E(x)}$, $\frac{\frac{\mathrm{d}^2 I(x)}{\mathrm{d}x^2}}{I(x)}$, $\frac{\frac{\mathrm{d}^2 E(x)}{\mathrm{d}x^2}}{E(x)}$, and $\frac{\rho(x)A(x)}{E(x)I(x)}$ functions are replaced by the proper Maclaurin series (Taylor series at point zero) representation of them. This simple modification greatly reduces the calculation intensity.

By substituting the mode shape functions into the four boundary conditions of the beam, a system of four equations with unknown constants is given,

$$H_{j1}^{n}(\omega_i)C_1 + H_{j2}^{n}(\omega_i)C_2 + H_{j3}^{n}(\omega_i)C_3 + H_{j4}^{n}(\omega_i)C_4 = 0 \quad (j = 1,2,3,4), \tag{4-13}$$

where $H_{j1}^{n}(\omega_i)$, $H_{j2}^{n}(\omega_i)$, $H_{j3}^{n}(\omega_i)$, and $H_{j4}^{n}(\omega_i)$ are coefficients of unknown constants C_1 to C_4 corresponding to the n-term solution series as a function of ith natural frequency ω_i [1], [22].

For the nontrivial solution, determinant of the coefficients must be zero giving the eigenvalue problem,

$$\begin{vmatrix} H_{11}^{n}(\omega_i) & \cdots & H_{14}^{n}(\omega_i) \\ \vdots & \ddots & \vdots \\ H_{41}^{n}(\omega_i) & \cdots & H_{44}^{n}(\omega_i) \end{vmatrix} = 0. \tag{4-14}$$

Consequently, ω_i^n which is the ith eigenvalue and natural frequency of the beam corresponding to the n-term solution series is evaluated. Substituting ω_i^n into Eq. (4-14) and choosing an arbitrary constant, other three unknowns will be evaluated. Then Eq. (4-11) yields the ith mode shape function [22].

Finally, normal mode eigenfunctions are given by Eq. (4-11) and modal participation coefficients obtained by Eq. (4-8) can be substituted into Eq. (4-4) to represent the steady-state dynamic response of the non-uniform structure,

$$w(x,t) = \sum_{i=1}^{\infty} \sum_{k=0}^{n} X_{k_i}(x) \left[\frac{1}{\omega_i} \int_0^t \int_0^L X_i(x) f(x,t) \mathrm{d}x \sin \omega_i (t-\tau) \, \mathrm{d}\tau \right]. \quad (4\text{-}15)$$

4.2 Free Vibration Simulation and Discussion

To provide a clear overview of the modeling process and validate the proposed analytical model, several sample cases are chosen. Firstly, natural frequencies of homogeneous beams with uniform, linearly tapered, and exponentially tapered geometries are compared with published results in the literature. Next, beams with uniform and linearly tapered geometries and FGM properties are analyzed and their natural frequencies are evaluated and compared with the published data. Since the data comparison has only been done for three first natural frequencies, no statistical data analysis was performed. Finally, first three natural frequencies and vibration mode shapes of exponentially and trigonometrically tapered beams with and without nonlinear FGM considering different geometry and material taper ratios [22] are studied and presented. Natural frequencies are reported in non-dimensional forms, where the non-dimensional frequency of the beam is defined as, $\lambda^4 = \omega^2 \frac{\rho_0 A_0 L^4}{E_0 I_0}$ in which ρ_0, A_0, E_0, and I_0 are defined at the fixed end of the beam.

First three non-dimensional natural frequencies of a uniform cantilever beam are compared with results from reference [6] in Table 4-1. By using only 7 terms of the mode shape function series, accurate values are calculated which proves the high convergence rate of the methodology [1].

Table 4-1 Non-dimensional first three natural frequencies of a uniform cantilever beam [1].

	$\lambda_1^{0.25}$	$\lambda_2^{0.25}$	$\lambda_3^{0.25}$
[6]	1.875	4.694	7.855
present method	1.875	4.694	7.855

For the linearly tapered geometry, width $b(x) = b_0\left(1 - n_b\frac{x}{l}\right)$ and thickness $h(x) = h_0\left(1 - n_h\frac{x}{l}\right)$ of the beam can vary linearly where b_0 and h_0 are width and thickness at the fixed end and n_b and n_h are taper ratios in those directions, respectively. By assuming the same taper ratio m in both directions, the variable cross-sectional area and second moment of area functions are $A(x) = A_0\left(1 - m\frac{x}{l}\right)^2$ and $I(x) = I_0\left(1 - m\frac{x}{l}\right)^4$, where $A_0 = b_0h_0$ and $I_0 = \frac{1}{12}b_0h_0^3$ are defined as the cross-sectional area and the second moment of area of the beam at its fixed boundary. Besides, 30 terms of Taylor series are used to represent the functions in the fourfold integration process. First three non-dimensional natural frequencies of a linearly tapered cantilever beam with different taper ratios are given in Table 4-2. These values are determined using 17 terms of the mode shape function series. The good agreement of the reported results compared to the published results from other methodologies proves the effectiveness of the proposed model [1].

Finally, for an exponentially tapered beam along width, thickness of the beam is assumed to be constant $h(x) = h_0$ and width varies exponentially $b(x) = b_0\mathrm{e}^{-m\frac{x}{l}}$ where m is the taper ratio in width direction. Hence, cross-sectional area and second moment of area functions are $A(x) = A_0\mathrm{e}^{-m\frac{x}{l}}$ and $I(x) = I_0\mathrm{e}^{-m\frac{x}{l}}$. Following the same mathematical process, vibration mode shape functions and natural frequencies of a cantilever beam exponentially tapered along width can be calculated. Table 4-3 shows the first three non-dimensional natural frequencies of the beam by using 12 terms of the mode shape function series. By comparing to other published results, great agreement and precision can be seen [1].

Table 4-2 Non-dimensional first three natural frequencies for a linearly tapered cantilever beam [1].

	$\lambda_1^{0.5}$				$\lambda_2^{0.5}$				$\lambda_3^{0.5}$			
m	[12]	[19]	[114]	present method	[12]	[19]	[114]	present method	[12]	[19]	[114]	present method
0.1	---	3.673	---	3.674	---	21.550	---	21.550	---	59.189	---	59.189
0.2	---	3.855	3.831	3.855	---	21.057	21.082	21.057	---	56.630	56.641	56.630
0.3	4.067	4.067	---	4.067	20.555	20.555	---	20.555	---	54.015	---	54.015
0.4	4.319	4.319	4.322	4.319	20.05	20.05	20.113	20.050	51.334	51.335	51.351	51.334
0.5	4.625	4.625	4.631	4.625	19.548	19.548	19.548	19.550	48.579	48.579	48.588	48.563

Table 4-3 Non-dimensional first three natural frequencies for an exponentially tapered cantilever beam along width [1].

	$\lambda_1^{0.5}$	$\lambda_2^{0.5}$	$\lambda_3^{0.5}$
[6]	4.735	24.202	63.850
[115]	4.735	24.200	63.861
[116]	4.723	24.202	63.864
present method	4.735	24.202	63.861

For beams with axially FGM properties, special polynomials for material non-homogeneity presented by [29] are used. Non-dimensional first two natural frequencies for a uniform cantilever beam with polynomial material variation function are presented in Table 4-4. By using only 13 terms of the mode shape function series, accurate values are evaluated [22].

Table 4-4 Non-dimensional first two natural frequencies for a uniform cantilever beam with polynomial material property variation function [22].

$\rho(x) = \sum_{j=0}^{J} a_j (\frac{x}{l})^j$	$E(x) = \sum_{h=0}^{H} b_{Jh} (\frac{x}{l})^h$	λ_1		λ_1	
		[30]	present method	[30]	present method
1	26	321.42	321.42	12623.84	12623.49
	$26 + 16\left(\frac{x}{l}\right)$	357.20	357.20	15615.45	15615.42
	$26 + 16\left(\frac{x}{l}\right) + 6\left(\frac{x}{l}\right)^2$	360.78	360.78	16174.13	16174.25
	$26 + 16\left(\frac{x}{l}\right) + 6\left(\frac{x}{l}\right)^2 - 4\left(\frac{x}{l}\right)^3$	359.90	359.89	15962.74	15962.51
	$26 + 16\left(\frac{x}{l}\right) + 6\left(\frac{x}{l}\right)^2 - 4\left(\frac{x}{l}\right)^3 + \left(\frac{x}{l}\right)^4$	360.00	360.07	15994.99	15997.55
$1 + \frac{x}{l}$	64.8	443.35	443.35	19861.39	19860.84
	$64.8 + 42.8\left(\frac{x}{l}\right)$	497.23	497.22	25081.87	25080.96
	$64.8 + 42.8\left(\frac{x}{l}\right) + 20.8\left(\frac{x}{l}\right)^2$	504.24	504.24	26363.87	26363.46
	$64.8 + 42.8\left(\frac{x}{l}\right) + 20.8\left(\frac{x}{l}\right)^2 - 1.2\left(\frac{x}{l}\right)^3$	504.09	504.09	26321.93	26321.46
	$64.8 + 42.8\left(\frac{x}{l}\right) + 20.8\left(\frac{x}{l}\right)^2 - 1.2\left(\frac{x}{l}\right)^3 - 2.2\left(\frac{x}{l}\right)^4$	503.97	503.97	26274.88	26274.65
$1.5954 + 0.04\left(\frac{x}{l}\right) + \left(\frac{x}{l}\right)^2$	109.94475	590.22	590.22	26503.05	26502.90
	$109.94475 + 72.87061\left(\frac{x}{l}\right)$	662.40	662.38	33454.66	33454.13
	$109.94475 + 72.87061\left(\frac{x}{l}\right) + 35.79648\left(\frac{x}{l}\right)^2$	671.91	671.91	35176.27	35176.54
	$109.94475 + 72.87061\left(\frac{x}{l}\right) + 35.79648\left(\frac{x}{l}\right)^2 - 1.27765\left(\frac{x}{l}\right)^3$	671.79	671.78	35141.46	35141.69
	$109.94475 + 72.87061\left(\frac{x}{l}\right) + 35.79648\left(\frac{x}{l}\right)^2 - 1.27765\left(\frac{x}{l}\right)^3 + 0.36325\left(\frac{x}{l}\right)^4$	672.06	671.80	35246.03	35147.71

As the second FGM case study, a uniform beam with $E(x) = 1 + \gamma\cos(\pi\frac{x}{l})$ and $\rho(x) = 1 + \alpha\cos(\pi\frac{x}{l})$ material property variation functions is analyzed where γ and α are rigidity and density taper parameters, respectively. Table 4-5 shows the non-dimensional first three natural frequencies. Only 6 terms of the mode shape function series are considered for this case which proves the high convergence rate of the method. Additionally, natural frequencies are compared with results from reference [30] showing an excellent agreement [22].

Table 4-5 Non-dimensional first three natural frequencies for a uniform cantilever beam with trigonometric material property variation function [22].

$\alpha = \gamma$	$\lambda_1^{0.5}$		$\lambda_2^{0.5}$		$\lambda_3^{0.5}$	
	[30]	present method	[30]	present method	[30]	present method
0	3.516	3.516	22.034	22.034	61.715	61.806
0.1	3.785	3.785	22.444	22.442	61.976	63.267
0.15	3.928	3.928	22.653	22.641	62.119	65.151
0.2	4.076	4.078	22.867	22.896	62.274	66.649

Now, linearly tapered cantilever beams with axially variable density and elasticity modulus are considered. First example is a beam with linearly tapered geometry and polynomial material property variation function. This means $A(x) = \left(1 - m\frac{x}{l}\right)^2$ and $I(x) = \left(1 - m\frac{x}{l}\right)^4$ which m is the geometrical taper ratio. Also, $E(x) = 1 + \frac{x}{l}$ and $\rho(x) = 1 + \frac{x}{l} + (\frac{x}{l})^2$ are elasticity and density variation functions, respectively. Non-dimensional first three natural frequencies for such a beam are presented in Table 4-6. Results are evaluated using 11 terms of the mode shape function series. The difference and small errors comparing with results from reference [33] for taper ratios higher than 0.6 are because of the elasticity linear function. Generally, the residual error in approximating linear functions with Taylor polynomial series might be high without considering a great number of terms. Replacing the linear functions with an appropriate Taylor polynomial series needs considering so many terms that could result in an intensive calculation process. Moreover, for higher natural frequencies of the structure, more terms of mode shape function series are required. Considering all of these factors requires more computational power and memory capacitance. Here, 30 terms of Taylor polynomial series are used to replace the linear function. For second and third natural frequencies of the beam with 0.8 taper ratio, no values by using 11 terms of the mode shape function series are evaluated. Clearly, more terms should be considered using the proposed method [22].

Table 4-6 Non-dimensional first three natural frequencies of a linearly tapered cantilever beam with polynomial material property variation function [22].

m	$\lambda_1^{0.5}$		$\lambda_2^{0.5}$		$\lambda_3^{0.5}$	
	[33]	present method	[33]	present method	[33]	present method
0	2.426	2.273	18.604	17.814	55.180	53.370
0.2	2.686	2.536	17.750	17.016	50.393	48.747
0.4	3.049	2.908	16.857	16.203	45.400	43.948
0.6	3.598	3.443	15.962	17.056	40.130	32.138
0.8	4.569	4.636	15.296	---	34.552	---

The second beam possesses constant width and linearly variable thickness with $A(x) = \left(1 - m\frac{x}{l}\right)$ and $I(x) = \left(1 - m\frac{x}{l}\right)^3$, where m is the taper ratio. Here in this case, elasticity modulus $E(x) = e^{\frac{x}{l}}$ and density $\rho(x) = e^{\frac{x}{l}}$ vary exponentially. Table 4-7 provides the non-dimensional first two natural frequencies for a linearly tapered cantilever beam along its thickness with exponential material property variation. Results are compared with ones from references [117] and [118]. Non-dimensional natural frequencies of taper ratio 0.1, 0.3, 0.5, and 0.8 are evaluated using 14, 14, 15, and 20 terms of the mode shape function series, respectively [22].

Table 4-7 Non-dimensional first two natural frequencies for a linearly tapered along thickness cantilever beam with exponential material property variation function [22].

m	$\lambda_1^{0.5}$			$\lambda_2^{0.5}$		
	[118]	[117]	present method	[118]	[117]	present method
0.1	2.606	2.606	2.606	19.413	19.410	19.412
0.3	2.708	2.709	2.708	18.100	18.101	18.100
0.5	2.856	2.857	2.856	16.688	16.692	16.688
0.8	3.292	3.293	3.294	14.362	14.371	14.380

For a homogeneous beam with nonlinear geometry, three cases are selected. The first one is an experimental validation of the model by studying an exponentially tapered beam with homogeneous material properties. First two natural frequencies of an exponentially tapered cantilever beam with a circular cross-section are experimentally measured and test results are compared with values obtained by the theoretical model. The variable profile for the radius of the beam cross-section is defined as $R(x) = R_0\left(\mathrm{e}^{m\frac{x}{l}}\right)$ where m is geometry taper ratio and R_0 is the radius at the fixed end of the beam [22], [50]. The geometric dimensions and material properties of the beam are listed in Table 4-8.

Table 4-8 Geometry and material properties of the exponentially tapered cantilever beam [22].

L (m)	R_0 (m)	m	E (Pa)	ρ (kg/m^3)
0.1625	0.00275	0.8	$68.9*10^{10}$	2700

Here, 10 terms of Taylor series are used to represent the nonlinear taper function. Fig. 4-1(a) shows the testing setup used for the experiment and Fig. 4-1(b) presents the LMS test frequency spectral with two peaks for the first and second natural frequencies of the non-uniform structure. The first two natural frequencies evaluated from the experimental tests are 96.13Hz and 1055.41Hz, respectively. By using the theoretical model, these two values are calculated as 99.09Hz and 1075.76Hz. The comparison of results proves the accuracy and validity of the method. As long as accurate mode shape functions and natural frequencies of different tapered structures can be obtained, the precise dynamic analysis can be done. It is noted that Euler-Bernoulli beam model ignores shear strain/stress in the beam cross-sections that leads to higher stiffness of the beam and natural frequencies compared with the practical problem. Therefore, the eigenvalues or natural frequencies of the free vibration analysis based on the presented model are a bit higher than the experiment results [22].

(a)

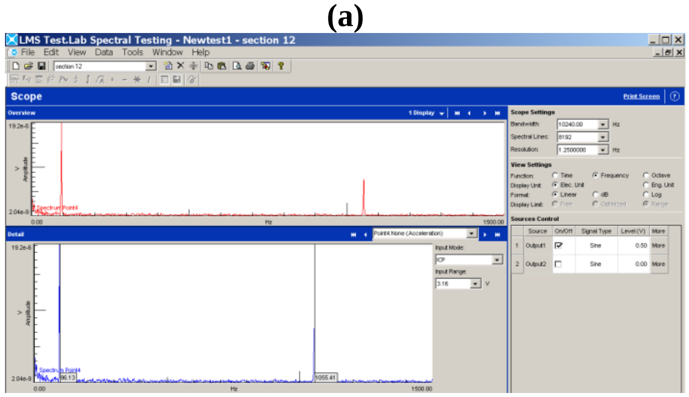

(b)

Fig. 4-1 Free vibration test of an exponentially tapered and homogeneous cantilever beam. (a) Experimental setup [22]. (b) Spectral frequency response in LMS.

Secondly, a convergence study on the second non-dimensional natural frequency of an exponentially tapered cantilever beam with homogeneous material properties for various geometrical taper ratios is presented in Fig. 4-2. As can be seen, the presented model has very high measurement resolution and rapid convergence rate with small nonlinearity (*m*<=0.3) even by a few numbers of ADM series terms (n<=7). On the other hand, for higher taper ratios (*m*=>0.4), the convergence rate is slower and high measurement resolution can be obtained by considering more series terms (n>10). It is noted that the occurrence of divergence in the model can be the result of several parameters such as: residual error incurred in approximating geometry and FGM functions by Taylor polynomials, insufficient number of series in the mode shape functions, and possible issues coming from the mathematical solving process of eigenvalue problem [22].

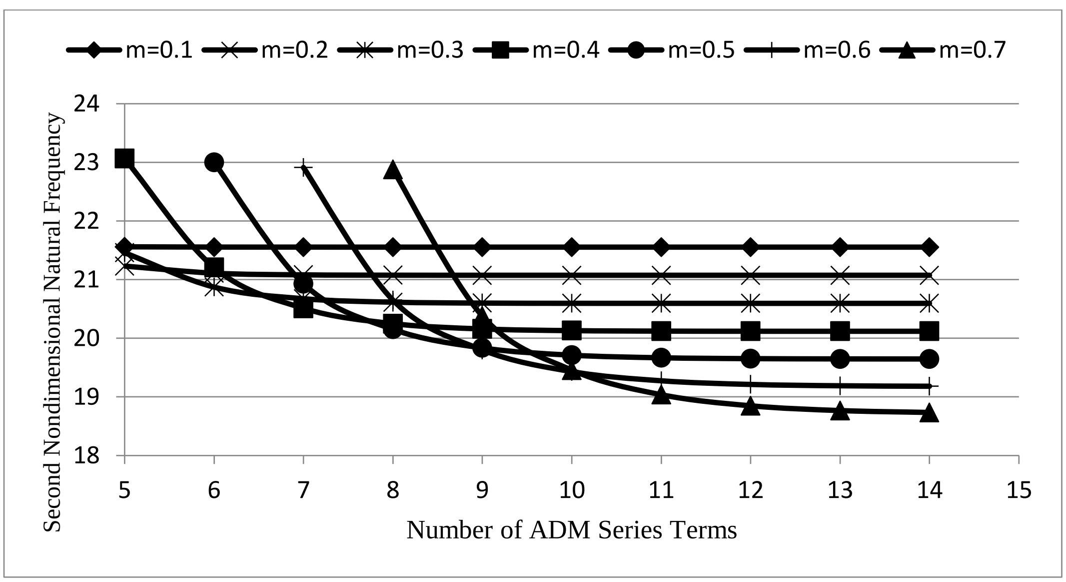

Fig. 4-2 The convergence study on the second non-dimensional natural frequency of an exponentially tapered cantilever beam with homogeneous material properties with various geometrical taper ratios [22].

The second case depicted in Fig. 4-3(a) is an exponentially tapered cantilever beam which its width and thickness variation functions are expressed by $b(x) = b_0\left(\mathrm{e}^{-n_b\frac{x}{l}}\right)$ and $h(x) = h_0\left(\mathrm{e}^{-n_h\frac{x}{l}}\right)$. By assuming the same taper ratio m in both directions, cross-sectional area and second moment of area functions are defined as $A(x) = A_0\left(\mathrm{e}^{-m\frac{x}{l}}\right)^2$ and $I(x) = I_0\left(\mathrm{e}^{-m\frac{x}{l}}\right)^4$ [1].

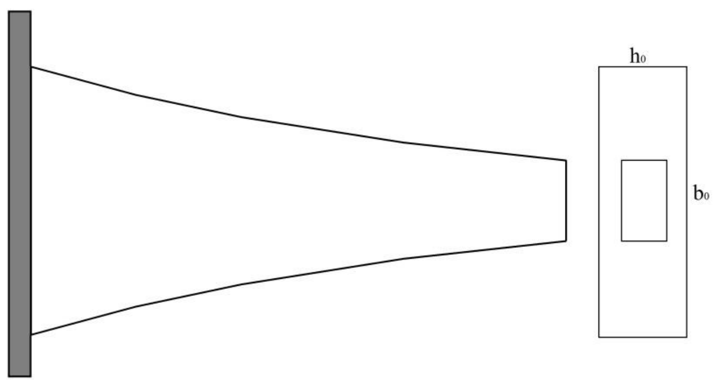

(a)

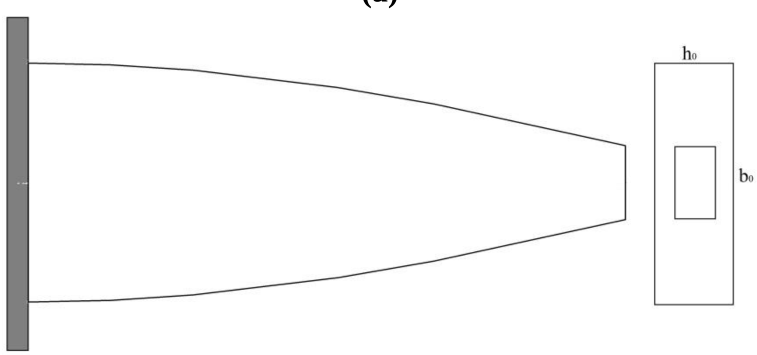

(b)

Fig. 4-3 Non-uniform cantilever tapered cone beams with cross-sectional view [1]. (a) Exponentially decaying. (b) Trigonometrically decaying.

By following the same computation procedure, the vibration mode shape functions and non-dimensional natural frequencies of an exponentially tapered beam can be obtained. Besides, 10 terms of Taylor series are used to represent the nonlinear functions in the fourfold integration. Table 4-9 represents the convergence study of the non-dimensional first three natural frequencies for various taper ratios. As can be seen, the model gives the natural frequencies for lower taper ratios (*m*<=0.5) with very high measurement resolution and rapid convergence rate even with small values of *n* (*n*<=10) for the mode shape function series. For higher taper ratios of the nonlinearly tapered beam (*m*>0.5), analytical approximation for the vibration characteristics with good accuracy can be obtained considering more mode shape function series terms (n>12). Similar to linearly tapered beams, increasing the taper ratio results in higher first natural frequency and lower second and third natural frequencies for the beam with exponentially decaying geometry. Moreover, four vibration mode shapes of the exponentially decaying configuration with taper ratio of *m*=0.3 are given in Fig. 4-4 [1].

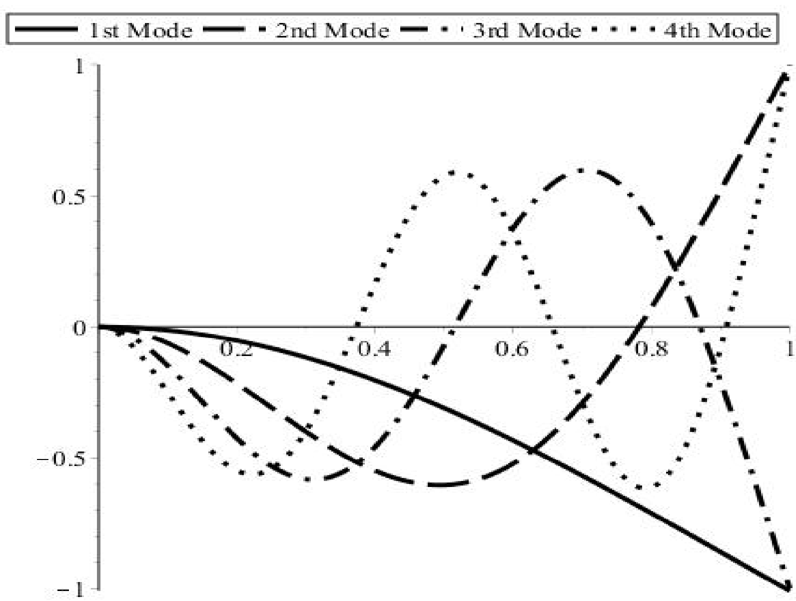

Fig. 4-4 First four vibration mode shapes of an exponentially decaying tapered cantilever beam with taper ratio of *m*=0.3 [1].

For the second homogeneous beam with nonlinear geometry, a trigonometrically tapered cone beam is chosen in which the cross-section varies according to a cosine function, Fig. 4-3(b). By assuming the same taper ratio *m* in width and thickness directions, cross-sectional area and second moment of area variation functions are defined as $A(x) = A_0\left(\cos\left(\frac{m\pi x}{2l}\right)\right)^2$ and $I(x) = I_0\left(\cos\left(\frac{m\pi x}{2l}\right)\right)^4$. Only 20 terms of Taylor series are used to represent the nonlinear functions in the fourfold integration. Table 4-10 shows the convergence study of the non-dimensional first three natural frequencies of a trigonometrically tapered cantilever beam with various taper ratios. In the same way, accurate natural frequencies for lower taper ratios can be found even with very small values of *n* for the mode shape function series. Increasing the taper ratio results in higher first natural frequency and lower second and third natural frequencies. This is the same trend for the beams with similar structural geometries, i.e., linearly and exponentially decaying profile. Finally, Fig. 4-5 depicts the first four vibration mode shapes of the trigonometrically tapered beam with taper ratio of m=0.3 [1].

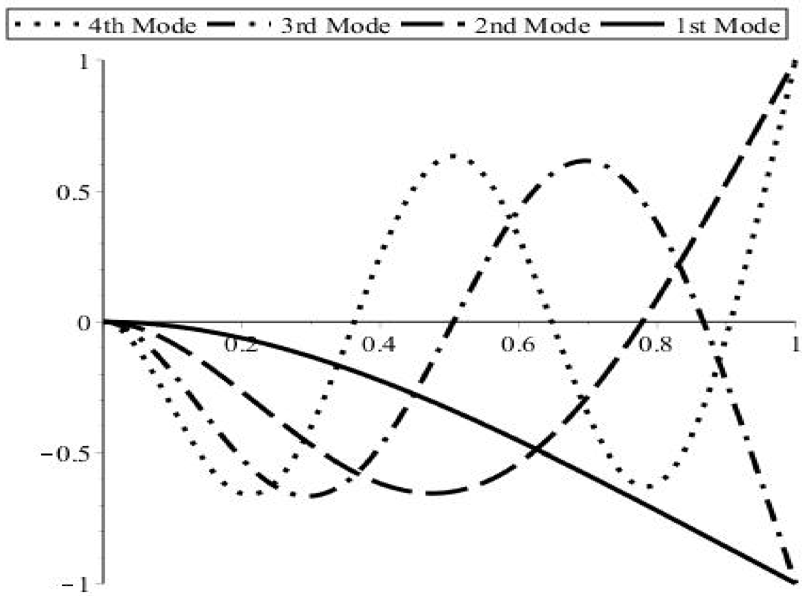

Fig. 4-5 First four vibration mode shapes of a cosine function tapered cantilever beam with taper ratio of *m*=0.3 [1].

For a beam with nonlinear geometry and material properties, three cases are studied. Firstly, an exponentially tapered cantilever with exponential density and elasticity modulus variation functions is considered. This means $A(x) = \left(e^{-m\frac{x}{l}}\right)^2$, $I(x) = \left(e^{-m\frac{x}{l}}\right)^4$, $E(x) = e^{-\beta\frac{x}{l}}$, and $\rho(x) = e^{-\alpha\frac{x}{l}}$, where m, β, and α are geometry, rigidity, and density taper ratios, respectively. Table 4-11 shows the convergence study for the non-dimensional first three natural frequencies of an exponentially tapered cone cantilever beam with exponential FGM properties. As can be seen, the presented model gives the natural frequencies for different geometry and material taper ratios with high measurement resolution and rapid convergence rate. For lower geometrical and material taper ratios, the convergence rate is much higher. For instance, when m=α=β=0.1, only 6 terms of the mode shape function series provide very accurate values of first three natural frequencies. The analytical approximation of the vibration characteristics for higher taper ratios can be achieved with good accuracy by considering more terms of the mode shape function series. Lastly, the first four vibration mode shapes of the beam are given in Fig. 4-6 with the geometry, density, and elasticity taper ratios of m=0.1, α=0.3, and β=0.5 [22].

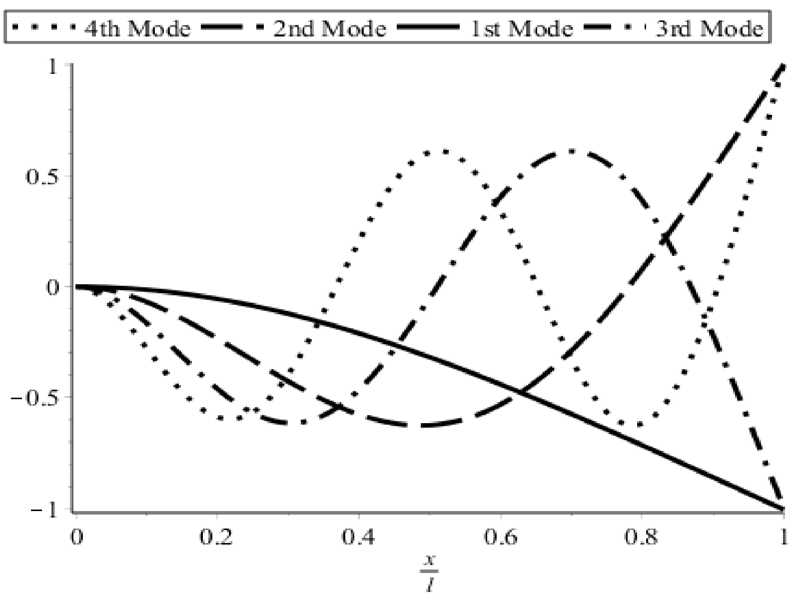

Fig. 4-6 First four vibration mode shapes for an exponentially tapered cantilever beam with exponential material property variation function (m=0.1, α=0.3, β=0.5) [22].

Secondly, exponentially tapered geometry and cosine function variation for elasticity modulus and density are considered. This means $A(x) = \left(e^{-m\frac{x}{l}}\right)^2$, $I(x) = \left(e^{-m\frac{x}{l}}\right)^4$, $E(x) = \left(\cos\frac{\beta\pi x}{2l}\right)$, and $\rho(x) = \left(\cos\frac{\alpha\pi x}{2l}\right)$. The convergence study for non-dimensional first three natural frequencies of such a beam can be seen in Table 4-12. Similarly, the convergence rate is very high for the beam structure with lower values of geometrical and material taper ratios. And the solution for a structure with higher taper ratios can be improved by considering more terms of the mode shape function series. Additionally, Fig. 4-7 depicts the first four vibration mode shapes of an exponentially tapered cantilever beam with cosine function FGM properties with the geometry, density, and elasticity taper ratios of m=0.1, α=0.3, and β=0.5, respectively [22].

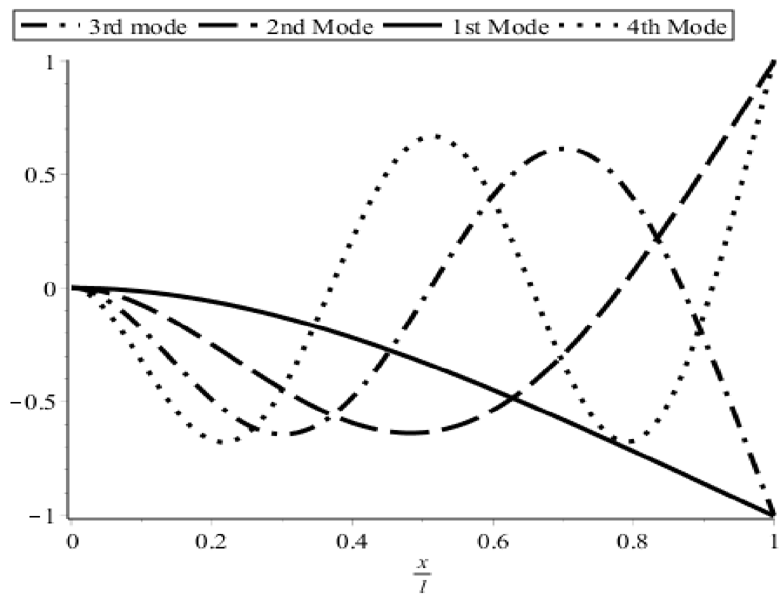

Fig. 4-7 First four vibration mode shapes for an exponentially tapered cantilever beam with cosine material property variation function (m=0.1, α=0.3, β=0.5) [22].

Finally, a trigonometrically tapered cantilever beam with exponential elasticity modulus and density variation functions is considered. Thus, $A(x) = \left(\cos\frac{m\pi x}{2l}\right)^2$, $I(x) = \left(\cos\frac{m\pi x}{2l}\right)^4$, $E(x) = e^{-\beta\frac{x}{l}}$, and $\rho(x) = e^{-\alpha\frac{x}{l}}$. Table 4-13 displays the convergence study for non-dimensional first three natural frequencies of a cosine tapered cantilever beam with exponential FGM properties. The proposed model based on ADM provides the natural frequencies for different geometry and material taper ratios with very high measurement resolution and rapid convergence rate even with small values of *n* for the mode shape function series. For lower taper ratios, the convergence rate is higher. Likewise, more accurate natural frequencies and mode shapes for higher taper ratios can be obtained with more terms of the mode shape series. The first four vibration mode shapes of the beam are depicted in Fig. 4-8 with the geometry, density, and elasticity taper ratios of m=0.1, α=0.3, and β=0.5, respectively [22].

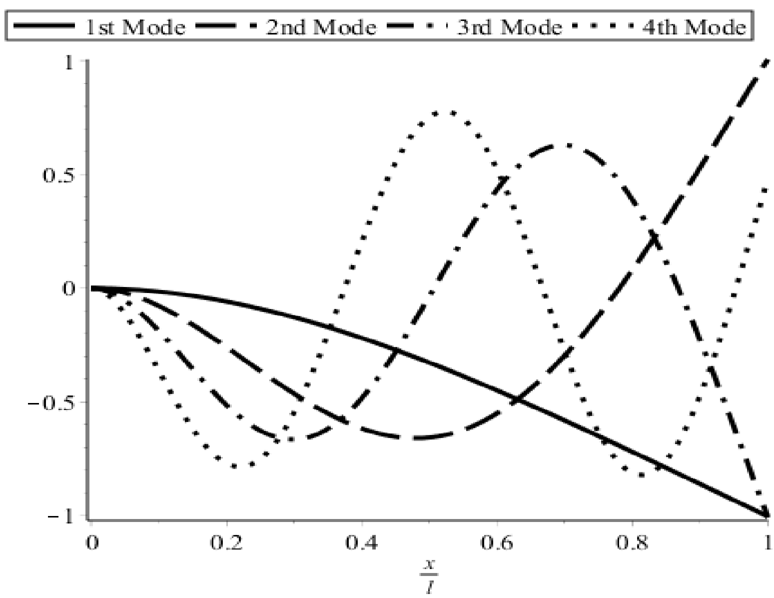

Fig. 4-8 First four vibration mode shapes for a trigonometrically tapered cantilever beam with exponential material property variation function (m=0.1, α=0.3, β=0.5) [22].

Last of all, Figs. 4-9 to 4-11 show first three non-dimensional natural frequencies variation with respect to geometry, density, and elasticity taper ratios for three kinds of geometrically and materially nonlinear beams discussed here. As it is shown in the figures, increasing the geometry taper ratio results in higher first natural frequency and smaller second and third natural frequencies regardless of the material taper ratio effect. Furthermore, an overall decline in the natural frequencies occurs by increasing the elasticity taper ratio. This can be the result of higher rigidity of the structure. In contrast, a considerable growth in natural frequencies of the beam can be seen as density taper ratio increases. For instance, a beam with m=0.5, α=0.5, and β=0.1 and a beam with m=0.1, α=0.1, and β=0.5 have the highest and lowest values for the first natural frequency, respectively. On the other hand, a beam with m=0.1, α=0.5, and β=0.1 and a beam with m=0.5, α=0.1, and β=0.5 have the highest and lowest values for the second and third natural frequencies, respectively. Regarding the structural requirements and applications, one can find and choose the most efficient mechanical and vibrational design of the non-uniform beam or column [22].

Table 4-9 Convergence study of non-dimensional first three natural frequencies of a homogeneous and exponentially decaying tapered cantilever beam [1].

m	$X = X_0 + \cdots + X_i$	$\lambda_1^{0.5}$	$\lambda_2^{0.5}$	$\lambda_3^{0.5}$
0.1	i = 14	3.663135777	21.55454395	59.25992606
	i = 13	3.663135777	21.55454397	59.25992500
	i = 12	3.663135777	21.55454397	59.25992498
	i = 11	3.663135773	21.55454394	59.25992801
	i = 10	3.663135773	21.55454399	59.25992763
0.2	i = 14	3.808838427	21.07440885	56.91704897
	i = 13	3.808838423	21.07440881	56.91704847
	i = 12	3.808838384	21.07440900	56.91704378
	i = 11	3.808838052	21.07441170	56.91697096
	i = 10	3.808835605	21.07443281	56.91636879
0.3	i = 14	3.952201378	20.59548305	54.66483242
	i = 13	3.952200738	20.59548748	54.66476310
	i = 12	3.952197048	20.59551398	54.66430321
	i = 11	3.952177414	20.59566190	54.66150274
	i = 10	3.952081402	20.59642435	54.64592563
0.4	i = 14	4.092245712	20.11907362	52.49942475
	i = 13	4.092229978	20.11919037	52.49796724
	i = 12	4.092162283	20.11970947	52.49084690
	i = 11	4.091892957	20.12185258	52.45855502
	i = 10	4.090909057	20.13002623	52.32541669
0.5	i = 14	4.227912834	19.64669954	50.41420582
	i = 13	4.227766743	19.64797336	50.40045099
	i = 12	4.227264394	19.65245986	50.34712722
	i = 11	4.225668012	19.66713544	50.15776994
	i = 10	4.221017779	19.71148844	49.56486763
0.6	i = 14	4.357984808	19.18173000	48.38666140
	i = 13	4.357298414	19.18959741	48.30872694
	i = 12	4.355322792	19.21251277	48.06343243
	i = 11	4.350073952	19.27460442	47.37844453
	i = 10	4.337324416	19.43104879	45.77896297
0.7	i = 14	4.481229077	18.73434703	46.34043141
	i = 13	4.479486291	18.76693042	46.03944329
	i = 12	4.475075216	18.84804450	45.27531802
	i = 11	4.464788152	19.03737683	43.63208966
	i = 10	4.442925291	19.45681787	40.74131636
0.8	i = 14	4.598024476	18.33072215	44.08286266
	i = 13	4.596592349	18.43137169	43.24804108
	i = 12	4.592559524	18.65271907	41.57348136
	i = 11	4.582599496	19.11975879	38.76061297
	i = 10	4.560964125	20.11475708	34.65149439
0.9	i = 14	4.715568903	18.02340999	41.29220819
	i = 13	4.722487269	18.27473642	39.59314114
	i = 12	4.731027505	18.78625837	36.84932579
	i = 11	4.737401846	19.85783855	32.88763279
	i = 10	4.733591552	23.49765062	25.98954423

Table 4-10 Convergence study of non-dimensional first three natural frequencies of a homogeneous and cosine function tapered cantilever beam [1].

m	$X = X_0 + \cdots + X_i$	$\lambda_1^{0.5}$	$\lambda_2^{0.5}$	$\lambda_3^{0.5}$
0.1	i = 14	3.540075583	22.02441139	61.52196908
	i = 13	3.540075583	22.02441139	61.52196908
	i = 12	3.540075583	22.02441147	61.52196309
	i = 11	3.540075583	22.02441139	61.52196914
	i = 10	3.540075583	22.02441148	61.52196649
0.2	i = 14	3.613910966	21.99458243	60.99588388
	i = 13	3.613910966	21.99458243	60.99588388
	i = 12	3.613910966	21.99458235	60.99588883
	i = 11	3.613910966	21.99458244	60.99588224
	i = 10	3.613910966	21.99458245	60.99588327
0.3	i = 14	3.742770822	21.94662737	60.11806782
	i = 13	3.742770822	21.94662737	60.11806762
	i = 12	3.742770826	21.94662736	60.11806657
	i = 11	3.742770830	21.94662734	60.11806750
	i = 10	3.742770869	21.94662684	60.11816314
0.4	i = 14	3.936456355	21.88482633	58.88737649
	i = 13	3.936456406	21.88482601	58.88739034
	i = 12	3.936456724	21.88482388	58.88750131
	i = 11	3.936458986	21.88480741	58.88840035
	i = 10	3.936473370	21.88469116	58.89513106
0.5	i = 14	4.211298961	21.81969349	57.30423493
	i = 13	4.211315760	21.81963668	57.30596097
	i = 12	4.211392064	21.81935547	57.31502004
	i = 11	4.211709113	21.81807082	57.35915679
	i = 10	4.212904113	21.81269055	57.55957882
0.6	i = 14	4.594772066	21.77550953	55.41106834
	i = 13	4.596688416	21.77151430	55.51066246
	i = 12	4.602177036	21.75903776	55.85270659
	i = 11	4.616444652	21.72326243	57.03341384
	i = 10	4.649610477	21.63053360	63.80459073
0.7	i = 14	5.197141968	21.74427641	55.35250717
	i = 13	5.272768742	21.64486638	63.40492017
	i = 12	5.405092458	21.45585009	---
	i = 11	5.606592266	21.13994153	---
	i = 10	5.865454839	20.68642251	---
0.8	i = 14	7.555630609	21.16532353	---
	i = 13	7.928422186	20.91500853	---
	i = 12	8.154676971	20.72240051	---
	i = 11	8.191927289	20.59871065	---
	i = 10	8.049618282	20.52660505	---
0.9	i = 14	9.563494814	24.33144205	---
	i = 13	9.155603472	24.34129036	---
	i = 12	8.787684625	24.27214951	---
	i = 11	8.475096130	24.11906315	---
	i = 10	8.222903984	23.87618238	---

Table 4-11 Non-dimensional first three natural frequencies of an exponentially tapered cantilever beam with exponential material property variation function [22].

m			0.1	0.3	0.5	0.1	0.3	0.5	0.1	0.3	0.5
α	β	n	$\lambda_1^{0.5}$			$\lambda_2^{0.5}$			$\lambda_3^{0.5}$		
0.1	0.1	10	3.774807695	4.067949377	4.337213788	21.75779577	20.79139281	19.92915467	59.46120158	54.82834794	49.41581682
		11	3.774807723	4.068143059	4.343666592	21.75779543	20.78985279	19.86458501	59.46120580	54.85756630	50.22423507
		12	3.774807730	4.068186021	4.345994791	21.75779523	20.78952742	19.84211264	59.46121233	54.86326081	50.50181950
	0.3	10	3.697515147	3.976321239	4.224448006	20.87772468	19.93742838	19.17903891	56.71925318	52.19883848	46.19996609
		11	3.697515809	3.976905112	4.234493729	20.87771875	19.93267116	19.06446756	56.71944372	52.28107888	47.47786187
		12	3.697515886	3.977054772	4.238457953	20.87771795	19.93150593	19.02083923	56.71947012	52.29965745	47.98482596
	0.5	10	3.619758168	3.883610232	4.110578890	20.02437096	19.11689913	18.50295995	54.08182281	49.58665199	42.82219131
		11	3.619765010	3.885029875	4.124377181	20.02431395	19.10475685	18.31512383	54.08336058	49.78018497	44.63402941
		12	3.619766060	3.885442817	4.130262853	20.02430559	19.10137031	18.23778852	54.08357357	49.83028673	45.46656601
0.3	0.1	10	4.089327929	4.405613347	4.696051132	23.09405259	22.08758096	21.19502381	62.73822382	57.91292479	52.22541732
		11	4.089327958	4.405828027	4.703310464	23.09405244	22.08587953	21.12309346	62.73822672	57.94391158	53.09553917
		12	4.089327962	4.405875683	4.705935045	23.09405242	22.08551914	21.09800501	62.73822707	57.94998637	53.39590245
	0.3	10	4.006319354	4.307298451	4.574717445	22.16972544	21.18990813	20.41091982	59.87325869	55.15978157	48.82740849
		11	4.006320082	4.307947454	4.586089930	22.16971864	21.18463791	20.28304130	59.87346718	55.24755873	50.20386301
		12	4.006320163	4.308113965	4.590590916	22.16971807	21.18334354	20.23425368	59.87348610	55.26749301	50.75304371
	0.5	10	3.922799628	4.207764588	4.451915622	21.27295768	20.32726667	19.70772255	57.11587260	52.42046456	45.24897872
		11	3.922807178	4.209347774	4.467671149	21.27289517	20.31378612	19.49760721	57.11747571	52.62786697	47.20079372
		12	3.922808331	4.209808809	4.474422331	21.27288603	20.31001747	19.41097721	57.11769479	52.68181883	48.10294300
0.5	0.1	10	4.427668506	4.768671219	5.081696407	24.50132857	23.45420760	22.53180409	66.17040802	61.14750898	55.17234916
		11	4.427668544	4.768909148	5.089861582	24.50132813	23.45232755	22.45168775	66.17041918	61.18036587	56.10885687
		12	4.427668548	4.768962013	5.092819853	24.50132797	23.45192813	22.42368220	66.17042581	61.18686686	56.43395687
	0.3	10	4.338601584	4.663281351	4.951250236	23.53107571	22.51113031	21.71310362	63.17826476	58.26615643	51.58214740
		11	4.338602384	4.664002713	4.964120448	23.53106839	22.50529254	21.57038700	63.17846629	58.35983036	53.06481939
		12	4.338602476	4.664187977	4.969229241	23.53106769	22.50385538	21.51583522	63.17848743	58.38120476	53.65986062
	0.5	10	4.248972688	4.556523487	4.818916435	22.58922467	21.60477009	20.98298716	60.29680000	55.39466571	47.79124630
		11	4.248981012	4.558289020	4.836894732	22.58915582	21.58980682	20.74795158	60.29846285	55.61688195	49.89396579
		12	4.248982290	4.558803774	4.844632918	22.58914625	21.58561283	20.65091464	60.29868767	55.67499614	50.87174436

Table 4-12 Non-dimensional first three natural frequencies of an exponentially tapered cantilever beam with trigonometric material property variation function [22].

m			0.1	0.3	0.5	0.1	0.3	0.5	0.1	0.3	0.5
α	β	n	$\lambda_1^{0.5}$			$\lambda_2^{0.5}$			$\lambda_3^{0.5}$		
0.1	0.1	8	3.676879978	3.964207322	4.192931563	21.57962715	20.64077731	20.19718216	59.28480525	54.23978335	44.89485370
		9	3.676880519	3.966057465	4.222929949	21.57961969	20.62427486	19.86696360	59.28452282	54.58631929	47.98140004
		10	3.676880557	3.966523047	4.235721433	21.57961896	20.62036976	19.73786085	59.28451890	54.66853694	49.55199534
	0.3	8	3.664670858	3.947087574	4.160167488	21.32948707	20.40510749	20.12464674	58.39750179	53.20870761	43.18053891
		9	3.664673902	3.950202992	4.197029167	21.32945921	20.37795002	19.69630484	58.39557545	53.68714812	46.57990714
		10	3.664674227	3.951058050	4.213660716	21.32945625	20.37088135	19.52081161	58.39546220	53.81356538	48.45398276
	0.5	8	3.639257355	3.907576152	4.083082209	20.80827864	19.94804090	20.19509324	56.56333114	50.81859560	39.19215038
		9	3.639297264	3.915700006	4.136732211	20.80805402	19.87694467	19.45228053	56.53904439	51.69495763	43.24642643
		10	3.639303532	3.918351965	4.164023204	20.80801460	19.85460767	19.12272688	56.53637759	51.98623828	45.83541746
0.3	0.1	8	3.804191279	4.100457368	4.335269838	22.04239650	21.09507792	20.66985421	60.39187033	55.28127651	45.71175839
		9	3.804191840	4.102398748	4.366974240	22.04238949	21.07776311	20.32111583	60.39151593	55.63626949	48.89132280
		10	3.804191883	4.102887674	4.380520972	22.04238853	21.07365709	20.18467384	60.39151828	55.72086408	50.51602942
	0.3	8	3.791704949	4.082916908	4.301237112	21.78958894	20.85730947	20.60492779	59.49608549	54.23634354	43.95553025
		9	3.791708123	4.086188038	4.340231860	21.78956059	20.82880166	20.15209340	59.49393733	54.72639853	47.45783057
		10	3.791708462	4.087086687	4.357869578	21.78955742	20.82136582	19.96651008	59.49380914	54.85649195	49.39627994
	0.5	8	3.765720307	4.042325598	4.220816805	21.26289703	20.39770353	20.70650293	57.64635201	51.81191609	39.86055993
		9	3.765761777	4.050868445	4.277680656	21.26267571	20.32305343	19.91857424	57.61980846	52.70859692	44.04204169
		10	3.765768305	4.053661117	4.306714672	21.26263600	20.29954698	19.56953748	57.61687890	53.00831154	46.71906034
0.5	0.1	8	4.091465481	4.407501808	4.655359894	23.06678266	22.10267409	21.72639019	62.82518287	57.57127996	47.47717596
		9	4.091466096	4.409657942	4.691129386	23.06677440	22.08339050	21.33223832	62.82471671	57.94674920	50.87755255
		10	4.091466140	4.410201938	4.706483139	23.06677381	22.07879702	21.17787373	62.82470703	58.03713700	52.63258670
	0.3	8	4.078397165	4.389061725	4.618412314	22.80836361	21.86070293	21.68131418	61.91166943	56.49560355	45.62316237
		9	4.078400631	4.392699833	4.662495599	22.80833391	21.82892452	21.16821317	61.90898215	57.01363533	49.36961854
		10	4.078400994	4.393701472	4.682545365	22.80833063	21.82059676	20.95795275	61.90880908	57.15273842	51.46268467
	0.5	8	4.051216142	4.346114258	4.530238129	22.27017076	21.39679096	21.86312530	60.03022176	53.99421814	41.27695390
		9	4.051261172	4.355647342	4.594781236	22.26995852	21.31353497	20.96268029	59.99806923	54.93955938	45.76157276
		10	4.051268313	4.358773669	4.628009455	22.26991847	21.28719302	20.56575448	59.99444217	55.25972580	48.64898529

Table 4-13 Non-dimensional first three natural frequencies of a cosine tapered cantilever beam with exponential material property variation function [22].

m			0.1	0.3	0.5	0.1	0.3	0.5	0.1	0.3	0.5
α	β	n	$\lambda_1^{0.5}$			$\lambda_2^{0.5}$			$\lambda_3^{0.5}$		
0.1	0.1	7	3.649748214	3.857009579	4.386596820	22.23247164	22.15107687	21.73358335	61.72498047	60.57454527	---
		8	3.649748214	3.856953376	4.355312415	22.23247206	22.15256203	21.92565881	61.72374165	60.35051970	---
		9	3.649748214	3.856945662	4.342090107	22.23247209	22.15273613	21.99392380	61.72370639	60.32530078	58.90897462
	0.3	7	3.578102389	3.779834305	4.288040165	21.34177214	21.25295273	20.98229283	58.90085318	57.95378911	---
		8	3.578103962	3.779914460	4.265308116	21.34175569	21.25386365	21.06865676	58.89261085	57.58869320	---
		9	3.578104084	3.779928758	4.253559118	21.34175448	21.25393910	21.09547200	58.89216588	57.53903060	56.35781706
	0.5	7	3.505948605	3.701104920	4.174565323	20.47792498	20.39142445	20.41308583	56.17474902	55.27742134	---
		8	3.505988956	3.702113400	4.167672462	20.47745272	20.38447850	20.32380318	56.16846900	54.90900937	---
		9	3.505994079	3.702342551	4.161701609	20.47739581	20.38273838	20.26393946	56.16881771	54.85704337	53.47666985
0.3	0.1	7	3.954307029	4.176370516	4.744507964	23.58898170	23.51251015	23.05298428	65.09557529	63.94495280	---
		8	3.954307029	4.176305824	4.709741772	23.58898227	23.51428409	23.28278870	65.09417529	63.68951658	---
		9	3.954307029	4.176296995	4.695121463	23.58898222	23.51449336	23.36539068	65.09413723	63.66058774	62.42325731
	0.3	7	3.877325943	4.093555102	4.638642026	22.65393618	22.56897319	22.26362513	62.14768290	61.23434907	---
		8	3.877327640	4.093634717	4.613325854	22.65392078	22.57036466	22.38111068	62.13791551	60.80791929	---
		9	3.877327778	4.093649224	4.600372879	22.65391914	22.57050935	22.42021940	62.13739749	60.74952971	59.81752643
	0.5	7	3.799789172	4.009035313	4.516086970	21.74657926	21.66357528	21.67247058	59.30303870	58.47170208	---
		8	3.799833234	4.010128327	4.508344610	21.74608384	21.65675371	21.60101937	59.29200966	58.01301316	---
		9	3.799838844	4.010378083	4.501875550	21.74602290	21.65499165	21.54674092	59.29196572	57.94636255	56.83673631
0.5	0.1	7	4.281996278	4.519682294	5.128769125	25.01688285	24.94642790	24.43774316	68.62385227	67.47890542	---
		8	4.281996278	4.519607677	5.090065723	25.01688340	24.94854193	24.71152719	68.62228358	67.18756419	---
		9	4.281996278	4.519597558	5.073873520	25.01688351	24.94879283	24.81105022	68.62222725	67.15438486	66.14539974
	0.3	7	4.199355536	4.430897173	5.015181840	24.03585333	23.95570256	23.60809599	65.54830372	64.68049296	---
		8	4.199357372	4.430974194	4.986897591	24.03583948	23.95768733	23.76291307	65.53678655	64.18296291	---
		9	4.199357515	4.430988617	4.972578212	24.03583826	23.95791934	23.81707234	65.53613879	64.11441511	63.50235877
	0.5	7	4.116107354	4.340244718	4.882929535	23.08334673	23.00468255	22.99405625	62.58169822	61.83604662	---
		8	4.116155409	4.341426136	4.874123480	23.08282954	22.99813878	22.94608988	62.56508161	61.27022321	---
		9	4.116161544	4.341697722	4.867063949	23.08276559	22.99638011	22.89989960	62.56453413	61.18617397	60.43339131

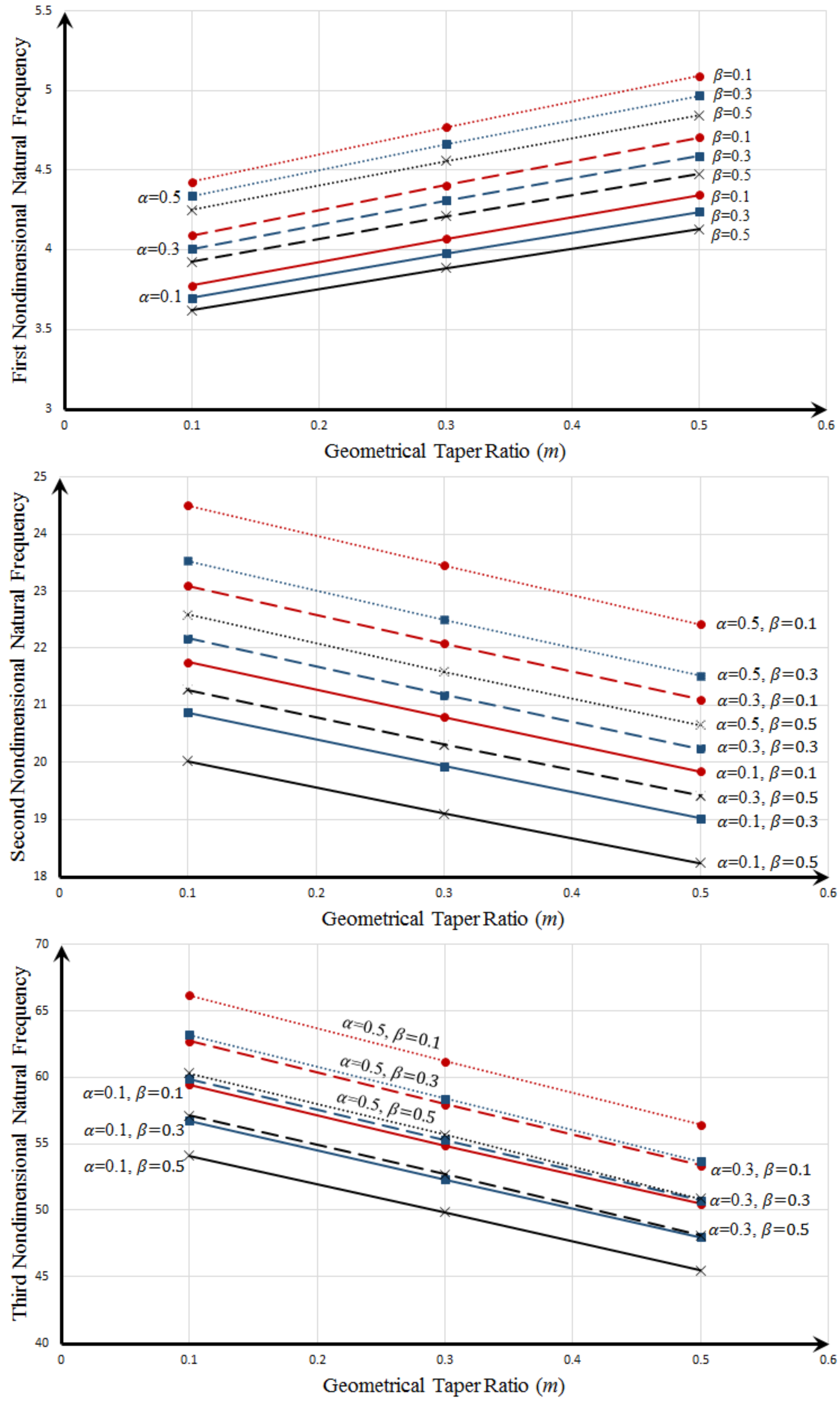

Fig. 4-9 First three non-dimensional natural frequencies variation with respect to geometry, density, and elasticity taper ratios for an exponentially tapered cantilever beam with exponential material property variation function [22].

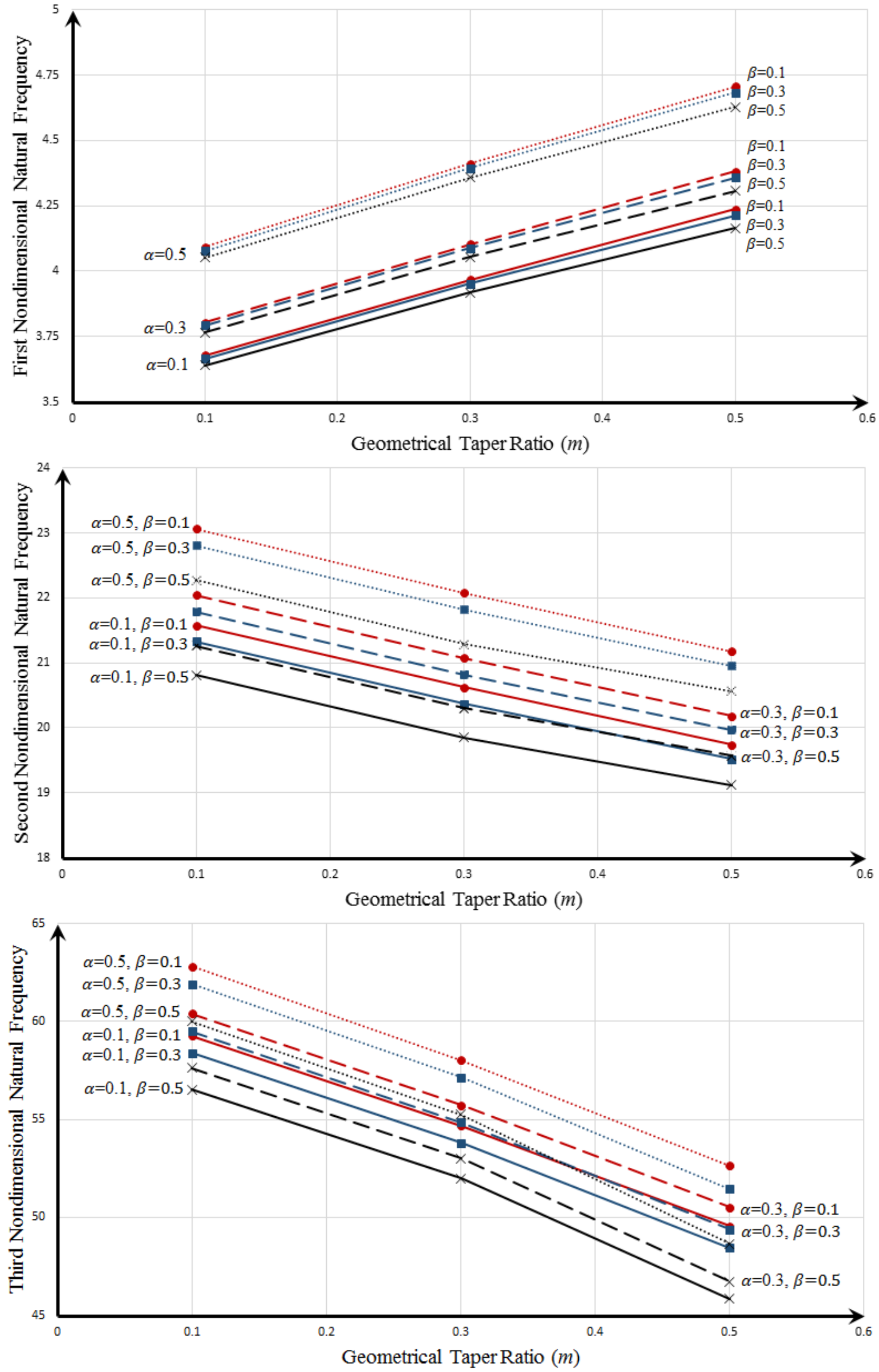

Fig. 4-10 First three non-dimensional natural frequencies variation with respect to geometry, density, and elasticity taper ratios for an exponentially tapered cantilever beam with cosine material property variation function [22].

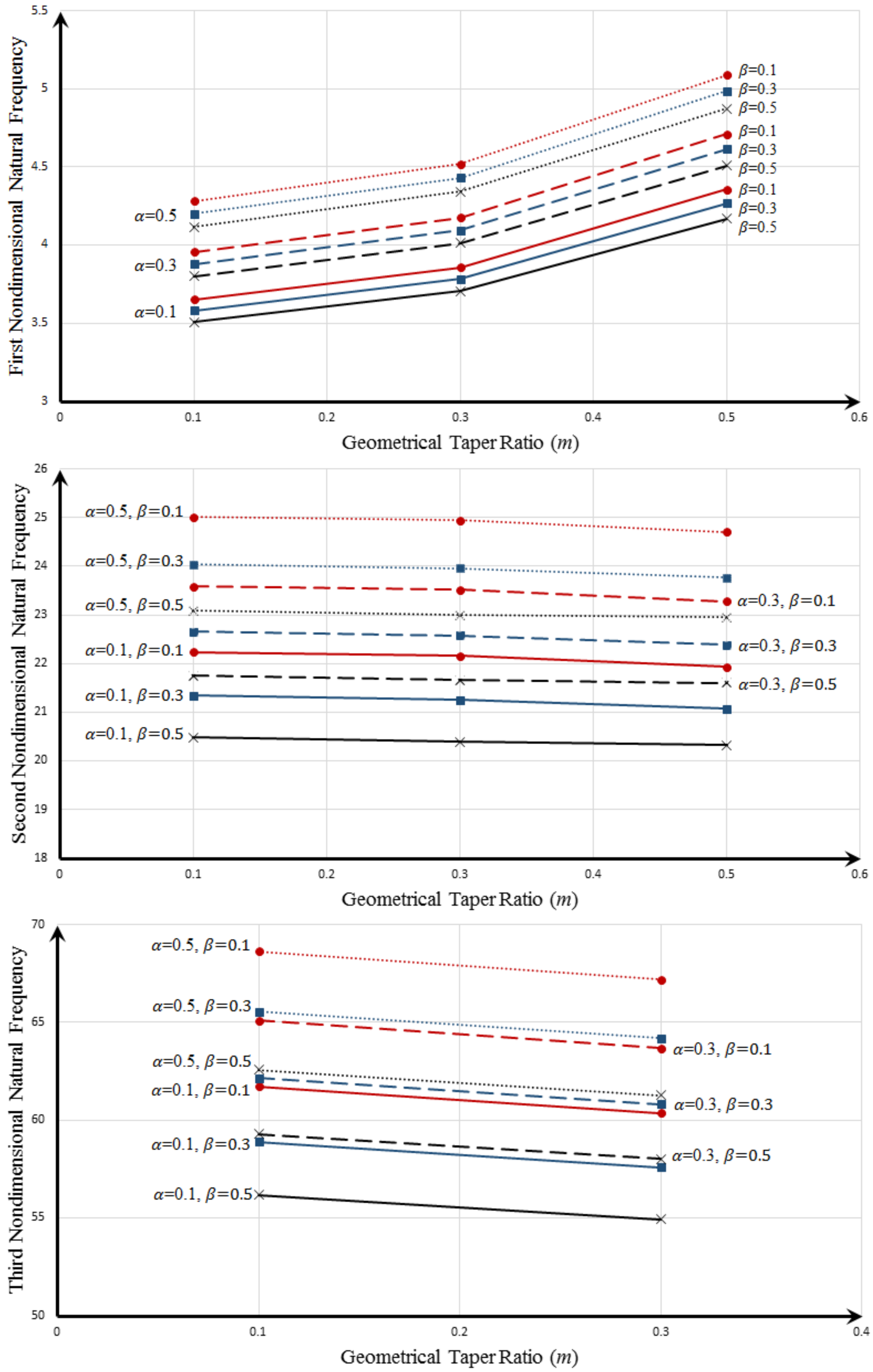

Fig. 4-11 First three non-dimensional natural frequencies variation with respect to geometry, density, and elasticity taper ratios for a trigonometrically tapered cantilever beam with exponential material property variation function [22].

4.3 Summary and Conclusions

The literature on the dynamic solution of non-uniform structures is limited. The objective of this section of the thesis was to present a unified theoretical approach to derive and analyze the vibration response of the nonlinearly tapered beams with axially FGM properties within the framework of Euler–Bernoulli beam theory.

A new mathematical model based on ADM was introduced to find the closed-form series solution. For non-uniform beams with different geometrical and material taper ratios, natural frequencies and corresponding mode shape functions were calculated. The efficiency and effectiveness of the method were validated by experimental test and comparison with existing numerical results. Perfect agreement with previously published and test results demonstrated the accuracy and rapid convergence of the proposed technique. It should be noted that the residual error in approximating a function by its *n*th degree Taylor polynomial could be high. This approximation error can be reduced by considering more terms of the polynomials for most of the functions. However, considering more terms leads to greater mathematical calculation intensity and decreases the computational efficiency of the model. On the other hand, the final vibration solution can be enhanced by considering more terms of the mode shape function series in ADM. In order to effectively suggest the number of required functions, the convergence study corresponding to the non-uniformity functions of the considered structure should be done [1], [22].

Finally, nonlinearly tapered cone beams with nonlinear FGM properties were investigated and presented for the first time. The proposed approach is capable of solving the vibration response of a beam with general nonlinear geometry profile, axially gradient material properties, and boundary conditions. Based on this analytical model, ideal non-uniform structural design can be attained for stability enhancement, energy harvesting, and many other engineering applications [22].

Chapter 5

5 Flutter and Buckling Enhancement

In this chapter, the proposed vibration model is applied to nonlinearly tapered beams with perfectly surface bonded piezoelectric layers subjected to a compressive follower force. Natural frequencies and mode shape functions are analytically derived and then flutter and buckling capacities are calculated. Furthermore, from the optimum structural design perspective, effects of follower force, tapering ratio, boundary condition, and voltage applied to the piezoelectric layer on the structural stability are thoroughly studied and presented.

This chapter of the thesis is reproduced with some modifications from [A. Keshmiri, N. Wu "Structural stability enhancement by nonlinear geometry design and piezoelectric layers", Journal of Vibration and Control, 25(3) 695–710, 2019] with permission from the "SAGE Publications".

5.1 Stability Analysis of Non-uniform Smart Beams

The problem under consideration is a nonlinearly tapered beam of length L having one fixed end at x=0 and constrained transversely by a spring with stiffness K at x=L, as shown in Fig. 5-1. Additionally, a pair of piezoelectric actuator is mounted on both sides of the beam with poling direction oriented in the transverse direction [50]. By applying the external voltage V to both piezoelectric layers, a tensile stress will be induced in the structure, which can be used to enhance the flutter and buckling capacities [119]. It is noted that the model analyzes global buckling of the structure, which leads to structural failure and eventually results in zero loading capacity and natural frequency. Here, there is no consideration of the local buckling issue. This can be an important future work in this area.

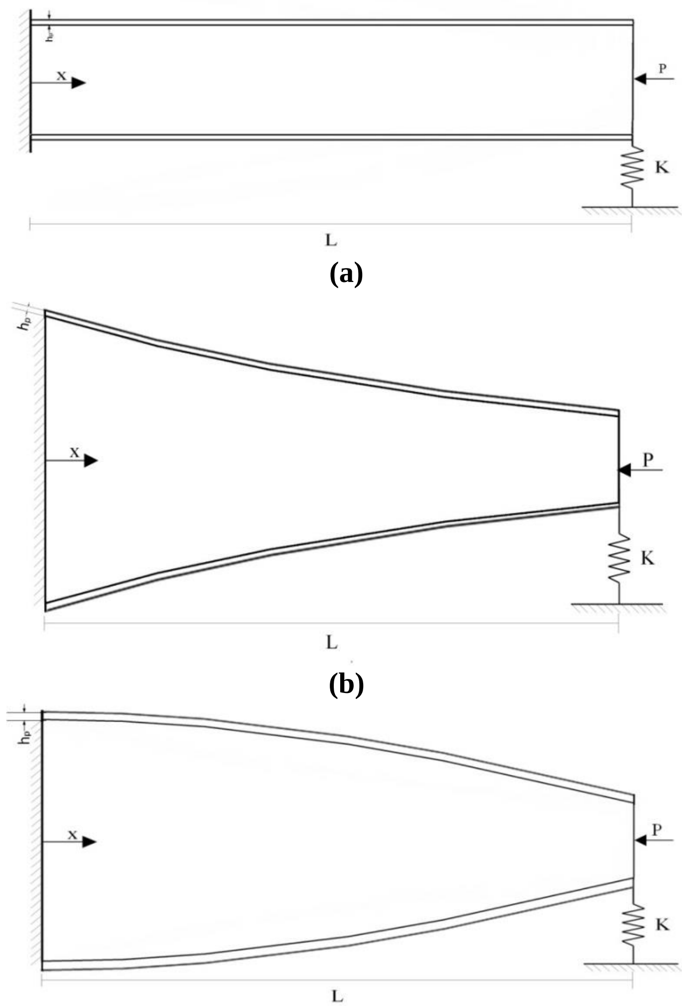

(c)

Fig. 5-1 Piezoelectric coupled beam of length L having one fixed end at x=0 and constrained transversely by a spring with stiffness K at x=L [50]. (a) Uniform. (b) Exponentially tapered. (c) Trigonometrically tapered.

Based on [119] and [120], the stress generated in perfectly surface bonded piezoelectric patches considering the electromechanical effect is defined as,

$$\sigma_x = -E_p z \frac{\partial^2 w(x,t)}{\partial x^2} - e_{31} E_e, \tag{5-1}$$

where E_p is the elasticity modulus of piezoelectric material, z is distance from neutral axis in transverse direction, $w(x,t)$ is displacement in transverse direction, e_{31} is piezoelectric coefficient, and E_e is the external electric field applied to the piezoelectric layers [50].

The first term represents the contribution of piezoelectric stiffness and the second term induces a uniform load F_p between actuators and the host structure which is expressed by,

$$F_p(x) = -2b(x)h_p E_e e_{31} = -2b(x)e_{31}V, \tag{5-2}$$

where $b(x)$ is width of the beam, h_p is thickness of the piezoelectric layer, and for a uniform electric field $E_e = V/h_p$ [50].

It should be noted that due to variable geometry profile, the induced tensile force by actuators has two variable horizontal and vertical components along the axial direction of the beam, Fig. 5-2. The horizontal component generates the uniform tensile load in the host beam with certain electrical voltage applied to the piezoelectric layers. On the other hand, the vertical components get canceled by the same amount of load on the other piezoelectric bonded surface of the structure

[50]. Consequently, the effective component of the induced force by actuators in stability enhancement can be calculated as,

$$F_p^x(x) = F_p(x)\cos\big(\theta(x)\big) = F_p(x)\left\{1 + \left[\tan\big(\theta(x)\big)\right]^2\right\}^{-1/2} = F_p(x)\left[1 + \left(\frac{d}{dx}h(x)\right)^2\right]^{-1/2}, \tag{5-3}$$

where θ(*x*) is the variable tangential angle shown in Fig. 5-2 and *h*(*x*) is the thickness geometry variation function [50].

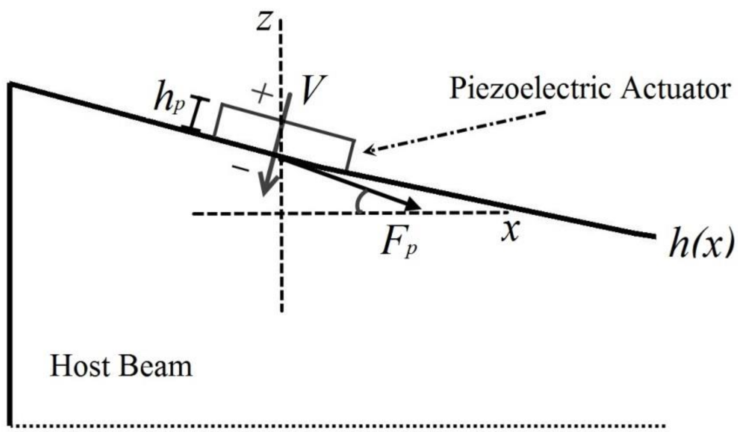

Fig. 5-2 A piezoelectric element bonded to the surface of a non-uniform structure under external voltage with two horizontal and vertical induced tensile force components [50].

The differential equation governing the elastic equilibrium of a homogeneous non-uniform smart beam subjected to a follower force *P* is expressed by,

$$\left(\rho A(x) + \rho_p A_p(x)\right)\frac{\partial^2 w(x,t)}{\partial t^2} + \frac{\partial^2}{\partial x^2}\left[\left(EI(x) + E_p I_p(x)\right)\frac{\partial^2 w(x,t)}{\partial x^2}\right] + \left(P - F_p^x(x)\right)\frac{\partial^2 w(x,t)}{\partial x^2} = 0, \tag{5-4}$$

where ρ is mass density of the beam, $A(x)=b(x)h(x)$ is cross-sectional area of the host beam, ρ_p is mass density of the piezoelectric patch, $A_p(x)=h_p b(x)$ is cross-sectional area of the piezoelectric patch, E is elasticity modulus of the beam, $I(x) = \frac{1}{12}b(x)h(x)^3$ is the second moment of area of the beam, E_p is elasticity modulus of the piezoelectric patch, and $I_p(x) = \frac{1}{12}b(x)h_p^3 + A_p(x)\left(\frac{h(x)+h_p}{2}\right)^2$ is the second moment of area of the piezoelectric layers [50].

Moreover, boundary conditions are defined as,

$$[w(x,t)]_{x=0} = \left[\frac{\partial w(x,t)}{\partial x}\right]_{x=0} = 0,$$
$$\left[\frac{\partial^2 w(x,t)}{\partial x^2}\right]_{x=L} = \left[\frac{\partial^3 w(x,t)}{\partial x^3} - \frac{K}{EI_{end}} w(x,t)\right]_{x=L} = 0, \tag{5-5}$$

where I_{end} is the second moment of area at $x=L$ [50].

Following the same analytical process from Eq. (4-4) to Eq. (4-10), vibration mode shape functions in the recurrence format can be expressed as,

$$X_0(x) = C_1 + C_2 x + C_3\frac{x^2}{2!} + C_4\frac{x^3}{3!},$$
$$X_{k+1}(x) = -O_x^{-1}\left[2\left(\frac{E\frac{dI(x)}{dx}+E_p\frac{dI_p(x)}{dx}}{EI(x)+E_pI_p(x)}\right)\frac{\mathrm{d}^3X_k(x)}{\mathrm{d}x^3} + \left(\frac{E\frac{d^2I(x)}{dx^2}+E_p\frac{d^2I_p(x)}{dx^2}+P-F_p^x(x)}{EI(x)+E_pI_p(x)}\right)\frac{\mathrm{d}^2X_k(x)}{\mathrm{d}x^2} - \right. \tag{5-6}$$
$$\left.\omega^2\left(\frac{\rho A(x)+\rho_pA_p(x)}{EI(x)+E_pI_p(x)}\right)X_k(x)\right] \quad k \geq 0.$$

As a result, all X_k components are evaluated for a specific mode shape. Similarly, to simplify the recurrent fourfold integration process, functions related to the geometry and material property of the host beam and piezoelectric layers will be substituted by the appropriate Taylor series representation. Additionally, with constant external electrical voltage/field, small mass relative to the total mass, and greater natural frequencies than frequencies of concern, piezoelectric layers will perform quasi-statically compared to the dynamic response of the host beam [119]. Thus, the dynamics of piezoelectric layers can be ignored and replaced by the static model plus the generalized force. This can also reduce the severity of mathematical process [50].

In the same way, by applying four boundary conditions of the beam, a system of four equations with unknown constants is given. For the nontrivial solution, the determinant of the coefficients must be zero giving the eigenvalue problem. If there is no external axial load P, the frequency equation gives the ith eigenvalue related to the ith natural frequency of the beam. As the follower force increases, the two smallest roots of the eigenvalue problem which are the first two natural frequencies move closer to each other and then at some value of P, they become equal. This value of P corresponds to the flutter capacity of the non-uniform structure. On the other hand, the axial load at which the first natural frequency becomes zero is correspondent to the buckling load of the beam. Besides, by applying the external voltage to piezoelectric layers, a local tensile load will be generated in the structure that enhances the structural flutter and buckling capacities [50].

5.2 Stability Simulations and Discussion

So far, a theoretical method to analyze the stability of a nonlinearly tapered and piezoelectric coupled beam is formulated. Numerical examples are presented to demonstrate the effectiveness of the proposed methodology and study the flutter and buckling loads of different non-uniform smart beams with various taper ratios, boundary conditions, and actuator voltages. Here, results are presented in non-dimensional forms where non-dimensional frequency, non-dimensional follower force, and non-dimensional spring stiffness are defined as $\beta = \omega^2 \frac{\rho A_0}{EI_0}$, $\bar{P} = \frac{PL^2}{\pi^2 EI_0}$, and $k = \frac{KL^3}{EI_{end}}$, respectively [50].

Firstly, a uniform and homogeneous cantilever piezoelectric coupled beam with its free end constrained transversely by a spring with stiffness k is considered, Fig. 5-1(a). The loading capacity results are presented in non-dimensional forms in Table 5-1 and are compared to the results from [49], denoting that no piezoelectric actuator is attached to the beam. Good agreement can be seen which proves the efficiency, accuracy, and robustness of the proposed model. For $k \leq 36$, first two natural frequencies meet each other first, while the axial load increases, showing the flutter case. In contrast, higher values of k correspond to the buckling phenomenon, where the first natural frequency approaches zero earlier with the increment of the axial load. The value of P at which two first natural frequencies approach each other and the first natural frequency becomes zero first, are the flutter and buckling capacities of the structure, respectively [50].

Table 5-1 Non-dimensional flutter and buckling capacities for a homogeneous uniform beam with respect to different values of the non-dimensional spring support coefficient [50].

	k	$\bar{P}$	
		[49]	present method
Flutter	0	2.035	2.032
	10	2.456	2.454
	20	3.025	3.028
	30	3.635	3.629
Buckling	50	2.511	2.581
	65	2.361	2.416
	80	2.298	2.332
	120	2.187	2.225

Secondly, a homogeneous and exponentially tapered cantilever beam with its free end constrained transversely is considered, Fig. 5-1(b). In this case, variable thickness and width of the beam are defined as $h(x) = h_0 e^{-m\frac{x}{L}}$ and $b(x) = b_0 e^{-m\frac{x}{L}}$ where m, h_0, and b_0 are geometry taper ratio and thickness and width at the fixed end, respectively. It is worth mentioning that taper ratios along thickness and width of the beam are considered to be the same. In order to make reasonable stability comparison among beams with different tapering ratios, all of them are assumed to have equal length, volume, and mass. This means that h_0 and b_0 will be different for each geometrical taper ratio [50].

In non-dimensional forms, Fig. 5-3 illustrates the variation of non-dimensional natural frequency of an exponentially tapered beam with taper ratio of m=0.3 under different compressive follower forces for various spring stiffness values without piezoelectric effect [50].

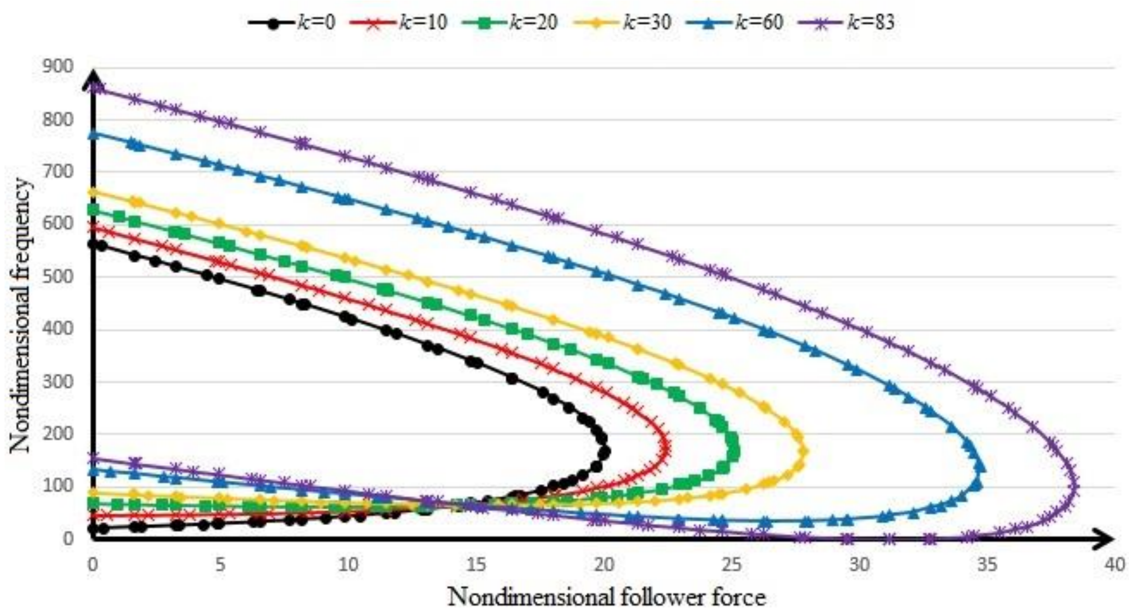

(a)

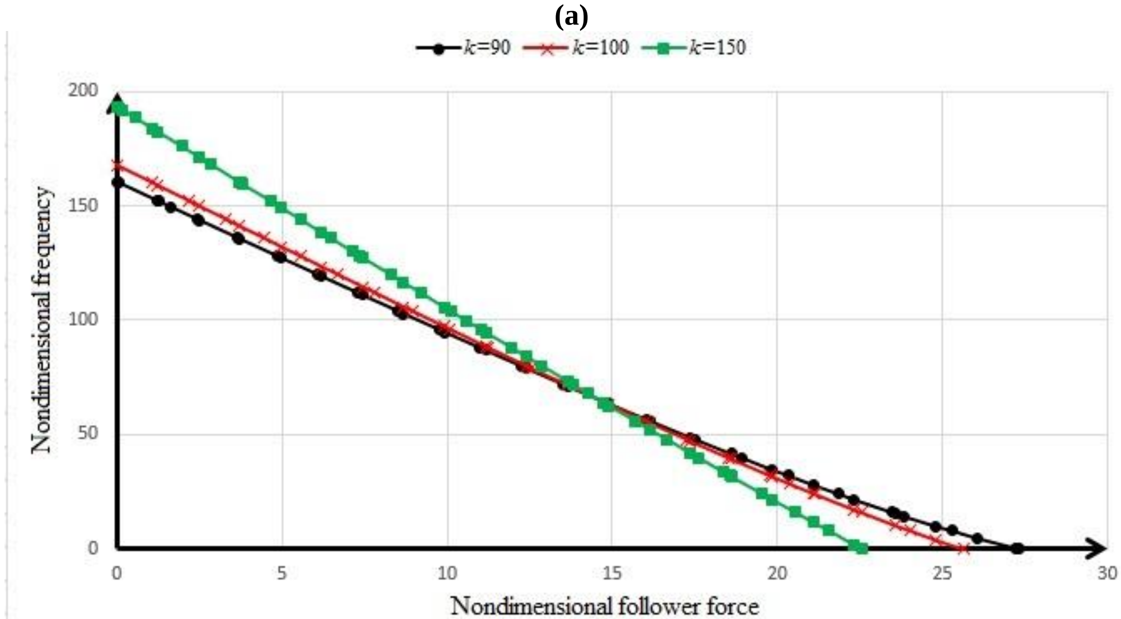

(b)

Fig. 5-3 Non-dimensional frequency versus non-dimensional follower force for an exponentially tapered beam with m=0.3 taper ratio and various non-dimensional spring coefficient [50]. (a) Non-dimensional flutter capacity. (b) Non-dimensional buckling capacity.

In Fig. 5-3(a) for k<83, beam flutter happens first. The first two natural frequencies are getting close to each other with the increment of the axial follower force before the first natural frequency reaches zero. However, increasing the axial follower force leads to lower first natural frequency until it becomes zero, Fig. 5-3(b) for $k \geq 83$. This means that the structure buckles first. Same phenomenon from the uniform beam was seen that increasing the non-dimensional spring coefficient results in lesser tendency to flutter in the structure, which is rational because of the restrictions at the beam boundary. For the same reason, stiffer boundary condition also results in less buckling capacity of the structure and definitely more instable behavior [50].

Fig. 5-4 shows the non-dimensional frequency versus non-dimensional follower force for an exponentially tapered beam with free end non-dimensional spring coefficient fixed as $k=0$ and $k=300$, zero external voltage, and various taper ratios. Based on Fig. 5-4(a) for the cantilever case ($k=0$), the structure flutters but does not buckle. By increasing the taper ratio from 0.1 to 0.7, non-dimensional flutter capacity of the beam drops from 20.3008 to 17.1523 which is the result of steep nonlinearity in the geometry. As discussed before, enlarging the non-dimensional stiffness coefficient of the beam free end spring triggers the buckling in the structure. For a certain boundary condition ($k=300$), non-dimensional buckling capacity also decreases from 20.9355 to 19.5525 by shifting the taper ratio from 0.1 to 0.7. This means that sharper nonlinear geometry or higher taper ratio makes the beam more susceptible to the buckling phenomenon, Fig. 5-4(b). Additionally, the nonlinear beam with taper ratio of m=0.8 still will not buckle under this level of constraint [50].

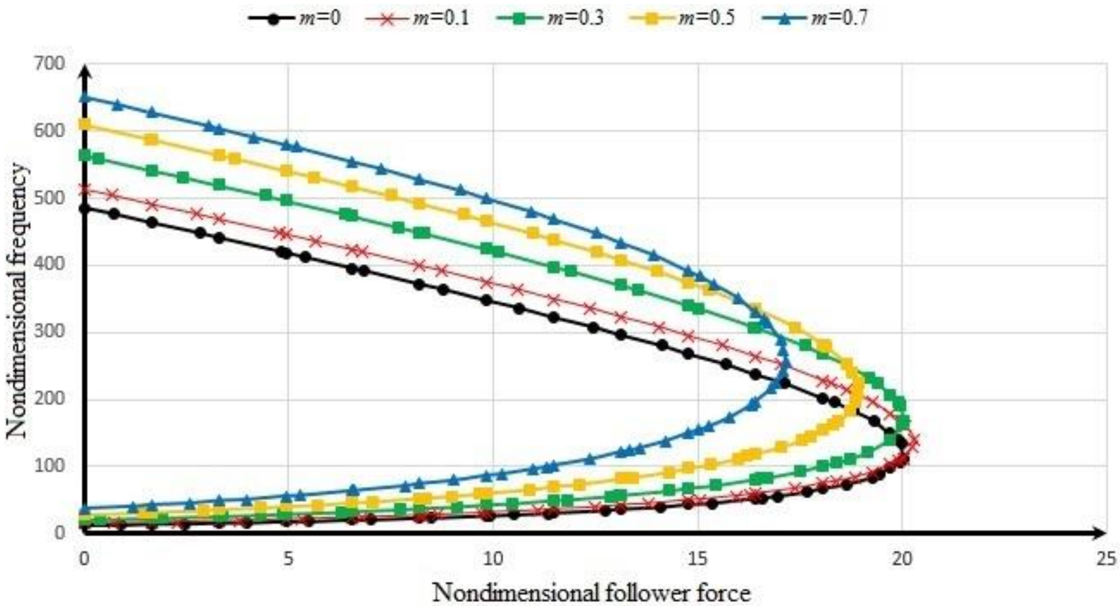

(a)

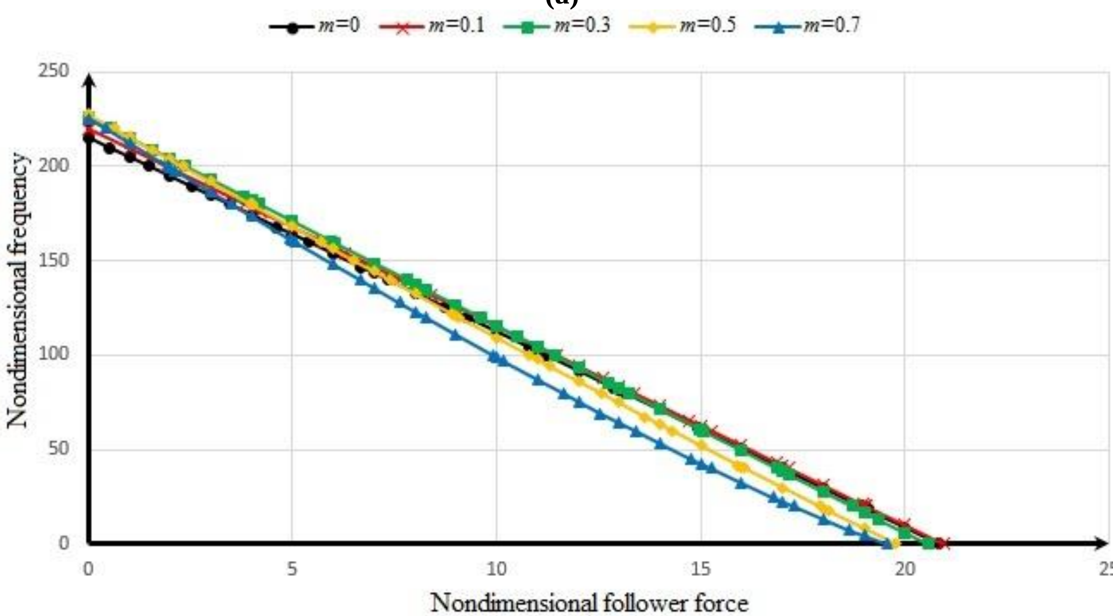

(b)

Fig. 5-4 Non-dimensional frequency versus non-dimensional follower force for an exponentially tapered beam with k=0 and k=300 non-dimensional spring coefficient and various taper ratio [50]. (a) Non-dimensional flutter capacity. (b) Non-dimensional buckling capacity.

Fig. 5-5 depicts the non-dimensional flutter and buckling capacities versus non-dimensional spring coefficient for an exponentially tapered beam with various taper ratios and zero external voltage. It is shown that a uniform beam has higher stability and flutter capacity only for very low values of the non-dimensional spring coefficient ($k \leq 36$). After the transition value from flutter instability to buckling with more rigid edge conditions, even very small nonlinearity in the geometry of the beam can significantly enhance the flutter and buckling capacities. For instance, non-dimensional buckling capacity of a uniform beam is increased from 22.358 to 25.593 for an exponentially $m=0.3$ tapered beam with the same volume/mass and boundary condition ($k=100$). This clearly shows 14.47% buckling capacity enhancement in the structure. The non-uniform geometrical profile can help to considerably improve the stability of structures with the same mass/weight or reduce the weight of the structure with required stability loading capacity. As a result, for a specified boundary condition imposed by external factors, the most stable and efficient geometrical design of the structure can be easily found. In addition, the nonlinear taper ratio of the beam affects the critical non-dimensional spring support stiffness value for the instability mode transition between flutter and buckling. When the taper ratio is changing from 0 to 0.8, the critical non-dimensional spring support stiffness varies from 33 to 310 [50].

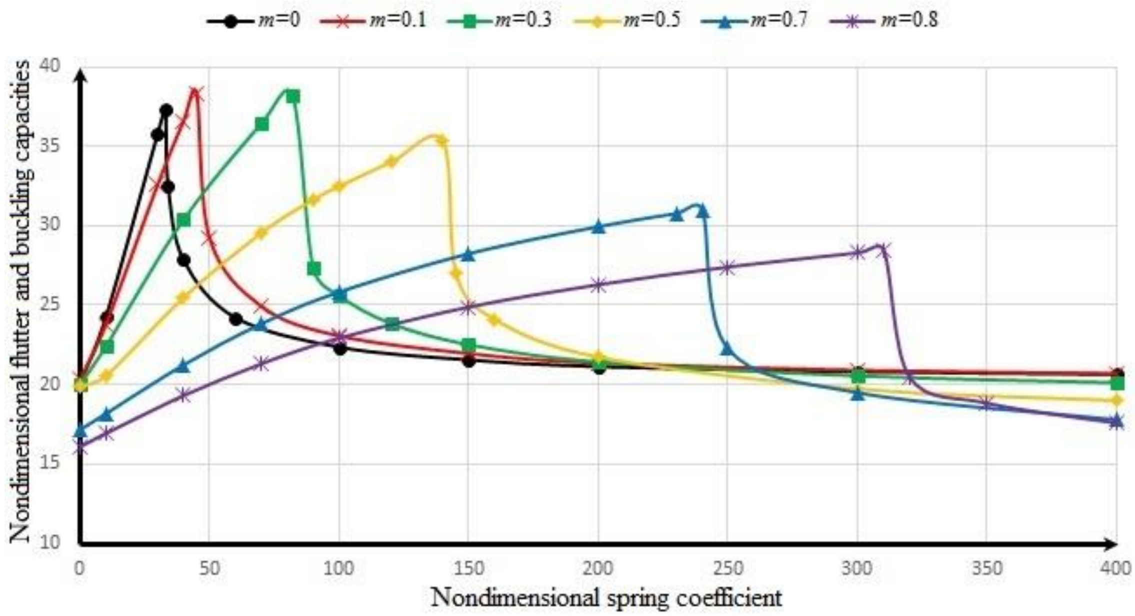

Fig. 5-5 Non-dimensional flutter and buckling capacities versus non-dimensional spring coefficient for an exponentially tapered beam with various taper ratios [50].

For the case where piezoelectric actuators are mounted on both sides of the beam, flutter and buckling capacities of the structure with various nonlinear geometrical taper ratios and degrees of restraint under different applied external voltages are plotted in Fig. 5-6. Here, width of the beam at the fixed end is assumed to be 0.08m and the piezoelectric coefficient is e_{31}=-9.29C/m^2. As depicted in the Fig. 5-6, increasing the actuator external voltage results in better stability of the beam with higher loading capacity. For instance, by applying V=30v, roughly 14% and 26% enhancement in flutter and buckling capacities of the non-uniform piezoelectric coupled beam with taper ratio of m=0.3 can be seen. Moreover, by comparing the plain uniform and nonlinear smart designs, even with small geometrical taper ratio m=0.3 and applied external voltage V=30v on piezoelectric layers, up to 20% structural stability improvement can be attained [50].

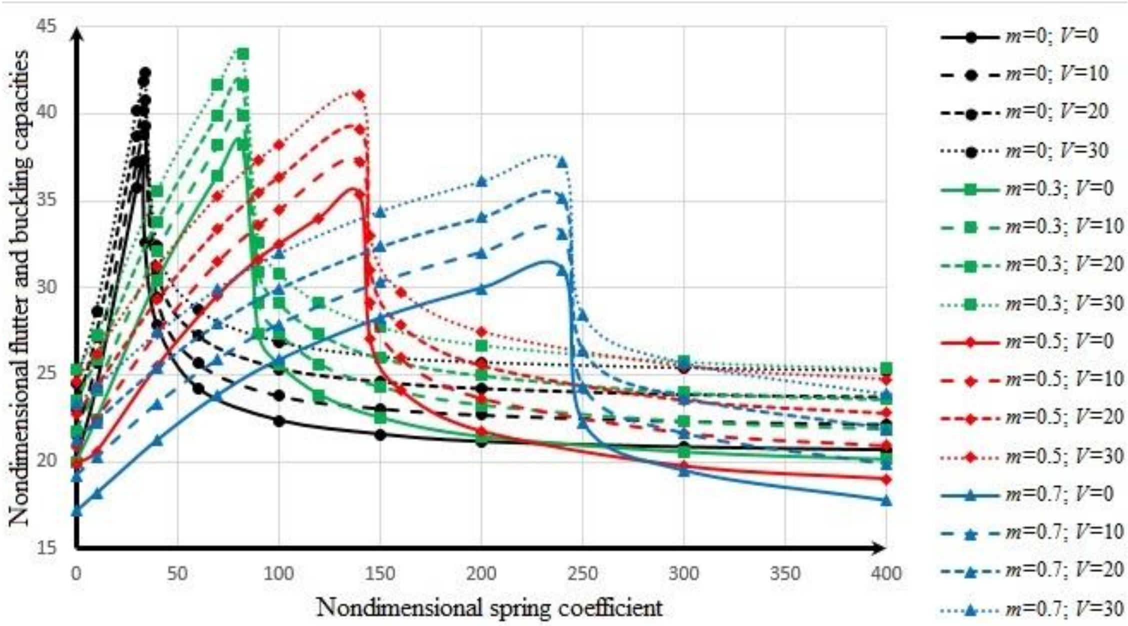

Fig. 5-6 Non-dimensional flutter and buckling capacities versus non-dimensional spring coefficient for an exponentially tapered beam with various taper ratio and applied actuation voltage [50].

Next, a homogeneous and cosine tapered cantilever beam with its free end constrained transversely is considered, Fig. 5-1(c). Here, variable thickness and width of the beam are defined as $h(x) = h_0\, cos\frac{m\pi x}{2L}$ and $b(x) = b_0\, cos\frac{m\pi x}{2L}$. Similar to the previous section, all of beams with different designs have identical length, volume, and mass. Stability analysis results are presented in Figs. 5-7 to 5-10 [50].

The variation of the first two non-dimensional natural frequencies with respect to non-dimensional follower force for the tapered beam with taper ratio of m=0.3 and no piezoelectric layers attached is represented in Fig. 5-7 [50].

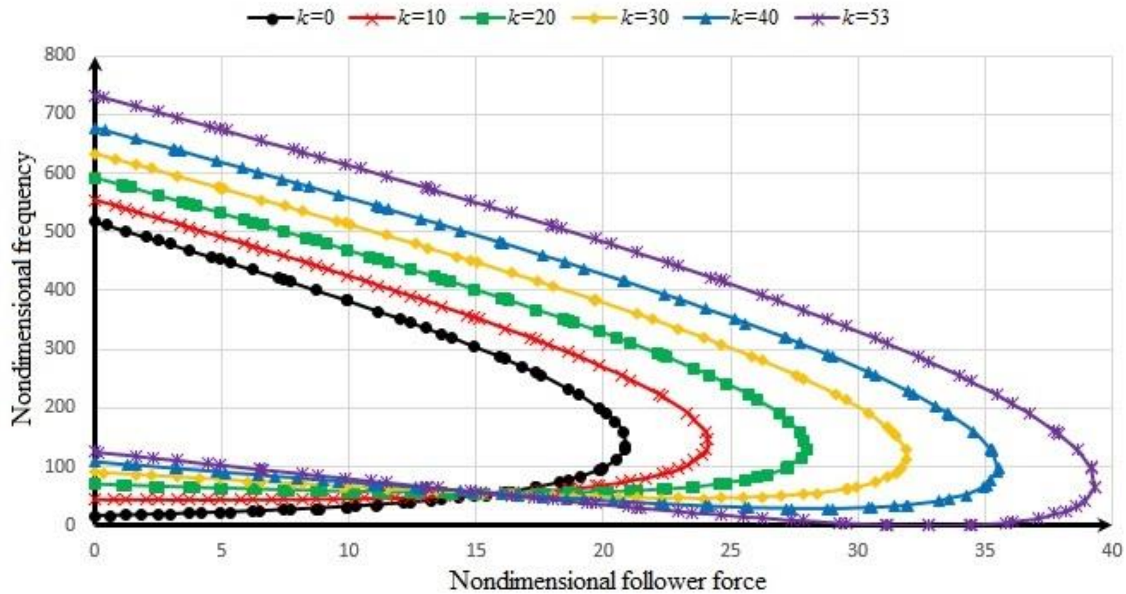

(a)

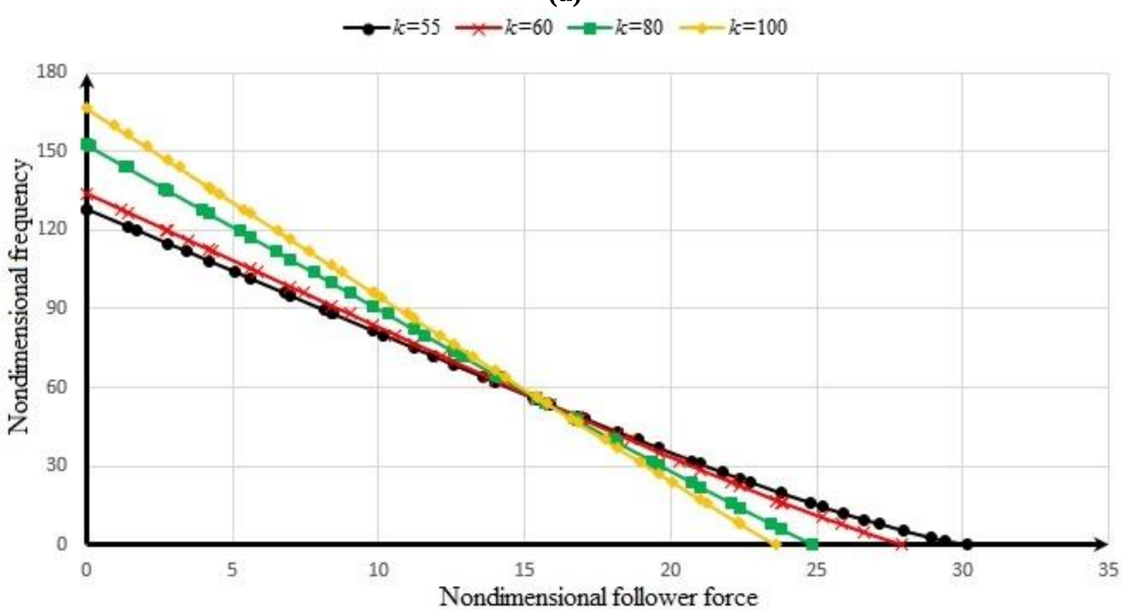

(b)

Fig. 5-7 Non-dimensional frequency versus non-dimensional follower force for a trigonometrically tapered beam with m=0.3 taper ratio and various non-dimensional spring coefficient [50]. (a) Non-dimensional flutter capacity. (b) Non-dimensional buckling capacity.

In Fig. 5-7(a) for k<53, first two natural frequencies approaches each other without passing zero which shows that the beam flutters. But for k≥53, first natural frequency passes through zero first and the structure buckles as shown in Fig. 5-

7(b). As discussed before, this logical trend is due to the variation of the spring support stiffness at the free end of the beam. Same incident from the last case study was seen that growing the non-dimensional spring stiffness caused higher flutter and less buckling capacities due to the constraints at the beam tip [50].

Fig. 5-8 presents the non-dimensional natural frequency versus non-dimensional follower force for a cosine tapered beam with non-dimensional spring coefficients k=0 and k=300, zero external voltage, and various taper ratios. For the cantilever beam (k=0), the structure flutters regardless of the geometry variation as seen in Fig. 5-8(a). In addition, it is noted that non-dimensional flutter capacity varies from 22.358 to 25.593 while the taper ratio increases from 0 to 0.7. Higher taper ratio results in a greater flutter capacity. Following the same idea, for a certain boundary condition rigidity (k=300), higher taper ratio makes the beam more resistant to the buckling, Fig. 5-8(b). Besides, very close geometry of the uniform and m=0.1 tapered beams leads to almost the same stability behavior [50].

The non-dimensional flutter and buckling capacities versus non-dimensional spring coefficient for a cosine tapered beam with various taper ratios and zero actuation voltage is displayed in Fig. 5-9. As mentioned before, a uniform beam has higher stability and flutter capacity only for very low values of the non-dimensional spring coefficient (k≤36). For relatively stiffer spring support and boundary conditions (55≤k≤250), nonlinearly tapered beam with different taper ratios (0.3≤*m*≤0.6) can provide up to 20.16% axial loading capacity enhancement [50].

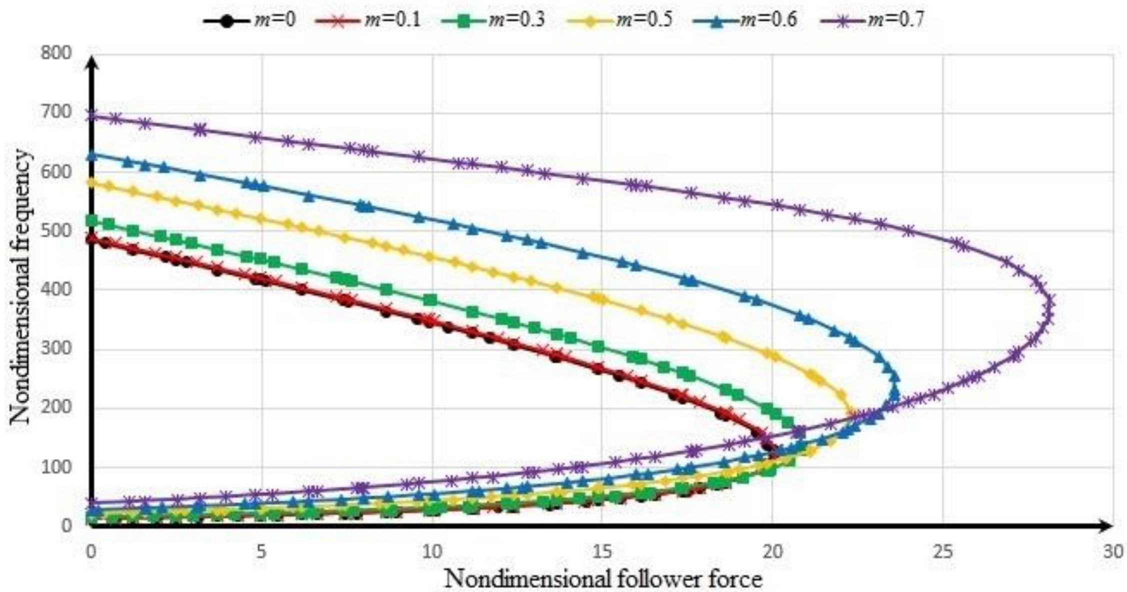

(a)

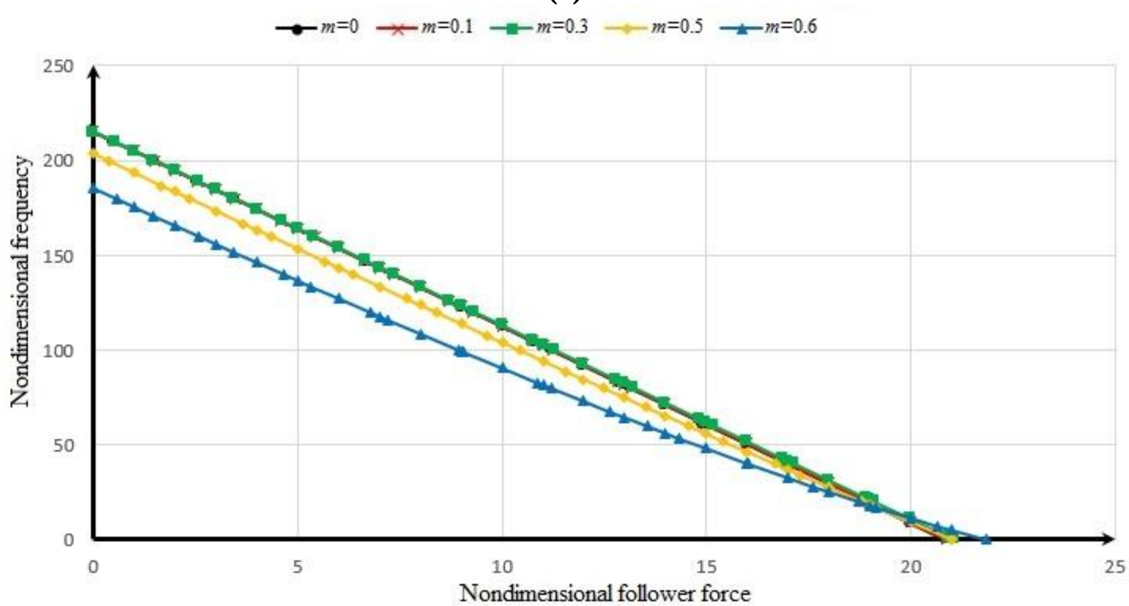

(b)

Fig. 5-8 Non-dimensional frequency versus non-dimensional follower force for a trigonometrically tapered homogeneous beam with k=0 and k=300 non-dimensional spring coefficient and various taper ratio [50]. (a) Non-dimensional flutter capacity. (b) Non-dimensional buckling capacity.

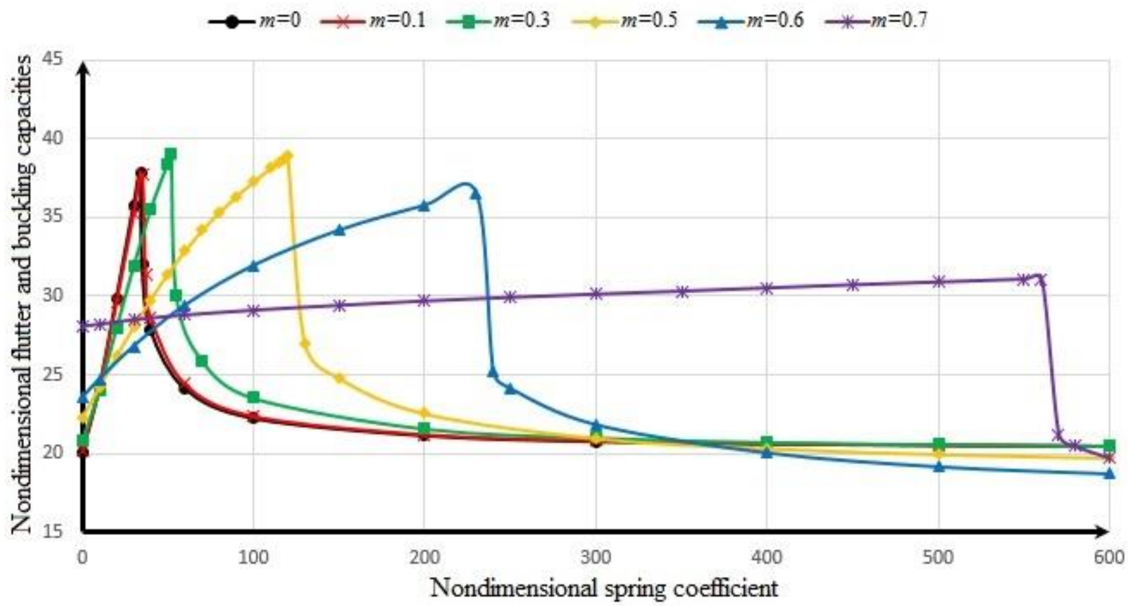

Fig. 5-9 Non-dimensional flutter and buckling capacities versus non-dimensional spring coefficient for a trigonometrically tapered beam with various taper ratios [50].

It can be concluded that for certain boundary conditions, nonlinear design of the beam can be efficiently optimized by considering either higher stability for specific mass value or lighter structure for certain loading capacity. With non-uniform beam design, the equivalent stiffness of the beam close to the fixed end is higher due to larger beam area which avoids further deformation induced by the higher moment. This can help to further improve the stiffness increment effect close to the beam fixed end. It is noted that with different boundary conditions of the beam, the nonlinear design would have different stability enhancement effects. Thus, various nonlinear functions should be employed to reach the best results which can be studied and determined by the analytical model proposed in this research [50].

Lastly, when piezoelectric actuators are attached to the structure, flutter and buckling capacities under different external voltages with various taper ratios and degrees of restraint are plotted in Fig. 5-10. Again as expected, increasing the actuation voltage leads to stability enhancement. For example, up to 18% and 45% growth in flutter and buckling capacities for the nonlinear design m=0.5 under V=30v actuation voltage can be achieved, respectively [50].

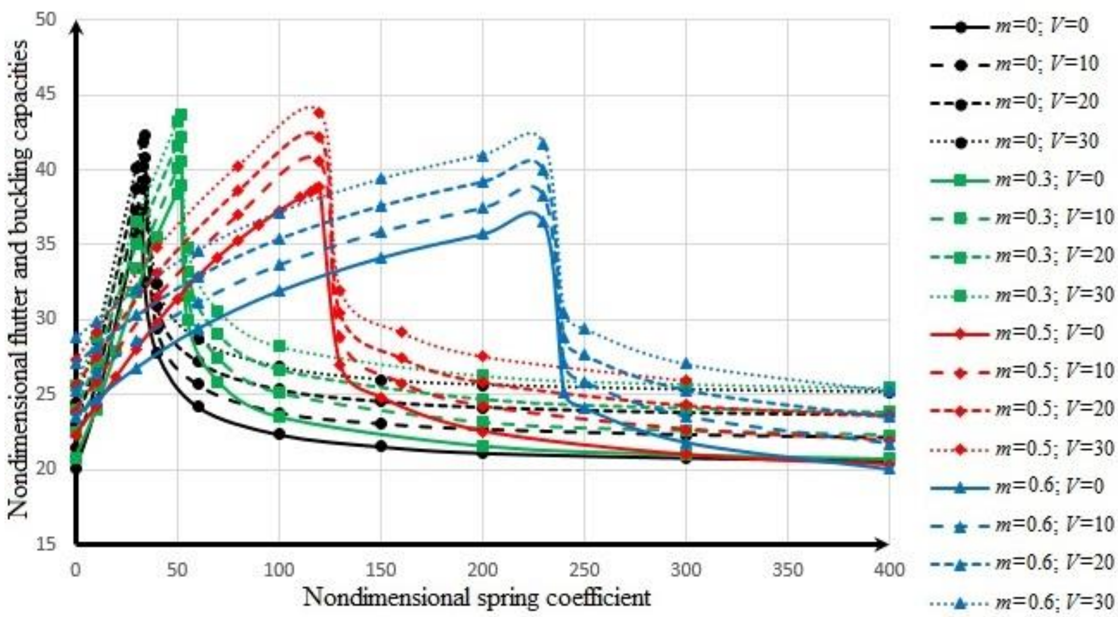

Fig. 5-10 Non-dimensional flutter and buckling capacities versus non-dimensional spring coefficient for a trigonometrically tapered beam with various taper ratios and applied actuation voltage [50].

5.3 Summary and Conclusions

This part of the research provided a new mathematical method to study the stability of nonlinearly tapered piezoelectric coupled beams under axial loads. Natural frequencies in addition to flutter and buckling loads of a non-uniform cantilever piezoelectric coupled beam with elastically restrained free tip were calculated theoretically and the results with various beam configurations were investigated. The current theoretical solution provides a good understanding of the physics of the problem for arbitrary non-uniform beams.

In summary, it is demonstrated that nonlinear geometry of the smart structure not only satisfies architectural and functional design requirements, but also considerably improves the stability of the system. Optimum structural design can be effectively achieved based on enhancement of flutter and buckling capacities by studying the effects of follower compressive load, non-uniform geometry, boundary condition, and actuation voltage. According to the numerical studies and by considering the same beam length, volume, and mass, the non-uniform design can show up to 45% higher flutter or buckling capacity for various degrees of restraint at the boundary. In other words, with similar buckling and flutter capacities, a non-uniform smart beam can be much lighter than the uniform one. Since tapered beams are widely used in modern structures, this superior stability behavior will be advantageous to many engineering applications [50].

Chapter 6

6 Piezoelectric Energy Harvester

This chapter of the thesis provides the theoretical development of four different piezoelectric energy harvesting systems. First, the electromechanical solution of a non-uniform FGM cantilever energy harvester is analytically presented. Then the model is used to design a broadband piezoelectric energy harvesting system capable of operating efficiently with high electrical outputs over a wide frequency domain. Next, a new design and analytical model for a composite energy harvester with embedded piezoelectric stacks by using in-plane polarization is investigated. Lastly, the optimum design of an energy harvesting platform by stacking up piezoelectric rings in the boundary of a non-uniform beam is presented.

6.1 Non-uniform Piezoelectric Energy Harvester

This section presents an analytical model for development of a piezoelectric energy harvester with nonlinear geometry and FGM properties based on the proposed theoretical methodology. The model is applied to geometrically and materially non-uniform beams with structural strain rate damping and surface bonded piezoelectric layers to derive the dynamic response of the smart structure to base motion excitation and efficiently harvest the subsequent vibrational energy.

Firstly, the steady state vibration response of the smart non-uniform beam subjected to a harmonic base motion is obtained and then electromechanical outputs of the piezoelectric patches are analytically derived. Furthermore, a comprehensive parametric study for bimorph piezoelectric energy harvesters is done. It is demonstrated that the novel non-uniform design can significantly increase the electromechanical output of the harvester [46].

This section of the thesis is reproduced with some modifications from [A. Keshmiri, N. Wu, Q. Wang “A new nonlinearly tapered FGM piezoelectric energy harvester”, Engineering Structures, 173, 52-60, 2018] with permission from the “Elsevier B.V.” and [A. Keshmiri, N. Wu “A wideband piezoelectric energy harvester design by using multiple non-uniform bimorphs”, Vibration, 1(1), 93-104, 2018] with permission from the “MDPI”.

6.1.1 Theoretical Model

The proposed piezoelectric energy harvester configuration consists of a nonlinearly tapered and FGM host cantilever beam and piezoelectric patches bonded on the top and bottom surfaces. The geometry of the structure is described by L length of the beam, $2b_0$ width of the beam at the fixed end, $2h_0$ thickness of the beam at the fixed end, and l_p and h_p length and thickness of the piezoelectric patch, respectively. The energy harvesting efficiency of the piezoelectric coupled cantilever beam is investigated by setting a harmonic base motion excitation [46]. Therefore, the mechanical vibration input for the system is achieved through $y(t) = -Ye^{j\varphi t}$, where Y is the amplitude of the base displacement, φ is the angular frequency of the harmonic excitation, and *j* is the unit imaginary number [121].

The differential equation that describes the forced lateral vibration of a smart beam with structural strain rate damping, non-uniform geometry, and axially FGM properties is expressed by,

$$\rho(x)A(x)\frac{\partial^2 w(x,t)}{\partial t^2} + \frac{\partial^2}{\partial x^2}\left[E(x)I(x)\frac{\partial^2 w(x,t)}{\partial x^2} + C_s(x)I(x)\frac{\partial^3 w(x,t)}{\partial x^2 \partial t}\right] = -\rho(x)A(x)\varphi^2 Ye^{j\varphi t}, \tag{6-1}$$

where *x* is the position variable along length of the beam, *t* is the time variable, $\rho(x)$ is the mass density, $A(x)$ is the cross-sectional area, $w(x,t)$ is the deflection function, $E(x)$ is the elasticity modulus, $I(x)$ is the second moment of area, and $C_s(x)$ is the strain rate damping coefficient [46].

Since the system is proportionally damped, the eigenfunctions are the normalized eigenfunctions of the corresponding undamped free vibration problem [122], [123], [124]. As a result, boundary conditions are defined as,

$$[w(x,t)]_{x=0} = \left[\frac{\partial w(x,t)}{\partial x}\right]_{x=0} = 0,$$
$$\left[E(x)I(x)\frac{\partial^2 w(x,t)}{\partial x^2}\right]_{x=L} = \left[\frac{\partial}{\partial x}\left(E(x)I(x)\frac{\partial^2 w(x,t)}{\partial x^2}\right)\right]_{x=L} = 0. \tag{6-2}$$

Following the same analytical process from Eq. (4-4) to Eq. (4-10), vibration mode shape functions in the recurrence format are derived as,

$$X_0(x) = C_1 + C_2 x + C_3 \frac{x^2}{2!} + C_4 \frac{x^3}{3!},$$

$$X_{k+1}(x) = -O_x^{-1}\left[2\left(\frac{\frac{dI(x)}{dx}}{I(x)} + \frac{\frac{dE(x)}{dx}}{E(x)}\right)\frac{\mathrm{d}^3 X_k(x)}{\mathrm{d}x^3} + \left(\frac{\frac{d^2 I(x)}{dx^2}}{I(x)} + \frac{\frac{d^2 E(x)}{dx^2}}{E(x)} + 2\frac{\frac{dI(x)}{dx}}{I(x)}\frac{\frac{dE(x)}{dx}}{E(x)}\right)\frac{\mathrm{d}^2 X_k(x)}{\mathrm{d}x^2} - \omega^2\left(\frac{\rho(x)A(x)}{E(x)I(x)}\right)X_k(x)\right] \quad k \geq 0. \tag{6-3}$$

Therefore, all X_k components are evaluated for a specific mode shape. Similarly, to simplify the recurrent fourfold integration process, functions related to the geometry and material property will be substituted by the appropriate Taylor series representation. Correspondingly, by applying four boundary conditions, a system of four equations with unknown constants is given. For the nontrivial solution, the determinant of the coefficients must be zero giving the eigenvalue problem [1], [22]. Consequently, the ith eigenvalue and natural frequency of the structure considering n-term mode shape function approximation is evaluated [46].

Obviously, mass normalized normal mode eigenfunctions satisfy the orthogonality conditions, Eq. (4-5). Since in general, the damping function does not possess the orthogonality property [125], it is assumed that the structural damping is in the form of $C_s(x)=\alpha E(x)$ where α is a constant. Consequently, the modal participation coefficients $T_i(t)$ are the solution of the ordinary differential equation,

$$\frac{\mathrm{d}^2 T_i(t)}{\mathrm{d}t^2} + 2\xi_i\omega_i\frac{dT_i(t)}{dt} + {\omega_i}^2 T_i(t) = -\varphi^2 Y\left(\int_0^L X_i(x)\rho(x)A(x)\mathrm{d}x\right)e^{j\varphi t}, \tag{6-4}$$

where $2\xi_i\omega_i=\alpha\omega_i^2$ and ξ_i is the structural strain rate damping ratio corresponding to the ith vibration mode [46].

The final solution of the Eq. (6-4) by Duhamel integral can be expressed as,

$$T_i(t) = \frac{-\varphi^2 Y}{\omega_{d_i}} \int_0^t \left[\left(\int_0^L X_i(x)\rho(x)A(x)\mathrm{d}x\right) e^{j\varphi\tau}\right] e^{-\xi_i\omega_i(t-\tau)} \sin\omega_{d_i}(t-\tau)\, d\tau, \tag{6-5}$$

where $\omega_{d_i} = \omega_i\sqrt{1-\xi_i{}^2}$ is the damped frequency corresponding to the ith vibration mode [46].

The steady state solution of Eq. (6-5) is expressed by,

$$T_i(t) = \frac{\varphi^2 Y \int_0^L X_i(x)\rho(x)A(x)dx}{\omega_i^2-\varphi^2+j2\xi_i\omega_i\varphi} e^{j\varphi t}. \tag{6-6}$$

As a result, normal mode eigenfunctions in Eq. (6-3) and modal participation coefficients in Eq. (6-6) are used to derive the dynamic steady state response of the non-uniform structure relative to its base as,

$$w(x,t) = \sum_{i=1}^{\infty} X_i(x)T_i(t) = \sum_{i=1}^{\infty} X_i(x) \frac{\varphi^2 Y \int_0^L X_i(x)\rho(x)A(x)dx}{\omega_i^2-\varphi^2+j2\xi_i\omega_i\varphi} e^{j\varphi t}. \tag{6-7}$$

This was the transverse vibration response resulted from the base excitation. Next, the procedure of deriving the electromechanical outputs of a non-uniform piezoelectric energy harvester is considered. The Erturk and Inman [87] approach in open circuit condition is followed.

The piezoelectric layer is subjected to an external stress field and generates electrical charge in response [46]. Hence, the sensor relation is rewritten as,

$$D_3(x,t) = d_{31}\sigma_1(x,t) + e_{33}^{\sigma}E_3(t), \tag{6-8}$$

where D_3 is the electrical displacement, d_{31} is the piezoelectric coefficient with polarization in direction 3 due to the external stress in direction 1, σ_1 is the axial stress along 1-axis, $e_{33}{}^{\sigma}$ is the permittivity at constant stress, and E_3 is the electrical field along 3-axis. It should be noted that 1, 2, and 3 directions are aligned with x, y and z axes, respectively [121].

By replacing the axial stress σ_1 with bending strain ε_1, changing the component permittivity at constant stress into constant strain by using the relation $e_{33}^{\varepsilon} = e_{33}^{\sigma} - d_{31}^2 E_p$ [44], and knowing that due to assumed uniform electric field $E_3(t) = \frac{V(t)}{h_p}$, Eq. (6-8) is revised as,

$$D_3(x,t) = d_{31}E_p\varepsilon_1(x,t) - e_{33}^{\varepsilon}\frac{V(t)}{h_p}, \tag{6-9}$$

where E_p is the piezoelectric elasticity modulus and $V(t)$ is the electric voltage over the piezoelectric area [121].

The longitudinal bending strain $\varepsilon_1(x,t)$ in the structure can be calculated as,

$$\varepsilon_1(x,t) = -h_c\frac{\partial^2 w(x,t)}{\partial x^2} = -\left(h(x) + \frac{h_p}{2}\right)\frac{\partial^2 w(x,t)}{\partial x^2}, \tag{6-10}$$

where h_c is the distance between the center of the piezoelectric layer and the beam neutral axis and $\frac{\partial^2 w(x,t)}{\partial x^2}$ is the curvature of the structure [121].

Consequently, the electric displacement function becomes,

$$D_3(x,t) = -\left(h(x) + \frac{h_p}{2}\right) d_{31} E_p \frac{\partial^2 w(x,t)}{\partial x^2} - e_{33}^{\varepsilon} \frac{V(t)}{h_p}. \quad (6\text{-}11)$$

The electric displacement $D_3(x,t)$ is related to the generated electric charge $q(t)$ by integration over the electrode area defined as,

$$q(t) = \iint [0 \quad 0 \quad D_3] \begin{bmatrix} dA_1 \\ dA_2 \\ dA_3 \end{bmatrix} = -\int_{x=0}^{L} \left[d_{31} E_p \left(h(x) + \frac{h_p}{2}\right) \frac{\partial^2 w(x,t)}{\partial x^2} + e_{33}^{\varepsilon} \frac{V(t)}{h_p} \right] b(x) dx, \quad (6\text{-}12)$$

where dA_1, dA_2, and dA_3 are components of the electrode area in the 2-3, 1-3, and 1-2 planes, respectively and $b(x)$ is the width variation function [121].

According to Eq. (6-12), the generated charge is only dependent on the normal component of the electrode area to the electric displacement. Additionally, it is assumed that the electrode area is covering the entire surface of the beam. Since the vibration mode of the energy harvester is not restricted to the first mode, segmented piezoelectric patches and electrodes are utilized to avoid the charge offset happening at higher vibration modes of the beam [46]. This is due to the fact that using continuous electrodes results in phase difference in the strain distribution and leads to the charge cancellation [87]. Therefore, Eq. (6-12) is rephrased in the segmented format as,

$$q(t) = -\sum_{u=1}^{N_p} \left\{ \int_{(u-1)L_p}^{uL_p} \left[d_{31} E_p \left(h(x) + \frac{h_p}{2}\right) \frac{\partial^2 w(x,t)}{\partial x^2} + e_{33}^{\varepsilon} \frac{V(t)}{h_p} \right] b(x)\, \mathrm{d}x \right\}, \quad (6\text{-}13)$$

where N_p is the total number of piezoelectric patches bonded to the surface of the host beam and obviously $N_p l_p = L$ [121].

Considering each piezoelectric patch as an individual harvester, absolute charge values from each piezoelectric patch are added together to build the total charge generated by the harvester [121].

The objective of this research is to estimate the open circuit voltage across the piezoelectric layers. Hence, the backward coupling in the relations is ignored [121]. Moreover, the term $\int_{x=0}^{L} \frac{e_{33}^{\varepsilon}}{h_p} b(x) \mathrm{d}x$ is defined as the capacitance of the piezoelectric layer and is represented by C_p [126]. Finally, the generated voltage $V(t)$ can be derived as,

$$V(t) = -\frac{d_{31}E_p}{C_p} \sum_{u=1}^{N_p} \left[\int_{(u-1)L_p}^{uL_p} b(x) \left(h(x) + \frac{h_p}{2} \right) \frac{\partial^2 w(x,t)}{\partial x^2} \mathrm{d}x \right]. \tag{6-14}$$

In order to provide a more general form of steady state response, frequency response functions (FRFs) of the electromechanical outputs are obtained and presented. Firstly, the voltage FRF is defined as the ratio of the steady state voltage output to the base displacement [121]. Hence, voltage FRF is described as,

$$\frac{V(t)}{-Ye^{j\varphi t}} = \frac{\varphi^2 d_{31} E_p}{C_p} \sum_{i=1}^{\infty} \left\{ \sum_{u=1}^{N_p} \left[\int_{(u-1)L_p}^{uL_p} b(x) \left(h(x) + \frac{h_p}{2} \right) \frac{\mathrm{d}^2 X_i(x)}{\mathrm{d}x^2} \mathrm{d}x \right] \frac{\int_0^L X_i(x) \rho(x) A(x) \mathrm{d}x}{\omega_i{}^2 - \varphi^2 + j2\xi_i \omega_i \varphi} \right\}. \tag{6-15}$$

Eq. (6-15) is the modified version of an equation analytically derived and experimentally validated by Erturk and Inman [96]. They have proved that the FRFs from the analytical solution can precisely predict the voltage output of a uniform bimorph [121].

Secondly, the relative tip motion FRF is presented as the ratio of the beam tip movement to the base displacement. It is noted that the presented model is not limited to the motion at the tip and can be applied to any point along the beam [121]. The tip motion FRF is defined as,

$$\frac{w(L,t)}{-Ye^{j\varphi t}} = \varphi^2 \sum_{i=1}^{\infty} X_i(L) \frac{\int_0^L X_i(x)\rho(x)A(x)\mathrm{d}x}{\omega_i{}^2 - \varphi^2 + j2\xi_i\omega_i\varphi}. \tag{6-16}$$

6.1.2 Simulations and Discussion

Based on the developed model, the electromechanical outputs of a nonlinearly tapered and FGM energy harvester are analytically obtained. Now, numerical examples are presented to demonstrate the validity and efficiency of the proposed model. Various non-uniform configurations are investigated in order to examine the effect of different design parameters and subsequently harvest the maximum electrical energy from the ambient mechanical vibration [46].

A uniform beam with piezoelectric sensors bonded on its surface is considered with geometric dimensions, material properties, and electromechanical coefficients listed in Table 6-1. The excitation of the piezoelectric energy harvester is due to the harmonic base translation and the steady state dynamic response of the system is of interest. Furthermore, structural strain rate damping ratios for the first two vibration modes are assumed to be ξ_1=0.03 and ξ_2=0.039. Finally, two steady state frequency responses, voltage output and beam tip motion, are studied. Based on the convergence study for vibration analysis of non-uniform beams, 20 terms of the mode shape function series (n=20) are used to accurately present the final mode shape function [46].

Table 6-1 Geometry and material properties of a uniform piezoelectric energy harvester [46].

Host beam					PZT4				
L (m)	h_0 (m)	b_0 (m)	E_0 (N/m^2)	ρ_0 (kg/m^3)	h_p (m)	E_p (N/m^2)	ρ (kg/m^3)	d_{31} (m/V)	e_{33} (F/m)
0.3	0.005	0.05	210*10^9	7800	0.0004	66*10^9	7800	-190*10^{-12}	15.93*10^{-9}

First of all, to verify the effectiveness and accuracy of the proposed method, the power output for a uniform cantilever beam subjected to a low frequency harmonic point force was obtained by Xie et al. [127] to be 0.002W. By using the proposed model here, the power output can be evaluated as 0.00195W under the same working condition. This demonstrates the accuracy and validity of the model [46].

Although the geometry or material property variation function in the presented model is not limited to any specific type of function and can be a general definition, three different nonlinear variation functions are considered as the case studies. They are 'exponentially decaying' in which the variation function is defined as $g(x) = g_0 e^{-m\frac{x}{L}}$, 'trigonometrically decaying' in which the variation function is defined as $g(x) = g_0 \cos\left(\frac{m\pi x}{2L}\right)$, and lastly 'exponentially increasing' in which the variation function is defined as $g(x) = g_0 e^{m\frac{x}{L}}$ where g_0 is the initial value, m is the tapering ratio, and $0 \leq x \leq L$ [46].

All taper/variation functions are defined from fixed to free end of the cantilever beam. To further clarify, Fig. 6-1(a) illustrates the three nonlinear geometry and material property variation functions and Fig. 6-1(b) shows an exponentially decaying tapered cantilever beam with piezoelectric patches mounted on its surface with possible FGM properties. For the effective electromechanical outputs comparison, all of the beams with different designs have identical length, volume, and mass [46].

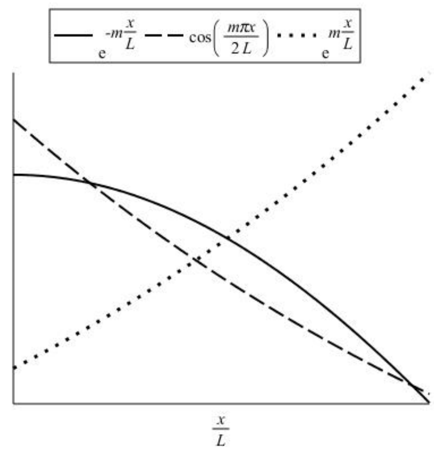

(a)

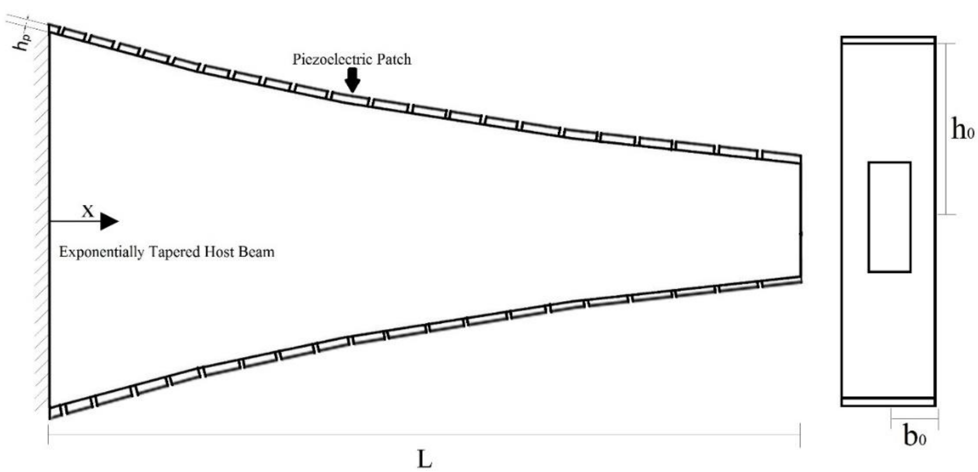

(b)

Fig. 6-1 Non-uniform configurations [46]. (a) Three nonlinear geometry and material property variation functions. (b) An exponentially decaying tapered cantilever beam with piezoelectric patches mounted on its surface, side and front views.

Fig. 6-2(a) displays the nonlinear geometry effect on the voltage output FRF for an exponentially decaying energy harvester like the structure in Fig. 6-1(b). As can be seen, higher nonlinearity in geometry of the harvester results in substantial increase of the voltage amplitude. To further clarify, by increasing the geometry taper ratio from 0 to 0.8, the peak voltage outputs for the first and second vibration modes show 1.71 and 1.32 times higher values, respectively, compared with the traditional uniform design. Furthermore, the decaying nonlinear geometry increases the natural frequencies of the structure. As a result, for excitation frequencies between the first and second natural frequencies of the uniform harvester ($290rad/s \leq \varphi \leq 1830rad/s$), non-uniform piezoelectric energy harvester with the same volume and material properties but with 0.8 geometrical taper ratio can generate up to 15.46 times larger voltage output, Fig. 6-2(a). Additionally, Fig. 6-2(b) illustrates the nonlinear geometry effect on the tip motion displacement. The trapezoidal profile of the harvester has led into larger distribution of strain along the length of the structure. Clearly, the lateral displacement amplitude drastically increases when the excitation frequency is close to the natural frequencies of the harvester. As depicted in the Fig. 6-2, exponentially decaying geometry of the piezoelectric energy harvester has significant positive effect on the output values [46].

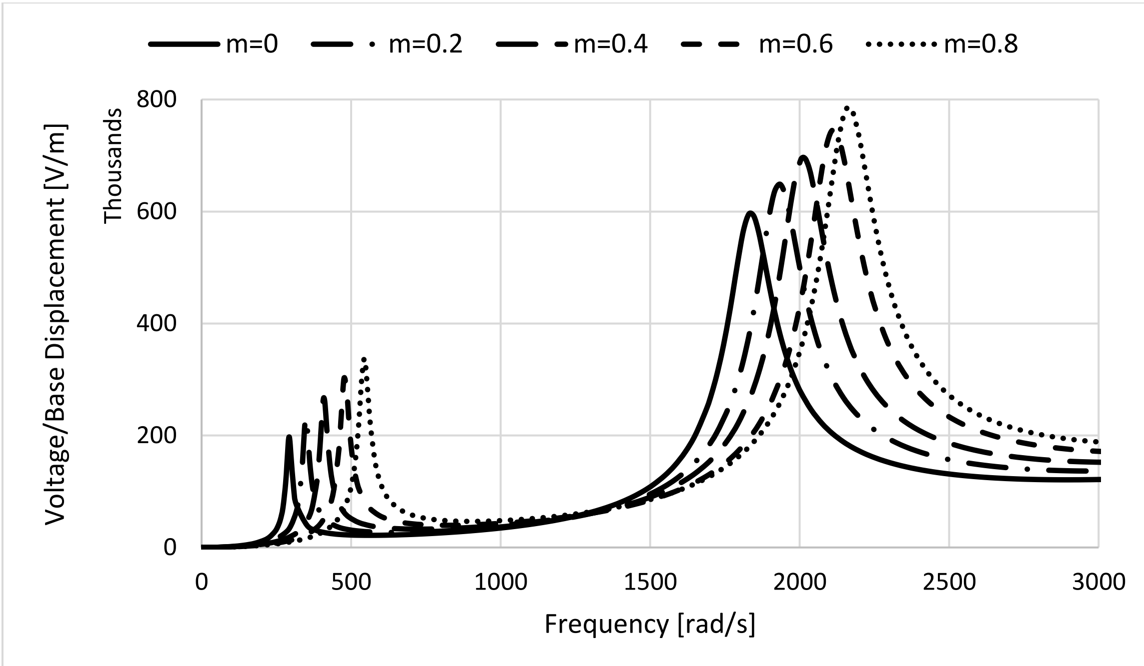

(a)

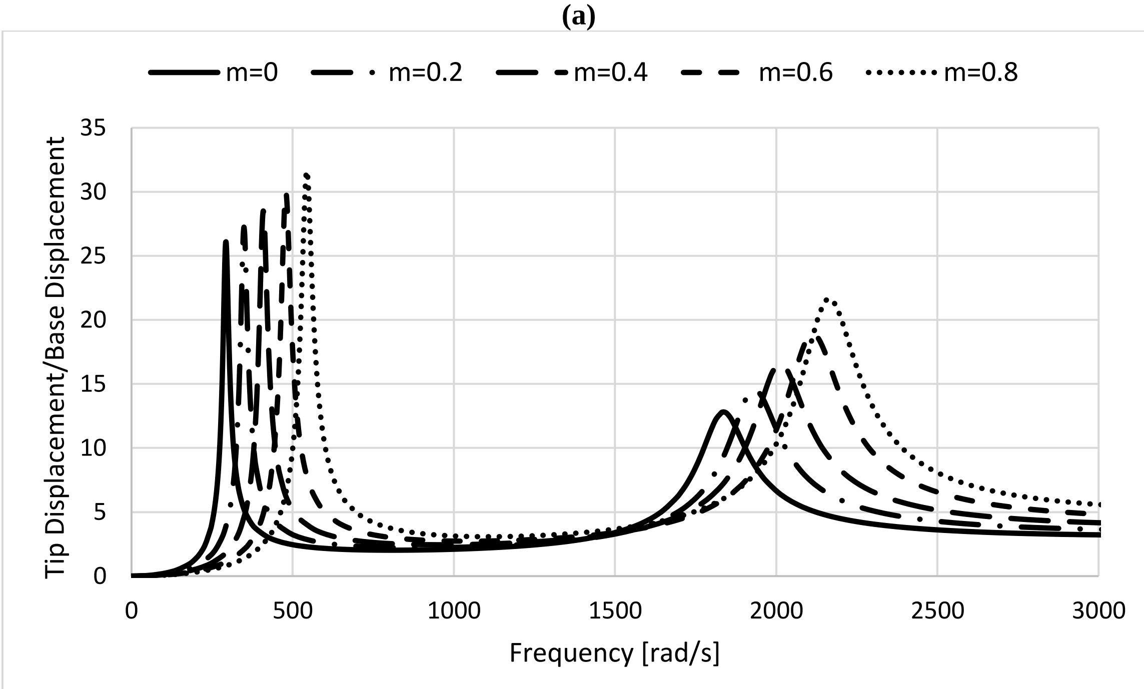

(b)

Fig. 6-2 Voltage output and tip displacement frequency responses for an exponentially decaying tapered piezoelectric energy harvester with different geometrical taper ratios [46]. (a) Voltage output. (b) Tip displacement.

The voltage output and tip motion amplitudes in the frequency domain for a tapered energy harvester with a cosine function variation profile are represented in

Fig. 6-3. By comparing Figs. 6-2 and 6-3, similar trend of results for both decaying geometries can be realized. The voltage output in Fig. 6-3(a) and tip displacement in Fig. 6-3(b) show the constructive effect of non-uniform configuration. Based on Fig. 6-3(a), the peak voltage outputs for the first two vibration modes can be enhanced 1.90 and 1.41 times when taper ratio changes from 0 to 0.8. Moreover, for ambient vibration frequencies between the first and second natural frequencies of the uniform harvester (290rad/s≤φ≤1830rad/s), up to 14.70 times larger voltage output can be obtained by using a non-uniform harvester with the same volume and 0.8 geometrical taper ratio. Likewise, increasing the nonlinearity in the geometry of the harvester leads to greater natural frequencies and tip motion amplitude [46].

Fig 6-4 illustrates the electrical and mechanical FRFs for an exponentially increasing piezoelectric energy harvester. Although the voltage and tip motion amplitudes at resonant condition significantly decrease for the non-uninform configuration compared with the uniform one, increasing the taper ratio reduces the natural frequencies of the structure. For energy harvesting from environmental vibration signals with very low frequencies like HVAC systems, this property can be useful. For instance, the voltage output for the exponentially increasing tapered harvester with taper ratio of 0.4 is up to 13.45 times higher than the uniform one with the same volume and material properties for the excitation frequency of φ=194rad/s, Fig. 4(a). Furthermore, the relative tip displacement for various geometrical taper ratios is shown in Fig. 6-4(b). Higher geometrical nonlinearity leads to smaller natural frequencies and tip displacement amplitude [46].

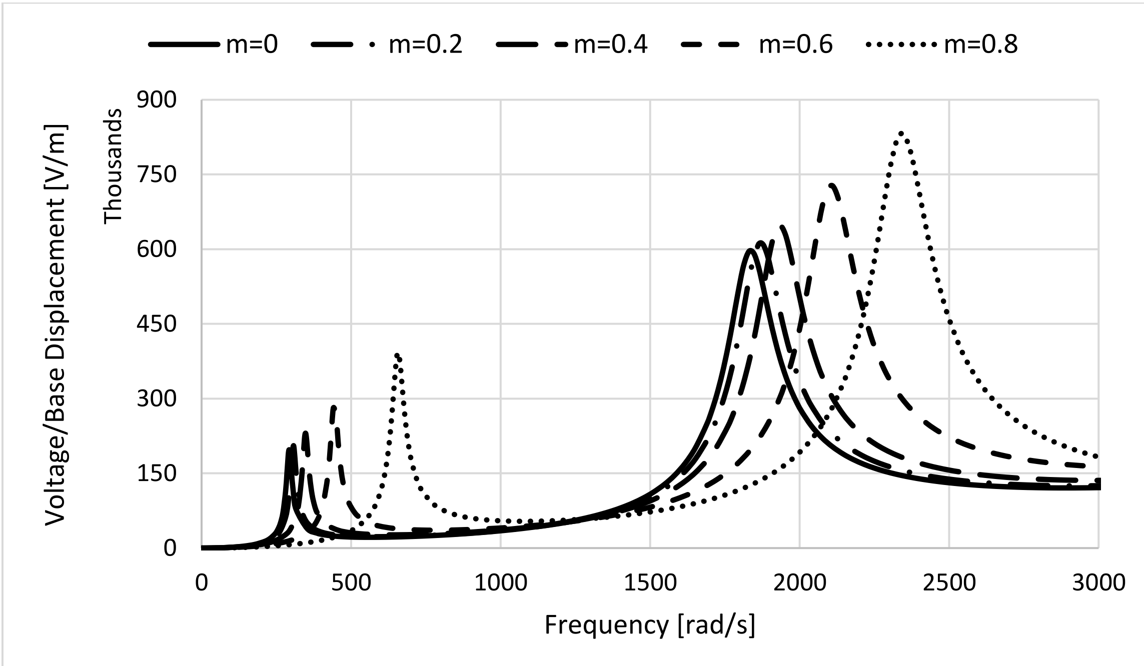

(a)

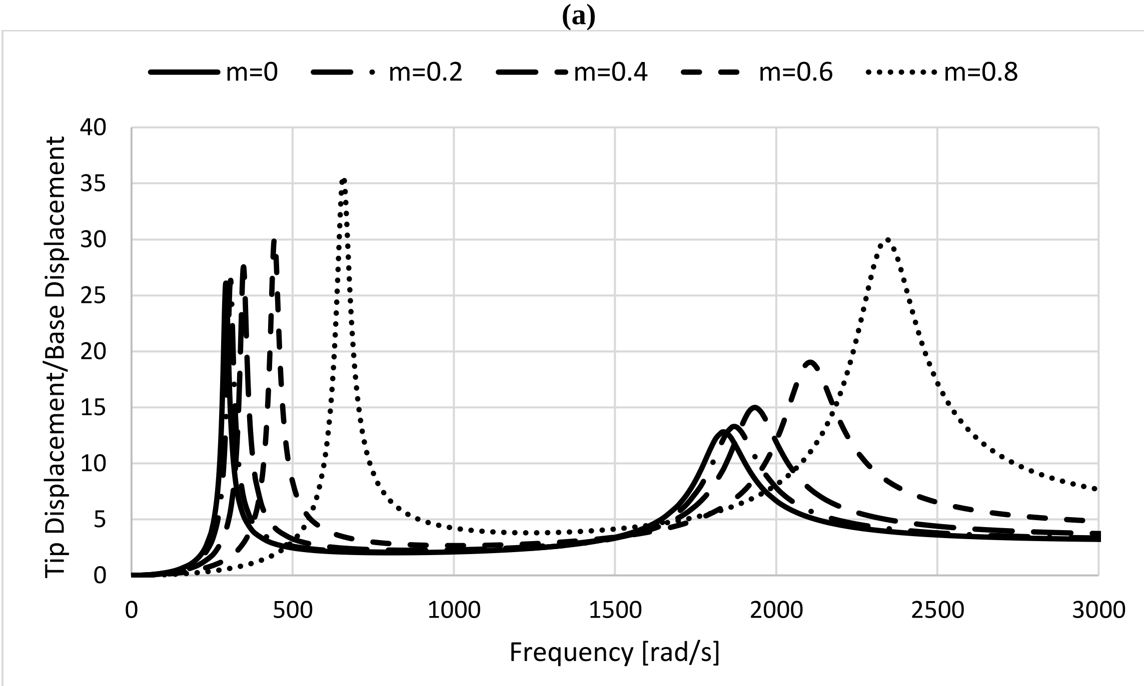

(b)

Fig. 6-3 Voltage output and tip displacement frequency responses for a trigonometrically decaying tapered piezoelectric energy harvester with different geometrical taper ratios [46]. (a) Voltage output. (b) Tip displacement.

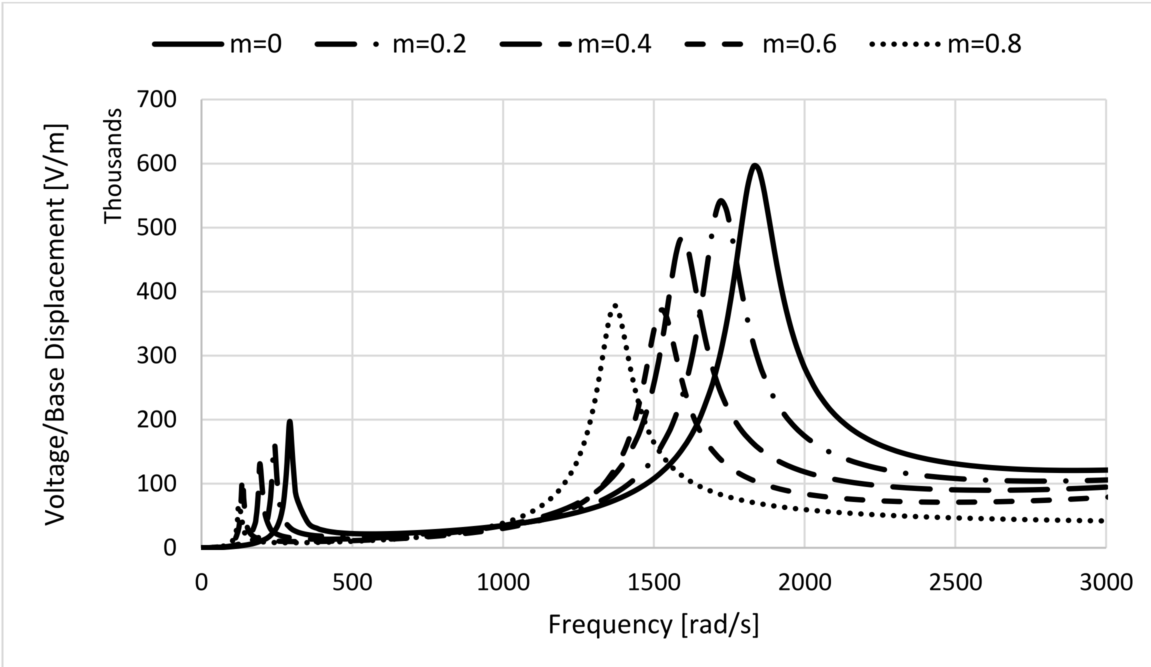

(a)

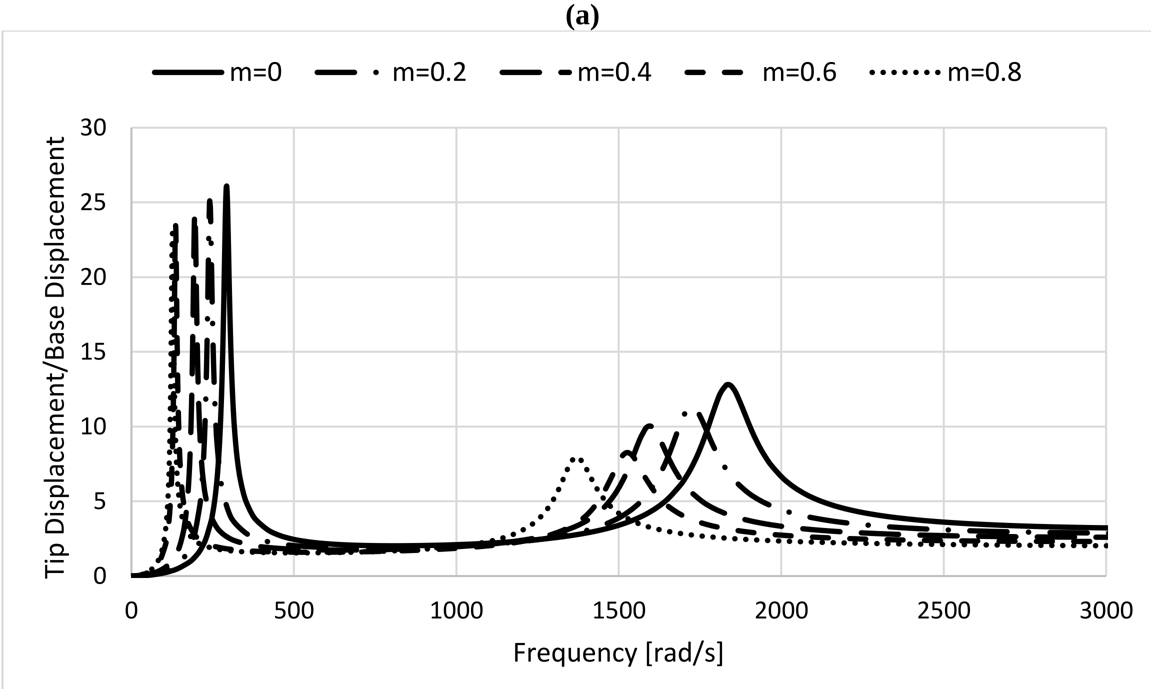

(b)

Fig. 6-4 Voltage output and tip displacement frequency responses for an exponentially increasing tapered piezoelectric energy harvester with different geometrical taper ratios [46]. (a) Voltage output. (b) Tip displacement.

In order to study the effect of axially FGM properties on the electromechanical outputs with different excitation frequencies, the exponential FGM variation profile is employed. Thus, the decaying and increasing exponential functions are representing the material property variation along the length of the beam. It should be noted that for the effective comparison of the results, all of the beams with different designs have the same volume and length. Therefore, a uniform cantilever energy harvester with axially variable FGM properties $E(x) = E_0 e^{-a\frac{x}{L}}$ and $\rho(x) = \rho_0 e^{-b\frac{x}{L}}$ is considered where a and b are elasticity and density taper ratios. The values of a and b will be positive for the decaying FGM profile from fixed to free end of the beam, while they are negative for the increasing FGM profile. Additionally, E_0 and ρ_0 are elastic modulus and density of the homogenous beam, respectively. For the non-uniform structure, E_0 and ρ_0 values are defined at the fixed end for the decaying FGM profile and at the free end for the increasing FGM profile. In this case, elastic modulus and density of the non-uniform harvesters with the FGM design are smaller than the homogenous harvester resulting in lighter and more flexible structures but with the same volume and length [46].

Fig. 6-5 graphically indicates the relationship between axially FGM and voltage output in the frequency domain for various taper ratios. Fig. 6-5(a) shows the functionally graded elasticity effect and Fig. 6-5(b) illustrates the functionally graded density impact on the voltage output of the harvester. According to Fig. 6-

5(a), axially decaying elasticity profile (positive taper ratios) decreases the natural frequencies of the structure by reducing its elasticity which can be beneficial in harvesting power from low level vibration frequencies. Additionally, considerable increase in the peak voltage output corresponding to the resonance can be seen. As an illustration, at excitation frequencies close to 270rad/s and 1570rad/s, the harvester with elasticity taper ratio a=+0.75 can generate 2.94 and 4.33 times higher voltage compared to the homogeneous structure, Fig. 6-5(a). In addition, although the increasing variation profile (negative taper ratios) does not lead to higher peak voltage output, it still can be a superior design at some lower excitation frequencies. For example, an energy harvester with elasticity taper ratio a=-0.75 can produce up to 11.09 times higher voltage compared to the homogeneous one at excitation frequency of 210rad/s, which is lower than the first resonant frequency of the homogeneous beam, Fig. 6-5(a). On the other hand, density variation effect on voltage output is depicted in Fig. 6-5(b). It should be noted that harvesters with the defined axially variable density here are much lighter than the homogeneous one. As can be seen in Fig. 6-5(b), nonlinear density profile results in higher natural frequencies of the harvester. Better voltage outputs can be seen at excitation frequencies higher than resonance frequencies of the homogeneous harvester for the decaying density profile. For instance, a harvester with exponential density variation profile at b=+0.75 taper ratio can generate up to

7.48 times larger voltage output compared to a homogeneous harvester at excitation frequencies around 395rad/s despite the fact that it is 30% lighter [46].

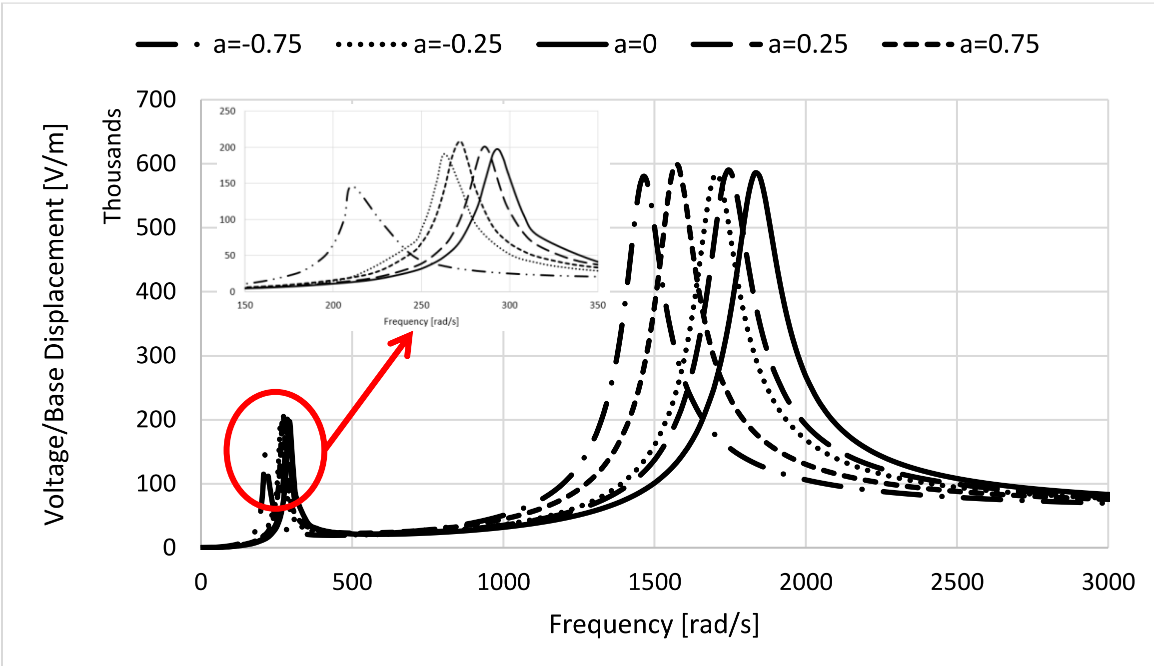

(a)

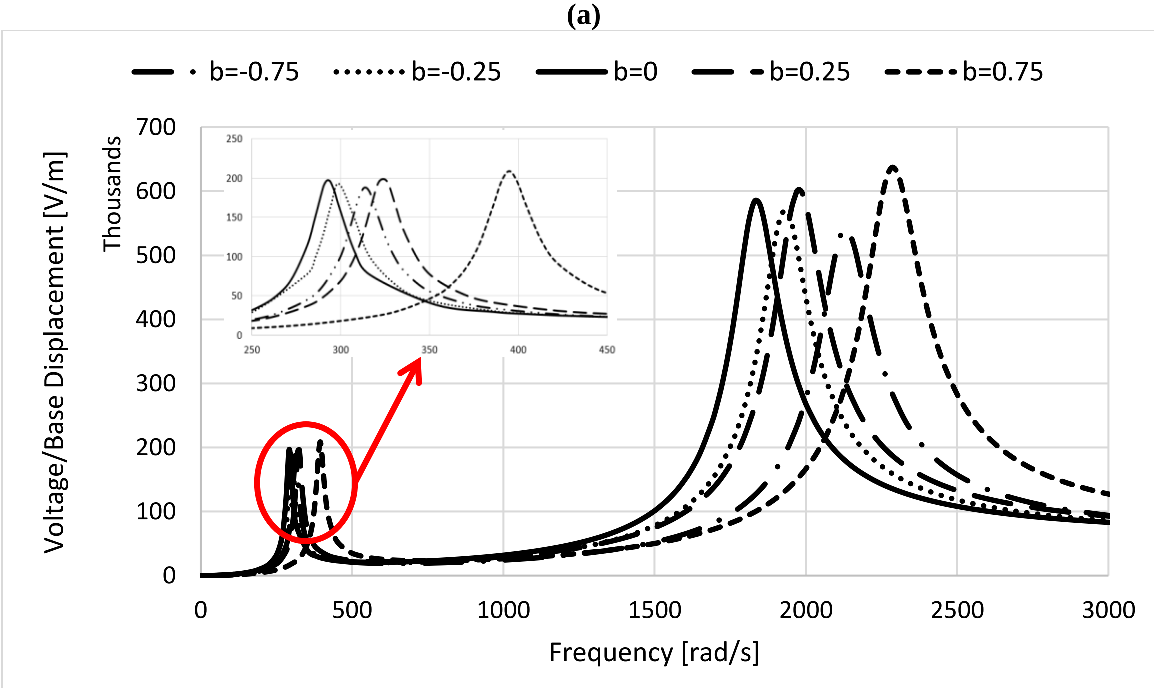

(b)

Fig. 6-5 Voltage output frequency response for uniform piezoelectric energy harvester with various exponential FGM properties (with the enlarged view of the first mode resonance) [46]. (a) Axially variable elasticity (constant density). (b) Axially variable density (constant elasticity).

Fig. 6-6 displays the voltage output and tip motion FRFs for a uniform harvester with axially exponential functionally graded elasticity and density profiles, simultaneously. Graphs are drawn just for higher taper ratios to effectively compare the results for various combinations of decaying and increasing profiles. Based on Fig. 6-6(a), for very low ambient vibration frequencies much smaller than the first resonance of the uniform harvester ($\varphi<254$rad/s), a nonhomogeneous piezoelectric energy harvester with the same volume, smaller mass, and increasing FGM profile ($a=b=-0.75$) can generate higher voltage up to 9.44 times larger than the homogeneous one. On the other hand, for excitation frequencies higher than the first resonance of the homogeneous harvester ($\varphi\geq295$rad/s), the nonhomogeneous configuration with the same volume, smaller mass, and decaying FGM profile ($a=b=0.75$) can produce up to 7.10 times larger voltage output compared to the homogeneous one. In Fig. 6-6(b) the relative tip displacement against excitation frequency is presented which shows an analogous variation around the resonance frequencies [46].

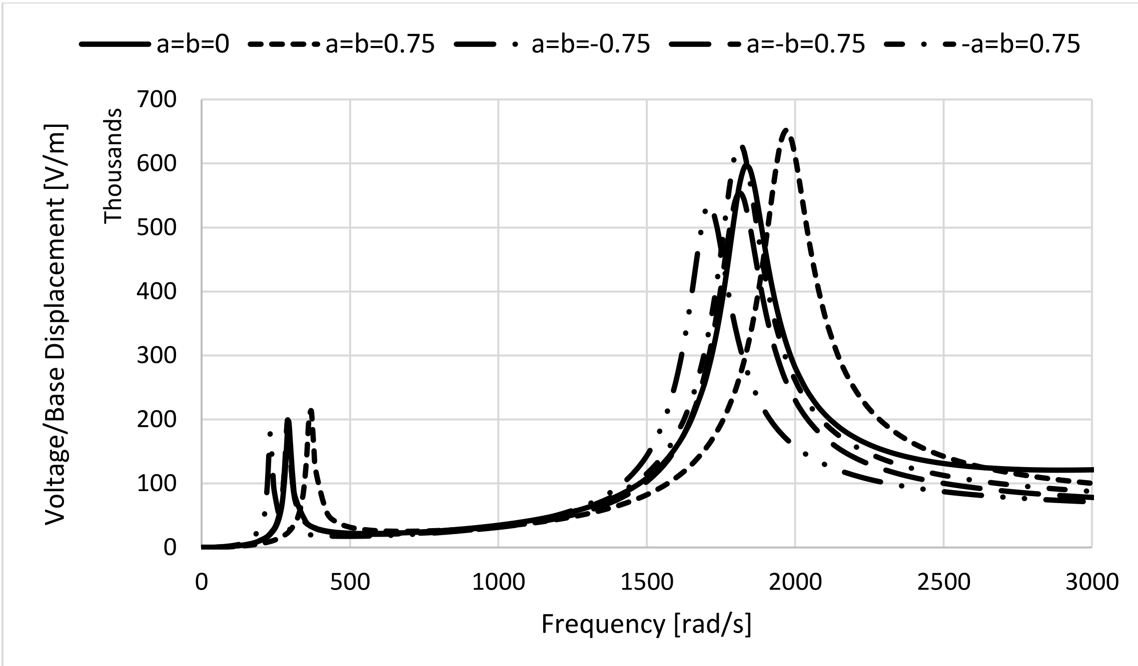

(a)

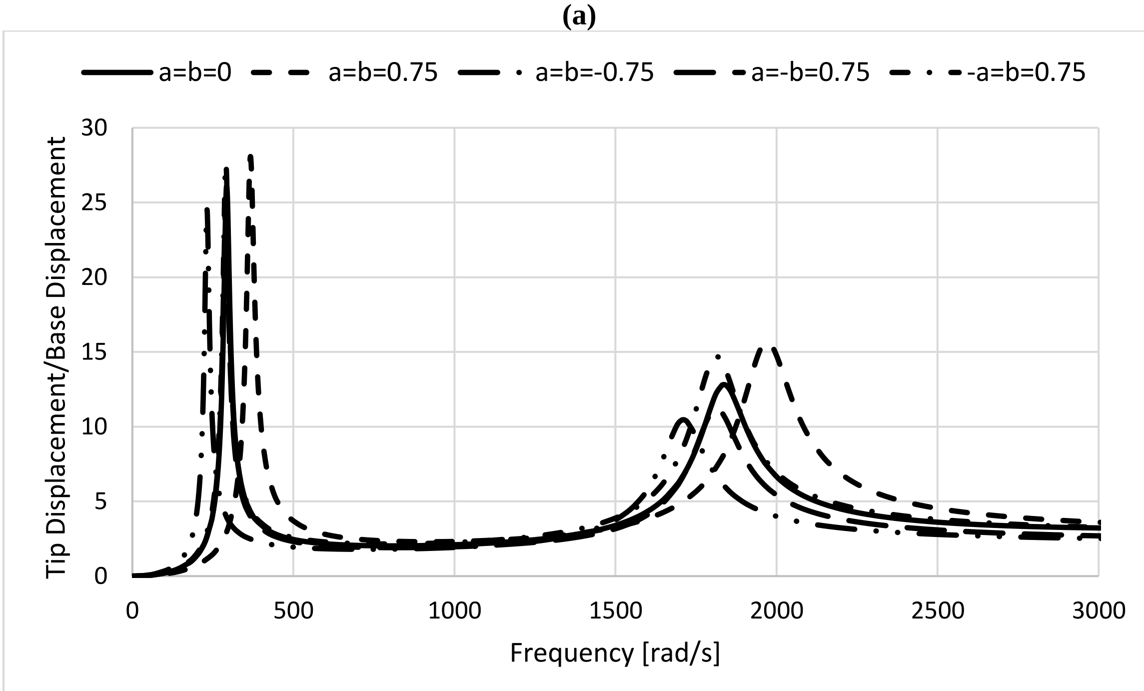

(b)

Fig. 6-6 Voltage output and tip displacement frequency responses for uniform piezoelectric energy harvester with various exponential FGM properties [46]. (a) Voltage output. (b) Tip displacement.

It has been demonstrated that the best structural design for a bimorph cantilever energy harvester to optimally harvest the environment vibration energy depends on several parameters including size, material, geometry and material properties variation profiles, the nonlinearity tapering rates, and the excitation frequency [46].

Fig. 6-7 depicts a comparison between electromechanical outputs of three bimorph piezoelectric energy harvesters. The first non-uniform harvester has exponentially decaying geometry (m=0.8) and FGM profile (a=b=0.75) and the other one has exponentially decaying geometry (m=0.8) with axially decaying elasticity but increasing density profile (-a=b=0.75). Compared to the traditional uniform harvester, the peak voltages for the first and second vibration modes of the non-uniform tapered FGM design can be enhanced up to 2.27 and 1.38 times, respectively. Furthermore, for excitation frequencies higher than the first natural frequency of the uniform harvester ($\varphi \geq 295$rad/s), the proposed non-uniform harvesters with tapered geometry and FGM design can generate up to 19.76 times larger voltage output compared to the uniform one, Fig. 6-7(a). The superior electromechanical features of the non-uniform energy harvesters are shown in Figs. 6-7(a) and 6-7(b) [46].

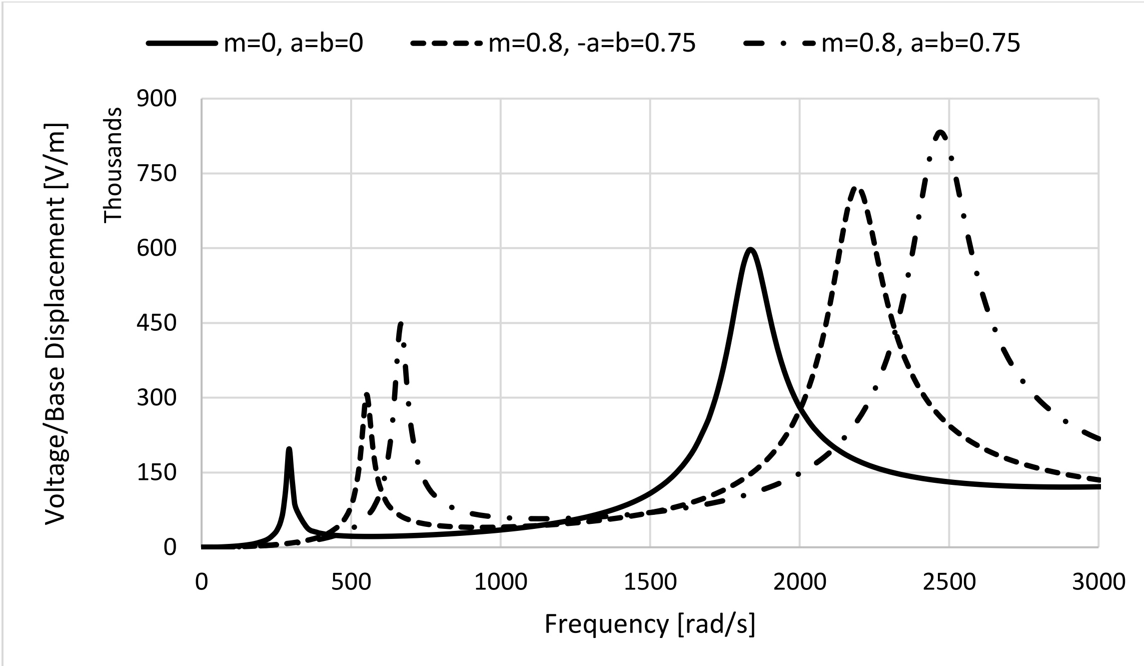

(a)

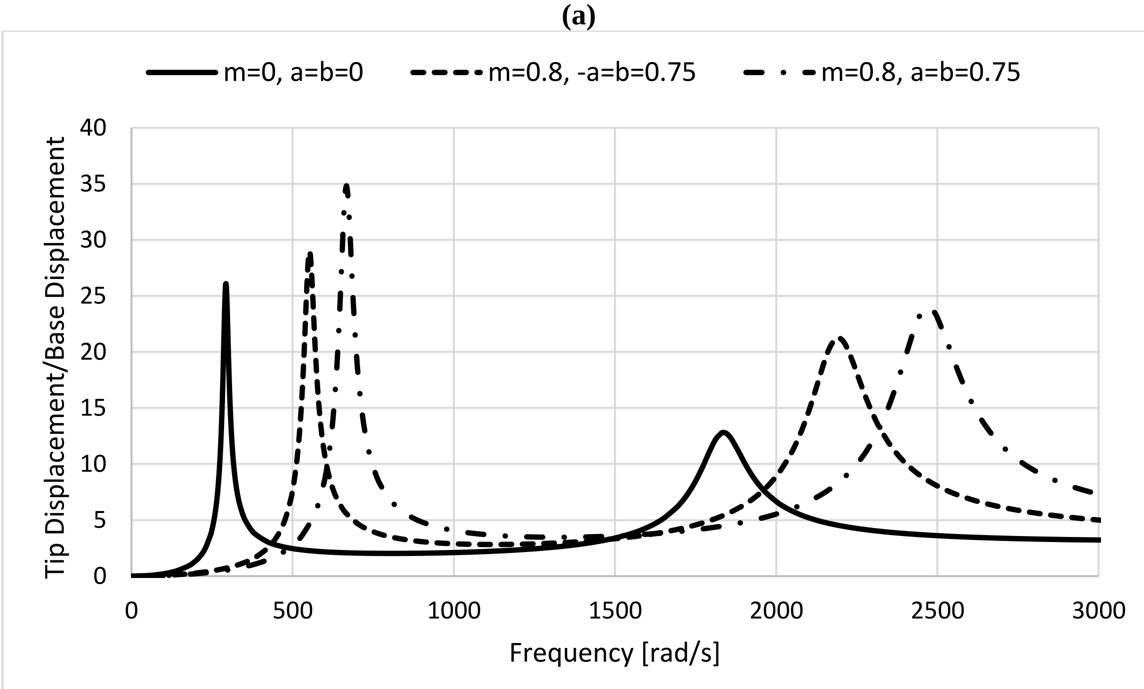

(b)

Fig. 6-7 Voltage output and tip displacement frequency responses for three piezoelectric harvester designs with the same volume and length, uniform with homogeneous material and exponentially tapered with exponential FGM property [46]. (a) Voltage output. (b) Tip displacement.

6.1.3 Conclusion

In this section, a new non-uniform piezoelectric energy harvester design was presented to enhance the energy harvesting efficiency and voltage output compared with the traditional uniform bimorph harvesters. The electromechanical solution of a nonlinearly tapered and axially FGM cantilever piezoelectric energy harvester subjected to harmonic base motion was analytically presented. The steady state vibration response of the smart structure was obtained and closed-form expressions for the voltage output in open circuit condition and tip displacement of the harvester were derived. Based on the parametric study, effects of nonlinear geometry and FGM variation functions as well as the excitation frequency on the voltage output and beam tip displacement were investigated and presented [46].

In summary, the presented model is applicable to any non-uniform energy harvester with general nonlinear geometry and axially FGM properties. For numerical study, three different nonlinear functions were selected. Following results were concluded [46]:

1. The decaying geometry increases the natural frequencies and electromechanical outputs. Compared to the traditional uniform design, up to 15.46 times higher voltage output can be harvested in relatively high frequency domains. In addition, the decaying FGM profile demonstrated up to 7.10 times better electromechanical outputs compared to the uniform one.

2. The geometry or FGM increasing profiles can generate up to 13.45 times larger voltage output at relatively low excitation frequencies compared to the uniform configuration with the same length and volume.

3. Based on the environment peak power frequency range, the non-uniform beam can be efficiently designed to harvest the maximum possible amount of energy. For low ambient vibration frequencies, increasing geometrical and FGM profile obtains more energy. In contrast, for higher excitation frequencies larger than the resonance frequency of the uniform structure, the harvester with decaying geometry and FGM profile generates more power.

4. The piezoelectric energy harvester combining the decaying nonlinearly tapered geometry and FGM design can generate more than 19.76 times higher voltage output compared to the one with traditional uniform homogeneous design in relatively high frequency domains.

6.2 Wideband Energy Harvesting System

This section investigates development of a wideband piezoelectric energy harvesting system with efficient electromechanical outputs. This work endeavors to challenge earlier energy harvesting designs and engineer a novel and advanced energy harvesting system with adequate bandwidth in the range of ambient vibration frequencies by considering nonlinear geometry design. The wideband harvester is proposed by combining several non-uniform piezoelectric coupled cantilevers with identical volume and length but different taper ratios. The theoretical model is based on what was presented in section 6.1 of this thesis. Furthermore, model is numerically tested with two sample structures made of 20 and 10 non-uniform piezoelectric coupled cantilevers with different geometries. However, it can be generalized to various numbers of beams and different conversion principles. It is demonstrated that with the suggested non-uniform design, the broadband energy harvesting design can function effectively with high voltage output over a wide frequency range. Therefore, optimum structural design for the required operational frequency range can be achieved [121].

This section of the thesis is reproduced with some modifications from [A. Keshmiri, N. Wu “A wideband piezoelectric energy harvester design by using multiple non-uniform bimorphs”, Vibration, 1(1), 93-104, 2018] with permission from the “MDPI”.

6.2.1 Theoretical Model

The proposed bimorph piezoelectric energy harvester includes beams with nonlinear geometry profile, homogeneous material properties, and surface bonded piezoelectric patches, Fig. 6.1(b). First, a uniform beam with piezoelectric sensors bonded to its surface is considered with the geometrical dimensions, material properties, and electromechanical coefficients listed in Table 6-2. The piezoelectric energy harvester is excited by a harmonic base translation and the steady state dynamic response of the system is of interest. Moreover, structural strain rate damping ratios for the first two vibration modes are assumed to be $\xi_1=\xi_2=0.01$ [121]. It is noted that here no FGM properties is considered. Following the same analytical process from Eq. (6-1) to Eq. (6-16), voltage output and tip displacement FRFs are derived as,

$$\frac{V(t)}{-Ye^{j\varphi t}}=\frac{\varphi^2\rho d_{31}E_p}{C_p}\sum_{i=1}^{\infty}\left\{\sum_{u=1}^{N_p}\left[\int_{(u-1)L_p}^{uL_p} b(x)\left(h(x)+\frac{h_p}{2}\right)\frac{\mathrm{d}^2X_i(x)}{\mathrm{d}x^2}\mathrm{d}x\right]\frac{\int_0^L X_i(x)A(x)\mathrm{d}x}{\omega_i{}^2-\varphi^2+j2\xi_i\omega_i\varphi}\right\}, \qquad (6\text{-}17)$$

$$\frac{w(L,t)}{-Ye^{j\varphi t}}=\rho\varphi^2\sum_{i=1}^{\infty}X_i(L)\frac{\int_0^L X_i(x)A(x)\mathrm{d}x}{\omega_i{}^2-\varphi^2+j2\xi_i\omega_i\varphi}. \qquad (6\text{-}18)$$

Here, the probability of designing a wideband energy harvesting system from an array of non-uniform cantilever bimorphs is investigated [121]. The basic idea of an ensemble of the beam mass structure is borrowed from [128] and has been further developed.

An energy harvesting system including several nonlinearly tapered piezoelectric coupled cantilever beams, each of which has the same volume and length but different taper ratios and hence different resonance frequencies, is considered. A schematic illustration of the proposed wideband energy harvester configuration is shown in Fig. 6-8 [121].

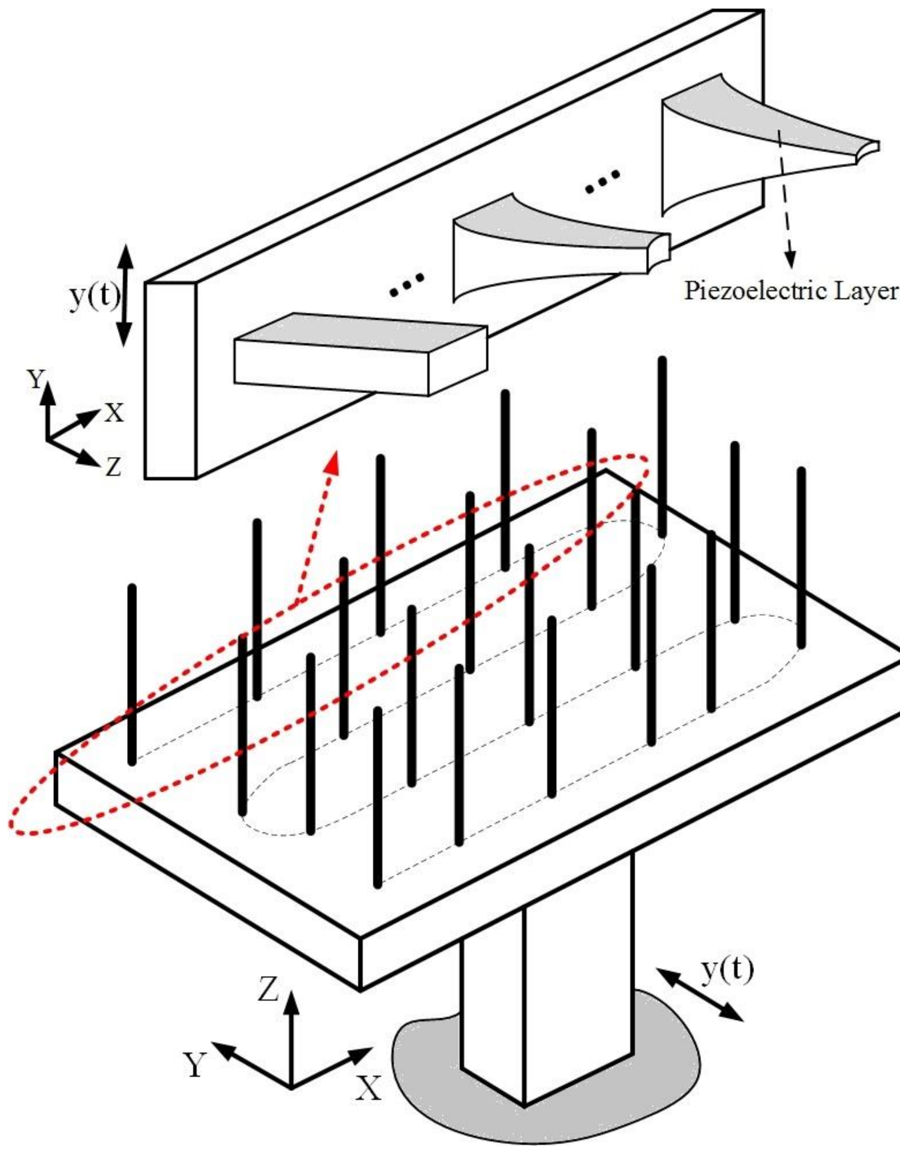

Fig. 6-8 A schematic illustration of a wideband piezoelectric energy harvesting system. An array of nonlinearly tapered cantilever piezoelectric coupled beams mounted on a transversely vibrating base [121].

As shown in section 6.1, the electromechanical outputs have a local maximum at the resonance frequencies of the harvester. It was proved that a tapered structure has different natural frequencies and possibly higher peak voltage output compared to the traditional uniform design with the same length and volume. The nonlinear profile makes the natural frequencies of a harvester with the same size and weight tunable by adjusting the geometrical taper ratios. In addition, for a certain desired voltage output, the non-uniform design can help to reduce the weight of the harvester. Here, the geometrical variation function is the exponential one defined as $g(x)=g_0e^{-mx/L}$ where g_0 is the initial value, m is the taper ratio, and $0\leq x\leq L$ [121].

By combining single bimorph piezoelectric cantilevers with different taper ratios on a vibrating base as shown in Fig. 6-8, wide resonance frequency range can be obtained. Additionally, it is very critical to place bimorph natural frequencies sufficiently close to have a steady and continuous bandwidth for the wideband operation. The assembled system has a wide-ranging operational frequency, which can automatically choose one harvester to resonate at one particular ambient vibration frequency. As a result, the whole system can work as a wideband piezoelectric energy harvester [121].

Table 6.2 Geometry and material properties of the piezoelectric energy harvester [121].

L (m)	b_0 (m)	h_0 (m)	h_p (m)	E (GPa)	ρ (kg/m^3)	E_p (GPa)	ρ_p (kg/m^3)	d_{31} (pm/V)	e_{33}^{ε} (nF/m)
0.2	0.02	0.005	0.004	100	7165	66	7800	-190	15.93

6.2.2 Wideband Harvester with Decaying Profile

In this design, the geometrical variation function is the decaying exponential which means positive values for taper ratios. The geometrical taper ratio changes from 0 to 1 with the increment of 0.05. The voltage output of a wideband energy harvesting system including 20 non-uniform bimorph cantilevers with the same length and volume are presented in Fig. 6-9. As depicted, a slight difference in the geometry of the non-uniform harvester can lead to a considerable alteration in the natural frequencies and electromechanical outputs. In fact, steeper nonlinearity in the geometry of the structure results in higher natural frequencies and peak voltage outputs. Fig. 6-9 shows the estimated voltage output of the wideband energy harvesting system within an input excitation range of [ω_{min}-ω_{max}]=[475-965]rad/s≈[75-155]Hz. The bottom plots show the individual output of each harvester whereas the top plot displays the superimposed overall voltage. As shown in Fig. 6-9, high peak voltage outputs (>10V) at resonance can be obtained in a wide frequency range from 500rad/s to 950rad/s by employing 20 nonlinearly tapered cantilever harvesters. Increasing the excitation frequency leads to higher peak voltage output (10V to 22V) due to the higher natural frequencies of the bimorph cantilevers with greater taper ratios [121].

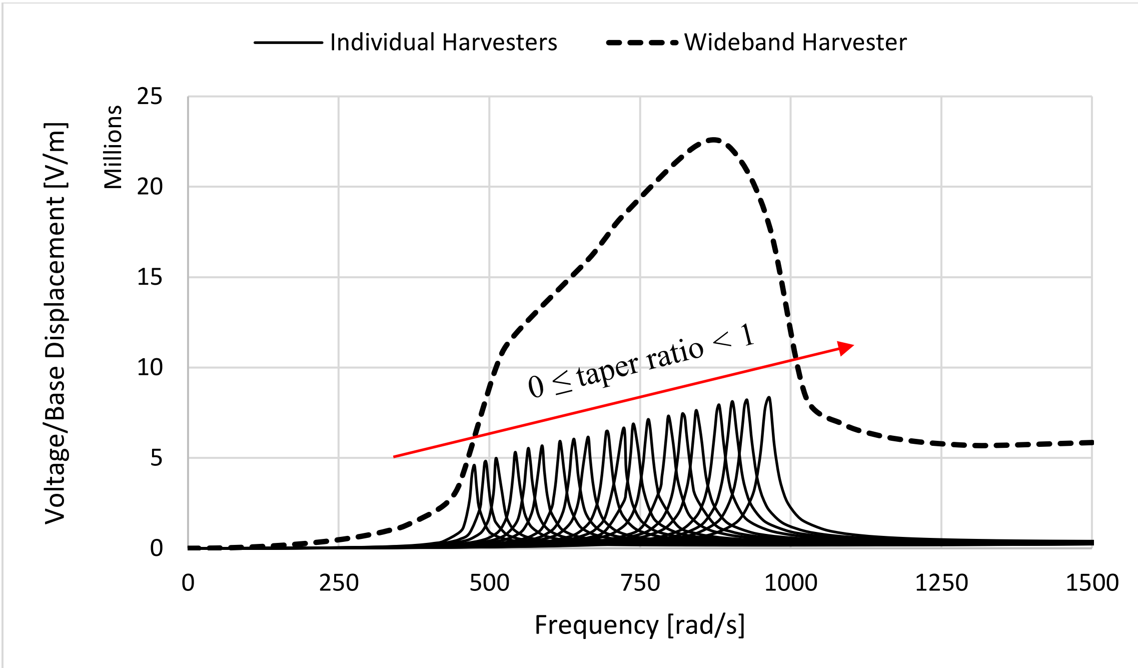

Fig. 6-9 Voltage output frequency response corresponding to the wideband energy harvesting system, 20 harvesters with nonlinear decaying geometry profiles, 0≤taper ratios<1 [121].

It should be noted that all piezoelectric harvesters with decaying tapered geometry have higher natural frequencies than the uniform cantilever with the same length and volume. This limits the application of the wideband harvester under excitations at the low frequency range. Therefore, the growing tapered design leading to lower natural frequencies is discussed in the following section [121].

6.2.3 Wideband Harvester with Growing Profile

For the second proposed design, the geometrical variation function is the growing exponential which means negative taper ratios. Here, geometrical taper ratio changes from -0.5 to 0 with the increment of 0.05. By employing 10 non-uniform bimorph energy harvesters with the same length and volume, the voltage output of a wideband energy harvester is obtained and presented in Fig. 6-10. In contrast to the decaying geometry, the growing profile decreases the natural frequencies of the cantilever structure which is definitely beneficial for energy harvesting from environmental vibration signals with very low frequencies like HVAC systems. The overall voltage output of the wideband energy harvester within an input excitation range of $[\omega_{min}-\omega_{max}]$=[300-475]rad/s≈[45-75]Hz changes from 4.5V to 8V as shown in Fig. 6-10. The bottom plots show the individual output of each harvester whereas the top plot displays the superimposed voltage output [121].

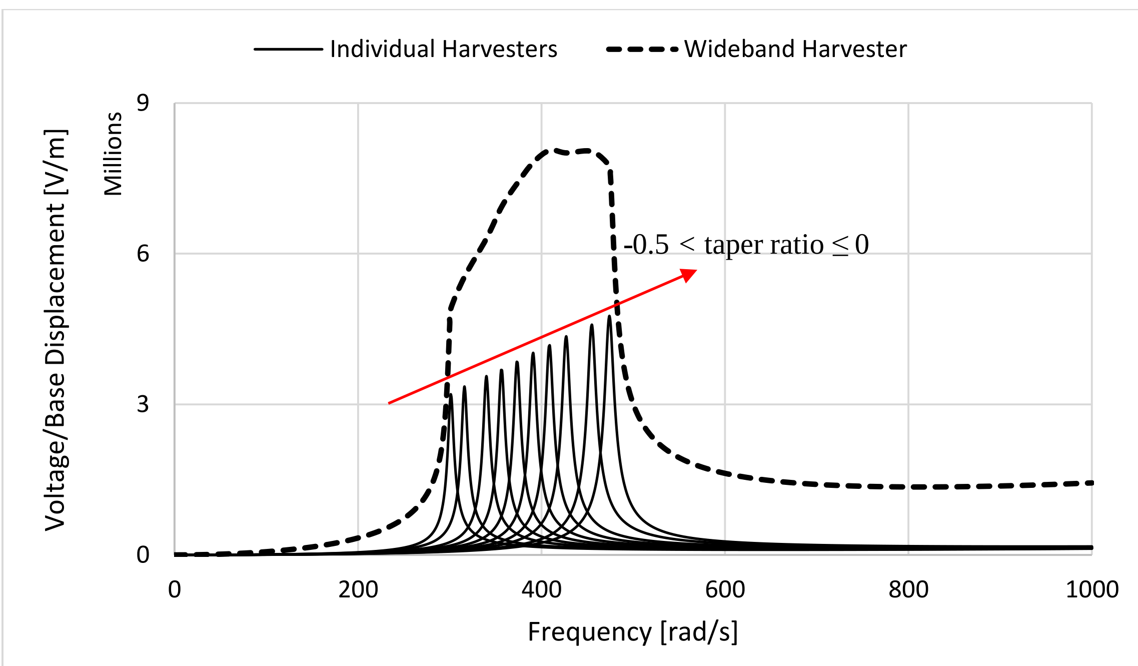

Fig. 6-10 Voltage output frequency response corresponding to the wideband energy harvesting system, 10 harvesters with nonlinear growing geometry profiles, 0≤taper ratios<0.5 [121].

In summary, a wideband harvester comprising two non-uniform configurations can be designed to effectively cover a large bandwidth based on the ambient vibration peak power frequency range covering both low and high frequencies. For the cases in sections 6.2.2 and 6.2.3, a wideband piezoelectric energy harvester consisting 30 nonlinearly tapered beams ($-0.5<m<1$) with similar length and volume/mass can efficiently function over a wide frequency range which roughly covers [45-155]Hz with voltage output changes from 5.5V to 23.4V. In addition to the wideband frequency coverage, it is demonstrated that the peak voltage output for the wideband harvester is roughly 5 times higher than the traditional uniform bimorph design ($m=0$) [121].

6.2.4 Conclusion

In this section, an analytic model for a wideband energy harvesting system combining several nonlinearly tapered cantilevers was presented. By using the developed dynamic model, the steady state response of the smart structure with non-uniform geometry and structural strain rate damping under harmonic motion was obtained and the closed-form expressions for the electrical output FRFs were derived. A wideband piezoelectric energy harvester comprising a group of nonlinearly tapered bimorph cantilevers, each of which has different geometrical taper ratios and hence different resonance frequencies, was studied [121].

A new approach to realize efficient energy harvesting from ambient vibration with variable frequency by widening the bandwidth of the harvester was developed and presented. This is achieved by combining an array of cantilever non-uniform piezoelectric harvesters with different taper ratios and resonance frequencies. The new wideband energy harvesting system can increase the electromechanical outputs compared with the traditional single bimorphs through a combination of multiple nonlinearly tapered beams with the same volume and length. This research challenges previous energy harvesting designs and formulates an innovative wideband energy harvesting configuration, which functions efficiently in a wide range of ambient excitation frequencies [121].

6.3 Energy Harvester with Embedded Piezoelectric Stacks

This section presents a new design and analytical model for a composite energy harvester by using embedded piezoelectric stacks. The in-plane polarization of the piezoelectric elements is used to maximize the electrical voltage/charge output. The presented model is applicable to composite beams with structural strain rate damping and embedded piezoelectric stacks. In the same way, the steady state vibration response of the composite harvester subjected to a harmonic base motion is obtained and electrical outputs are analytically derived. Moreover, a parametric study for the composite energy harvester with different embedded piezoelectric stacks number, length, and thickness in a wide frequency domain is done. Finally, the new design is compared to a conventional unimorph harvester with identical geometrical and material properties. The comparison of results demonstrated better electrical outputs by the proposed new harvester [81].

Piezoelectric materials can be configured in many various shapes advantageous for energy harvesting. A large portion of conventional energy harvester designs are unimorph or bimorph structures. These two configurations use the piezoelectric out-of-plane polarization (piezoelectric coefficient d_{31}). On the other hand, by using the stack configuration where strain and piezoelectric polling directions coincide, the in-plane polarization is employed (piezoelectric coefficient d_{33}). For piezoelectric materials, the d_{33} piezoelectric coefficient is usually much larger than the d_{31} coefficient. Therefore, it is more desirable for an energy harvester to operate in the in-plane polarization mode when the electric field and the strain direction coincide. Based on [129], the voltage sensitivity can be also increased by using suitable electrode systems for pure d_{33} mode operation. Thus, a novel analytical model for a composite energy harvester with embedded piezoelectric stacks using the pure in-plane polarization is presented [81].

This section of the thesis is reproduced with some modifications from [A. Keshmiri, X. Deng, N. Wu "New energy harvester with embedded piezoelectric stacks", Composites Part B: Engineering, 163, 303-313, 2019] with permission from the "Elsevier B.V.".

6.3.1 Theoretical Model

The proposed piezoelectric energy harvester configuration consists of a uniform composite beam with two different sections along the length. The first section includes piezoelectric layers perfectly bonded to the substructure layer acting as the core material and the second part is the host beam itself, Fig. 6-11(a). The geometry of the composite structure is described by L_c length of the composite part, L_s length of the homogeneous part, b width of the structure, h_p thickness of the piezoelectric patch, and h_s thickness of the core material in the composite section [81].

It is assumed that the electrode layer is made of a Polyvinylidene thin film (CuNi, Au, etc.) by sputtering a thin metal alloy layer on the piezoelectric stack. Therefore, the thickness is negligible [130]. Since the piezoelectric polarization direction is along the bending stress in *z* direction, piezoelectric stacks are working by d_{33} mode. On the other hand, Fig. 6-11(b) depicts a conventional unimorph piezoelectric energy harvester with identical geometrical and material properties. The electromechanical outputs of these two energy harvesters will be analytically derived and compared [81].

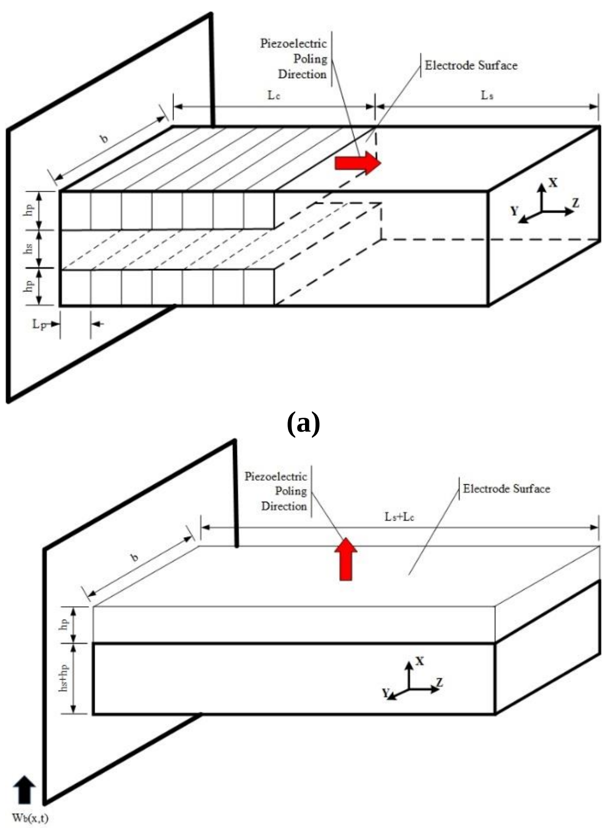

(b)

Fig. 6-11 Two piezoelectric energy harvester configurations [81]. (a) Composite cantilever energy harvester with embedded piezoelectric stacks (piezoelectric poling is along *z* direction). (b) Unimorph cantilever energy harvester with surface bonded piezoelectric patches (piezoelectric poling is along *x* direction in traditional unimorph design).

As illustrated in Fig. 6-12, two sets of connections for piezoelectric stacks can be expected. According to Fig. 6-12(a), piezoelectric stacks are attached mechanically in series but electrically in parallel with electrodes covering their surface in *xy* plane. Although the parallel connection does not increase the output voltage, a multilayer stack design can offer much larger electrode area, higher electric current, and lower impedance to better match the impedance of the electrical device [131]. On the other hand, piezoelectric stacks can be linked mechanically and electrically in series with electrodes covering their surface in *xy* plane, Fig. 6-12(b). Generally, stacking piezoelectric elements mechanically in series and electrically in parallel (same voltage and additive charge) has the effect of stepping down peak voltage and stepping up the effective capacitance compared to the mechanically and electrically in series system. Assuming identical material and geometry, both configurations produce the same power into matched loads. However, the electrically parallel stack configuration is desired due to lower matching electrical load required. It decreases the output voltage to a reasonable size and also the higher capacitance is important for energy transfer [105]. As a result, the piezoelectric stacks connected mechanically in series but electrically in parallel are used in the remainder of this section of the thesis [81].

The energy harvesting efficiency of the composite piezoelectric energy harvester can be investigated by harmonically moving its base in the *x* direction. Therefore, the mechanical vibration input for the system is achieved through $w_b(t)=Ye^{j\varphi t}$ where Y is the amplitude of the base displacement, φ is the angular frequency of the vibration, and j is the unit imaginary number [81].

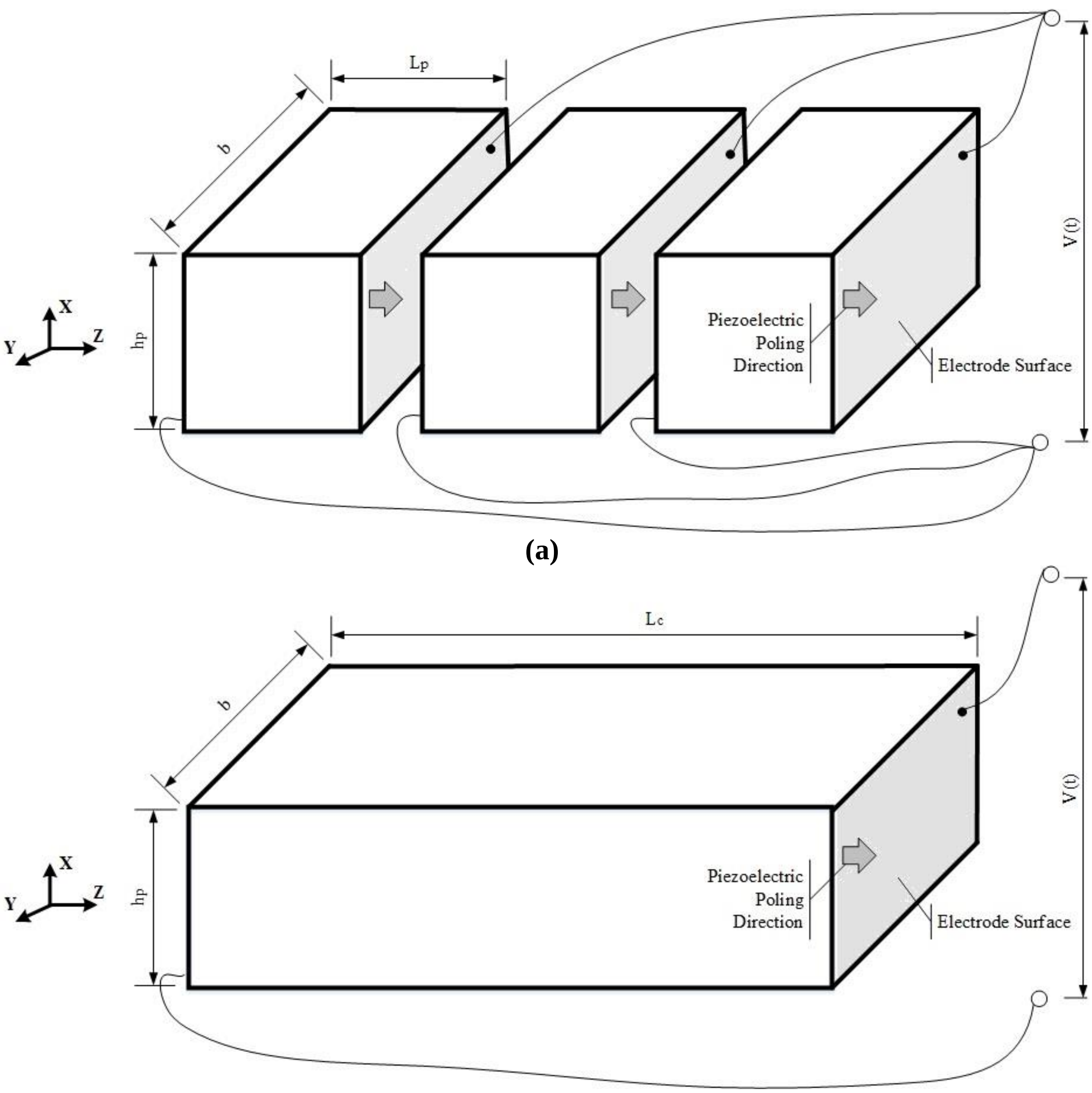

Fig. 6-12 Piezoelectric stacks electrical connections with electrodes covering the stack surface in *xy* plane [81]. (a) Piezoelectric stacks in parallel. (b) Piezoelectric stacks in series.

The differential equation governing the forced lateral vibration of a composite beam with structural strain rate damping can be expressed by,

$$m\frac{\partial^2 w(z,t)}{\partial t^2}+\frac{\partial^2}{\partial z^2}\left[\frac{\partial^2 M(z,t)}{\partial z^2}+C_s I\frac{\partial^3 w(z,t)}{\partial z^2 \partial t}\right]=-m\frac{\partial^2 w_b(t)}{\partial t^2}, \tag{6-19}$$

where z is the position variable along the length, t is the time variable, m is the mass per unit length of the beam, $w(z,t)$ is the deflection function, $M(z,t)$ is the internal bending moment function, C_s is the strain rate damping coefficient, and I is the second moment of area [81].

Following Erturk and Inman approach [126], the internal bending moment can be calculated by integrating the moment of stress distribution at the beam cross-section. Consequently, it can be written as,

$$\begin{cases} M(z,t)=-\int_{h_1}^{h_2}\sigma_z^s bx\mathrm{d}x-\int_{h_2}^{h_2+h_p}\sigma_z^p bx\mathrm{d}x & 0\le z\le L_c \\ M(z,t)=-2\int_0^{\frac{h_s+h_p}{2}}\sigma_z^s bx\mathrm{d}x & L_c\le z\le L_s \end{cases}, \tag{6-20}$$

where σ_z^s and σ_z^p are stresses in the host and piezoelectric structures along the z direction, respectively [81].

It is noted that in the bending situation, one set of piezoelectric stacks sustain tensile stresses and the other set are under compressive stresses. Since the stack configuration cannot withstand tensile load, the structure acts like a unimorph system [81]. Additionally, h_1 is the distance between host structure's bottom and neutral axis of the composite section and h_2 is the distance between piezoelectric layer's bottom and neutral axis of the composite section expressed as,

$$h_1=-\frac{h_p^2+2h_p h_s+\frac{E_s}{E_p}h_p^2}{2(h_p+\frac{E_s}{E_p}h_s)}, \tag{6-21}$$

$$h_2 = \frac{h_p^2 + 2\frac{E_s}{E_p}h_p h_s + \frac{E_s}{E_p}h_p^2}{2(h_p + \frac{E_s}{E_p}h_s)} - h_p. \tag{6-22}$$

Stresses in Eq. (6-20) can be obtained as,

$$\sigma_z^s = E_s \varepsilon_z^s, \tag{6-23}$$

$$\sigma_z^p = E_p(\varepsilon_z^p - d_{33}E_3), \tag{6-24}$$

where ε_z is the strain, E_s is the host structure elasticity modulus, E_p is the piezoelectric elasticity modulus, d_{33} is the piezoelectric coefficient, and E_3 is the electric field all along the 3 or z direction. It should be noted that 1, 2 and 3 directions are aligned with x, y, and z axes, respectively. Additionally, subscript/superscript s and p stand for host structure and piezoelectric stack [81].

Eq. (6-24) is obtained from the piezoelectric constitutive relation where $\varepsilon_3 = d_{33}E_3 + s_{33}^E\sigma_3$ in which s_{33}^E is the elastic compliance and reciprocal of E_p. However in this case, the piezoelectric layer is only subjected to an external stress field and generates electrical charge in response. Since there is no external electric field on the piezoelectric patch (E_3=0), the sensor constitutive relation reduces to $\varepsilon_3 = s_{33}^E\sigma_3$. It is worth mentioning that the direction of axial strain and polarization are the same for piezoelectric patches [81]. Finally, internal moment by expressing the strains in terms of radius of curvature $\varepsilon_z = -x\frac{\partial^2 w(z,t)}{\partial z^2}$ is defined as,

$$\begin{cases} M(z,t) = \int_{h_1}^{h_2} E_s b \frac{\partial^2 w(z,t)}{\partial z^2} x^2 \mathrm{d}x + \int_{h_2}^{h_2+h_p} E_p b \frac{\partial^2 w(z,t)}{\partial z^2} x^2 \mathrm{d}x & 0 \le z \le L_c \\ M(z,t) = 2\int_0^{\frac{h_s+h_p}{2}} E_s b \frac{\partial^2 w(z,t)}{\partial z^2} x^2 \mathrm{d}x & L_c \le z \le L_s \end{cases}. \tag{6-25}$$

Eq. (6-25) can be rewritten as,

$$\begin{cases} M(z,t) = \left(E_s I_s + E_p I_p\right)\frac{\partial^2 w(z,t)}{\partial z^2} & 0 \le z \le L_c \\ M(z,t) = E_s I_s' \frac{\partial^2 w(z,t)}{\partial z^2} & L_c \le z \le L_s \end{cases}, \tag{6-26}$$

where I_s, I_p, and I_s' are defined as,

$$I_s = \int_{h_1}^{h_2} bx^2 \mathrm{d}x = \frac{1}{3}E_s b\left({h_2}^3 - {h_1}^3\right), \tag{6-27}$$

$$I_p = \int_{h_2}^{h_2+h_p} bx^2 \mathrm{d}x = \frac{1}{3}E_p b\left(\left(h_2 + h_p\right)^3 - {h_2}^3\right), \tag{6-28}$$

$$I_s' = 2\int_0^{\frac{h_s+h_p}{2}} E_s bx^2 \mathrm{d}x = \frac{2}{3}E_s b\left(\frac{h_s+h_p}{2}\right)^3. \tag{6-29}$$

Inserting Eq. (6-26) into Eq. (6-19) yields the mechanical governing equation of the lateral motion for a composite energy harvester with embedded piezoelectric stacks written as,

$$\left(E_s I_s + E_p I_p\right)\frac{\partial^4 w(z,t)}{\partial z^4} + C_s I_s \frac{\partial^5 w(z,t)}{\partial z^4 \partial t} + m_c \frac{\partial^2 w(z,t)}{\partial t^2} = -m_c \frac{\partial^2 w_b(t)}{\partial t^2} \quad 0 \le z \le L_c, \tag{6-30}$$

$$E_s I_s' \frac{\partial^4 w(z,t)}{\partial z^4} + C_s I_s' \frac{\partial^5 w(z,t)}{\partial z^4 \partial t} + m_s \frac{\partial^2 w(z,t)}{\partial t^2} = -m_s \frac{\partial^2 w_b(t)}{\partial t^2} \quad L_c \le z \le L_s, \tag{6-31}$$

where $m_c=\rho_s A_s+2\rho_p A_p$ and $m_s=\rho_s(A_s+2A_p)$ are masses per unit length for two sections. In addition, $A_s=bh_s$ and $A_p=bh_p$ are cross-sectional areas [81].

The lateral vibration motion of the composite structure can be represented by a linear combination of the normal modes of the beam defined as $w(z,t) = \sum_{i=1}^{\infty} Z_i(z)T_i(t)$, where $Z_i(z)$ is normal mode and $T_i(t)$ is modal participation coefficient for the ith vibration mode. The eigenfunctions represented by $Z_i(z)$ are mass normalized modes of the corresponding free vibration problem given by,

$$Z_i^c(z) = \sum_{n=0}^{\infty} Z_n^c(z) = \begin{cases} Z_0^c = A_1 + A_2 z + A_3 \frac{z^2}{2!} + A_4 \frac{z^3}{3!} \\ Z_{k+1}^c = -O_z^{-1}\left[-\omega_i^2 \frac{m_c L_c^4}{EI_c} Z_k^c\right] \quad k \geq 0 \end{cases} \quad 0 \leq z \leq L_c, \tag{6-32}$$

$$Z_i^s(z) = \sum_{n=0}^{\infty} Z_n^s(z) = \begin{cases} Z_0^s = A_5 + A_6 z + A_7 \frac{z^2}{2!} + A_8 \frac{z^3}{3!} \\ Z_{k+1}^s = -O_z^{-1}\left[-\omega_i^2 \frac{m_s L_s^4}{EI_s} Z_k^s\right] \quad k \geq 0 \end{cases} \quad L_c \leq z \leq L_s, \tag{6-33}$$

where normal mode functions are determined by the same methodology comprehensively described in section 4.1 of this thesis. Similarly, ω_i is the *i*th undamped natural frequency. Furthermore, A_1 to A_8 are unknown parameters that should be evaluated using boundary and continuity conditions [81] given as,

$$z = 0 \rightarrow \begin{cases} Z^c(z) = 0 \\ \frac{\mathrm{d}Z^c(z)}{\mathrm{d}z} = 0 \end{cases}, \quad z = L_c + L_s \rightarrow \begin{cases} E_s I_s' \frac{\mathrm{d}^2 Z^s(z)}{\mathrm{d}z^2} = 0 \\ \frac{\mathrm{d}}{\mathrm{d}z}\left(E_s I_s' \frac{\mathrm{d}^2 Z^s(z)}{\mathrm{d}z^2}\right) = 0 \end{cases}, \tag{6-34}$$

$$z = L_c \rightarrow \begin{cases} Z^c(z) = Z^s(z) \\ \frac{\mathrm{d}Z^c(z)}{\mathrm{d}z} = \frac{\mathrm{d}Z^s(z)}{\mathrm{d}z} \end{cases}, \quad \begin{cases} \left(E_s I_s + E_p I_p\right) \frac{\mathrm{d}^2 Z^c(z)}{\mathrm{d}z^2} = E_s I_s' \frac{\mathrm{d}^2 Z^s(z)}{\mathrm{d}z^2} \\ \left(E_s I_s + E_p I_p\right) \frac{\mathrm{d}^3 Z^c(z)}{\mathrm{d}z^3} = E_s I_s' \frac{\mathrm{d}^3 Z^s(z)}{\mathrm{d}z^3} \end{cases}. \tag{6-35}$$

Therefore, all Z_k components are evaluated. By applying four boundary and four continuity conditions, a system of eight equations with eight unknown constants A_1 to A_8 is derived. For the nontrivial solution, the determinant of the coefficients must be zero which gives the eigenvalue problem. Therefore, ω_i^n which is the *i*th eigenvalue and undamped natural frequency of the beam considering *n*-term mode shape function is calculated [81].

Since damping function does not possess the orthogonality property, it is assumed that the structural damping is in the form of $C_s I_s = (E_s I_s + E_p I_p)$ for the composite section where α and is a constant [46]. Clearly, normal mode eigenfunctions satisfy the orthogonality conditions, Eq. (4-5). As a result, the modal participation coefficients $T_i(t)$ are the solution of the ordinary differential equation,

$$\frac{\mathrm{d}^2 T_i^c(t)}{\mathrm{d}t^2} + 2\xi_i\omega_i \frac{\mathrm{d}T_i^c(t)}{\mathrm{d}t} + \omega_i{}^2 T_i^c(t) = m_c \frac{\partial^2 w_b(t)}{\partial t^2} \int_0^{L_c} Z_i^c(z)\mathrm{d}z, \tag{6-36}$$

where $2\xi_i\omega_i = \alpha\omega_i^2$ and ξ_i is the structural strain rate damping ratio corresponding to the ith vibration mode [121].

In the case of harmonic base motion, the steady state solution of the Eq. (6-36) can be obtained as,

$$T_i^c(t) = \frac{m_c \varphi^2 Y \int_0^{L_c} Z_i^c(z)\mathrm{d}z}{\omega_i^2 - \varphi^2 + j2\xi_i\omega_i\varphi} e^{j\varphi t}. \tag{6-37}$$

Finally, the analytical steady state response of the piezoelectric coupled section of the structure relative to its base is derived as,

$$w(z,t) = \sum_{i=1}^{\infty} Z_i(z) T_i(t) = \sum_{i=1}^{\infty} Z_i^c(z) \frac{m_c \varphi^2 Y \int_0^{L_c} Z_i^c(z)\mathrm{d}z}{\omega_i^2 - \varphi^2 + j2\xi_i\omega_i\varphi} e^{j\varphi t}\ 0 \le z \le L_c. \tag{6-38}$$

To obtain the electrical outputs of the piezoelectric coupled structure in open circuit condition, similar approach to what was described in section 6.1.1 is followed. Here, the piezoelectric layer is subjected to an external stress field and generates electrical charge in response. It should be noted that the backward coupling in the mechanical domain is not considered [46], [121].

Since the piezoelectric stacks work in the 33 mode and the axial stress is only along 3 or *z* axis [81], the sensor equation becomes,

$$D_3(z,t) = d_{33}\sigma_3(z,t). \tag{6-39}$$

The axial stress σ_3 can be calculated in terms of longitudinal bending strain $\varepsilon_3(z,t)$ in the structure as,

$$\sigma_3(z,t) = E_p\varepsilon_3(z,t) = -E_p h_{pc}\frac{\partial^2 w(z,t)}{\partial z^2}, \tag{6-39}$$

where h_{pc} is the distance between composite beam neutral axis and center of the piezoelectric layer [81] defined as,

$$h_{pc} = \frac{\frac{E_s}{E_p}h_s(h_p+h_s)}{2(h_p+\frac{E_s}{E_p}h_s)}. \tag{6-40}$$

The strain varies along the length of the beam and generates various amounts of charge in each piezoelectric stack, which sums up to produce the total charge output of the energy harvester [81]. By doing the integration of electric displacement $D_3(z,t)$ over the electrode surface, electric charge is calculated as,

$$q(t) = \iint \begin{bmatrix} 0 & 0 & D_3 \end{bmatrix} \begin{bmatrix} dA_1 \\ dA_2 \\ dA_3 \end{bmatrix} = d_{33}E_p h_{pc} b h_p \sum_{k=0}^{N_p} \frac{\partial^2 w(z,t)}{\partial z^2} \Big|_{z=\frac{(k-1)L_p+kL_p}{2}}, \tag{6-41}$$

where dA_1, dA_2, and dA_3 are components of the electrode area in the 2-3, 1-3, and 1-2 planes, respectively. Additionally, N_p is the number of piezoelectric stacks and obviously $N_pL_p=L_c$ [81].

According to Eq. (6-41), the generated charge is only dependent on curvature distribution over the piezoelectric coupled part of the composite harvester. Furthermore, it has been assumed that the electrode area is covering the entire surface of each stack and they are connected in parallel, Fig. 6-12(a) [81]. Hence, for the open circuit case, the generated voltage $V(t)$ can be calculated by dividing the produced electric charge to the capacitance of the piezoelectric stacks C_p,

$$V(t) = \frac{q(t)}{C_p} = \frac{d_{33}E_p h_{pc} b h_p}{C_p} \sum_{k=0}^{N_p} \frac{\partial^2 w(z,t)}{\partial z^2} \bigg|_{z=\frac{(k-1)L_p + kL_p}{2}}, \tag{6-42}$$

where piezoelectric capacitance can be defined as $C_p=N_p\varepsilon_{33}bh_p/L_p$ and ε_{33} is the permittivity component [81].

In the case of harmonic base motion where $w_b(t)=Ye^{j\varphi t}$, the steady state electric charge and voltage output can be obtained. In order to provide a more general form of steady state responses, FRFs are obtained and presented [81]. Electrical charge and voltage output FRFs are defined as the ratio of the steady state charge/voltage to the translational base displacement as,

$$\frac{q(t)}{-Ye^{j\varphi t}} = d_{33}E_p h_{pc} b h_p m_c \sum_{i=1}^{\infty} \left(\frac{\varphi^2 \int_0^{L_c} Z_i^c(z)dz}{\omega_i^2 - \varphi^2 + j2\xi_i\omega_i\varphi} \sum_{k=0}^{N_p} \frac{d^2 Z_i^c(z)}{dz^2} \bigg|_{z=\frac{(k-1)L_p + kL_p}{2}} \right), \tag{6-43}$$

$$\frac{v(t)}{-Ye^{j\varphi t}} = \frac{d_{33}E_p h_{pc} L_p m_c}{N_p \varepsilon_{33}} \sum_{i=1}^{\infty} \left(\frac{\varphi^2 \int_0^{L_c} Z_i^c(z)dz}{\omega_i^2 - \varphi^2 + j2\xi_i\omega_i\varphi} \sum_{k=0}^{N_p} \frac{d^2 Z_i^c(z)}{dz^2} \bigg|_{z=\frac{(k-1)L_p + kL_p}{2}} \right). \tag{6-44}$$

The presented method can accurately model the coupled system dynamics for various excitation frequencies. Therefore, Eqs. (6-43) and (6-44) are the multi-mode FRFs since all vibration modes are included [81].

6.3.2 Simulations and Discussion

Based on the developed model, electrical outputs of the composite piezoelectric energy harvester can be analytically obtained. Numerical examples are presented to demonstrate the validity and efficiency of the proposed model [81].

As an illustration, a beam like Fig. 6-11(a) with PIC252 (modified Lead Zirconate-Lead Titanate) piezoelectric stack is considered with the geometric dimensions, material properties, and electromechanical coefficients listed in Table 6-3 [81]. Considering the manufacturing feasibility, the minimum thickness and height of the single piezoelectric patch are restricted to be larger than 2mm and 0.5mm based on the piezoceramics available in the market [130].

Table 6-3 Geometry and material properties of a uniform composite energy harvester [81].

L_s (m)	L_c (m)	b (m)	h_s (m)	h_p (m)	E_s (GPa)	S_{11}^E (m^2/N)	S_{33}^E (m^2/N)	ρ_s (kg/m^3)	ρ_p (kg/m^3)	d_{31} (pm/V)	d_{33} (pm/V)	ε_{33} (nF/m)
0.4	0.4	0.05	0.01	0.002	68.9	$16.1*10^{-12}$	$20.7*10^{-12}$	2700	7800	-180	400	15.494

The excitation of the piezoelectric energy harvester is due to the harmonic base translation and the steady state dynamic response of the system is of interest. Moreover, structural strain rate damping ratios for the first two vibration modes are assumed to be $\xi_1=\xi_2=0.01$. Finally, two steady state FRFs, electric charge and voltage output, are studied. Based on the convergence study for vibration analysis of non-uniform beams, 10 terms of mode shape function series (n=10) are used to accurately present the first and second vibration modes [81].

Fig. 6-13 displays the electric charge and voltage output FRFs for the composite energy harvester with different numbers of piezoelectric stacks embedded in a constant length L_c, as shown in Fig. 6-11(a). As can be seen in Fig. 6-13(a), increasing the number of piezoelectric stacks embedded in the structure leads to larger electric charge output. In other words, embedding thinner piezoelectric stacks results in higher produced charge. This is due to the fact that more piezoelectric stacks mean larger electrode area, which finally produces more electric charge. On the other hand, thicker piezoelectric stacks are favorable for larger voltage outputs because of the smaller piezoelectric capacitance, Fig. 6-13(b) [81].

Fig. 6-14 graphically indicates the relationship between the electrical FRFs and length of the embedded piezoelectric part, L_c. Based on Figs. 6-14(a) and 6-14(b), increasing the length of the piezoelectric embedded section results in lower first natural frequencies of the system which is definitely favorable in low frequency energy harvesting applications. According to Eq. (6-41), the produced electric charge is only dependent on the curvature distribution over the piezoelectric coupled part of the composite harvester. Due to high mechanical stiffness of the stack configuration, increasing the composite section length does not lead to higher generated charge. This issue will not happen in higher mode shapes because of larger curvature distribution. As can be seen in Fig. 6-14(a), up to 1.94 times higher peak electric charge for the second vibration mode is achieved by increasing the L_c from 0.3m to 0.5m. According to Fig. 6-14(b), the lower mode electrical output problem for the voltage is not reported. This is due to the fact that equal numbers of piezoelectric stacks are used in all of the simulations. As a result, the composite harvester with larger L_c is benefiting from piezoelectric stacks with larger length and consequently lower capacitance. Thus, greater voltage output is achieved by using a longer piezoelectric embedded part for all of the mode shapes. As shown in Fig. 6-14(b), up to 3.50 times higher peak voltage by increasing the L_c from 0.3m to 0.5m is reported [81].

The effect of piezoelectric stacks size (h_p) on the electric FRFs is examined in Fig. 6-15. According to Fig. 6-15(a), bigger piezoelectric stack means larger electric charge which is certainly achieved through greater electrode area. On the contrary, piezoelectric stack cross-sectional area does not affect the voltage output. Hence, larger h_p leads to lower h_{pc} which causes the destructive effect on the generated voltage, Fig. 6-15(b). Lastly, the large size effect is in favor of low frequency energy harvesting. As shown in Fig. 6-15, increasing piezoelectric stack size results in lower natural frequency of the harvester [81].

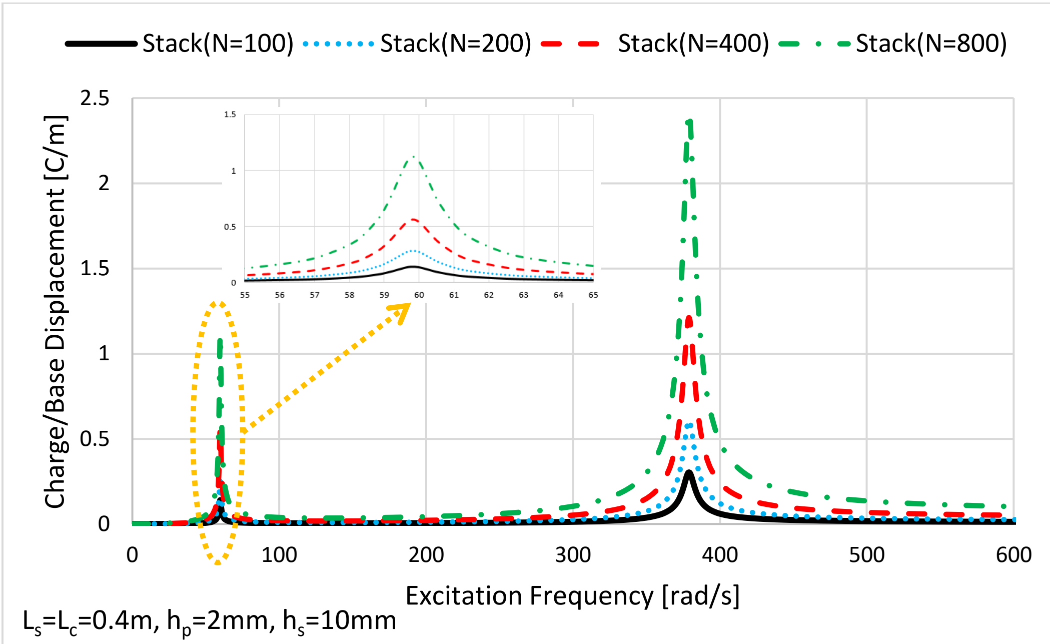

(a)

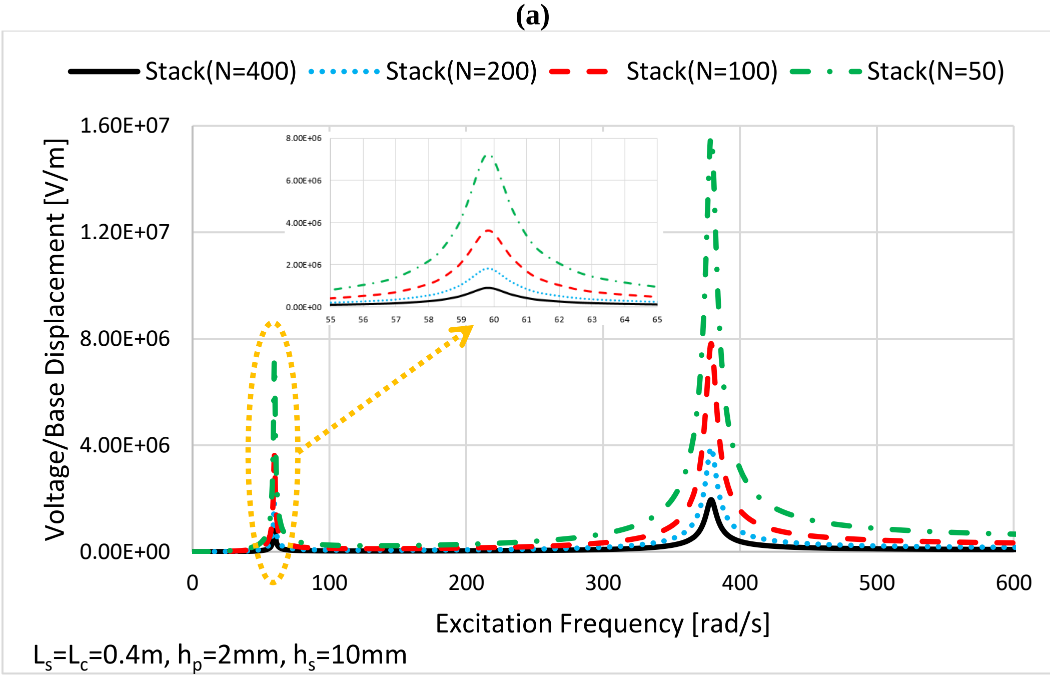

(b)

Fig. 6-13 Electric charge and voltage output FRFs for the composite energy harvester with different numbers of piezoelectric stacks [81]. (a) Electric charge FRF. (b) Voltage output FRF.

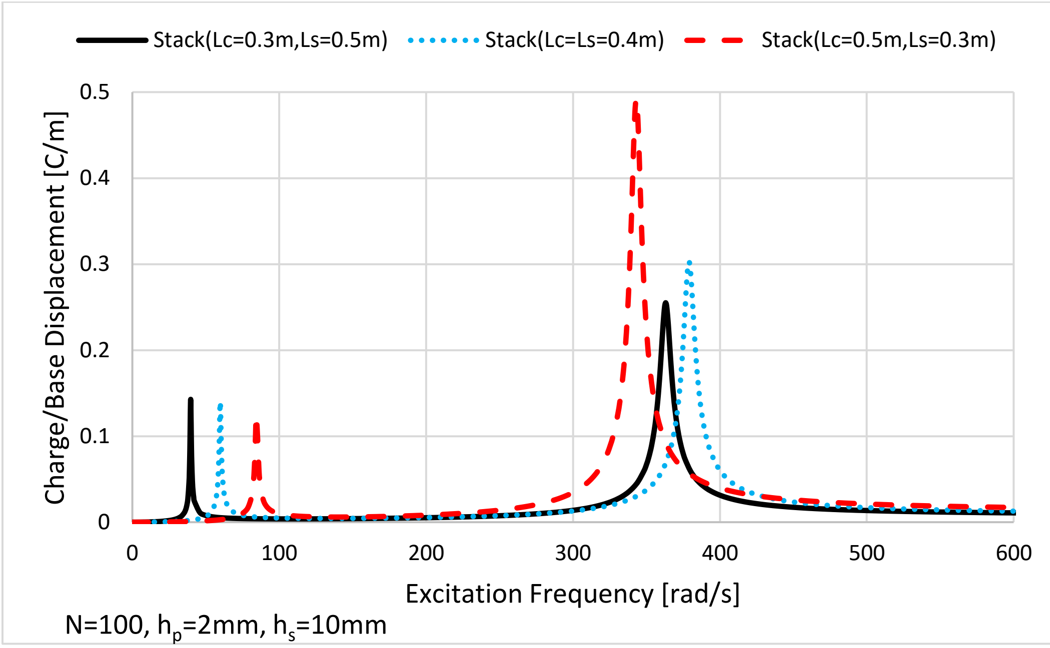

(a)

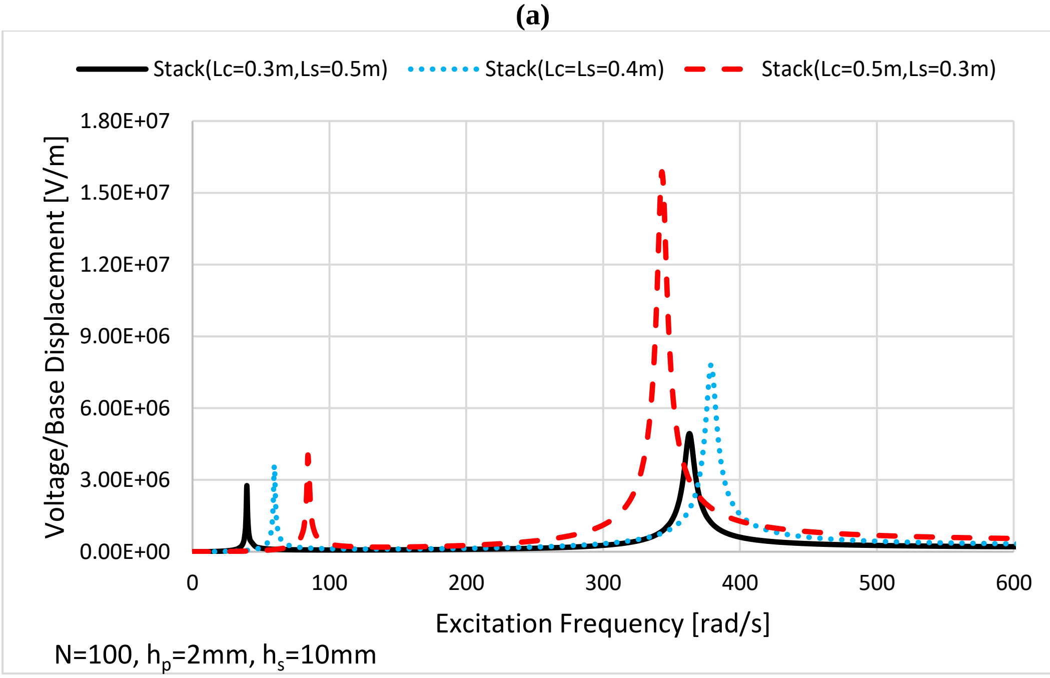

(b)

Fig. 6-14 Electric charge and voltage output FRFs for the composite energy harvester with different length of the embedded section [81]. (a) Electric charge FRF. (b) Voltage output FRF.

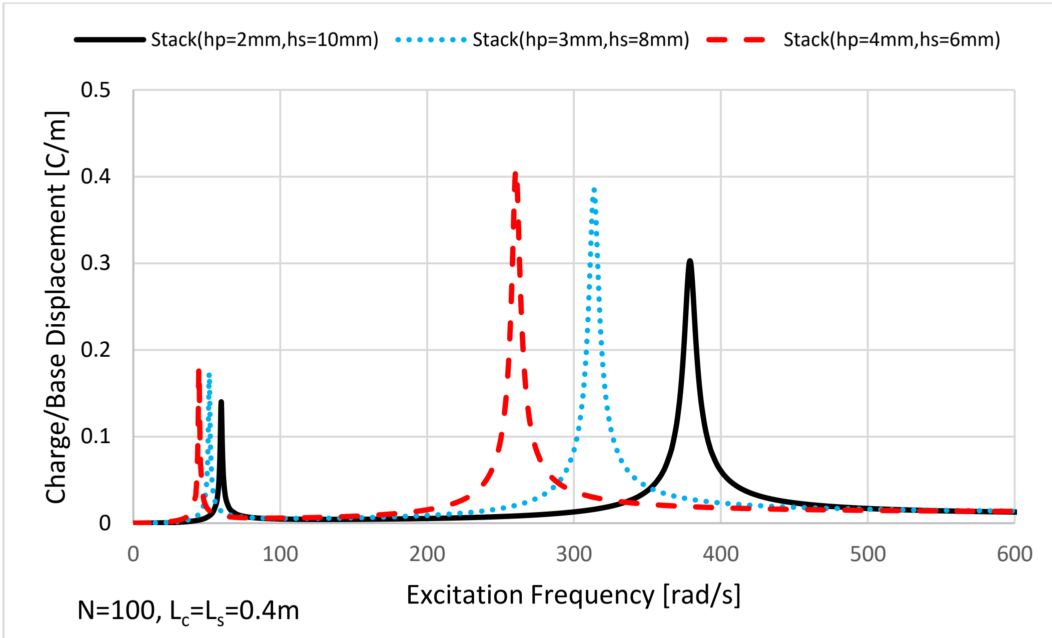

(a)

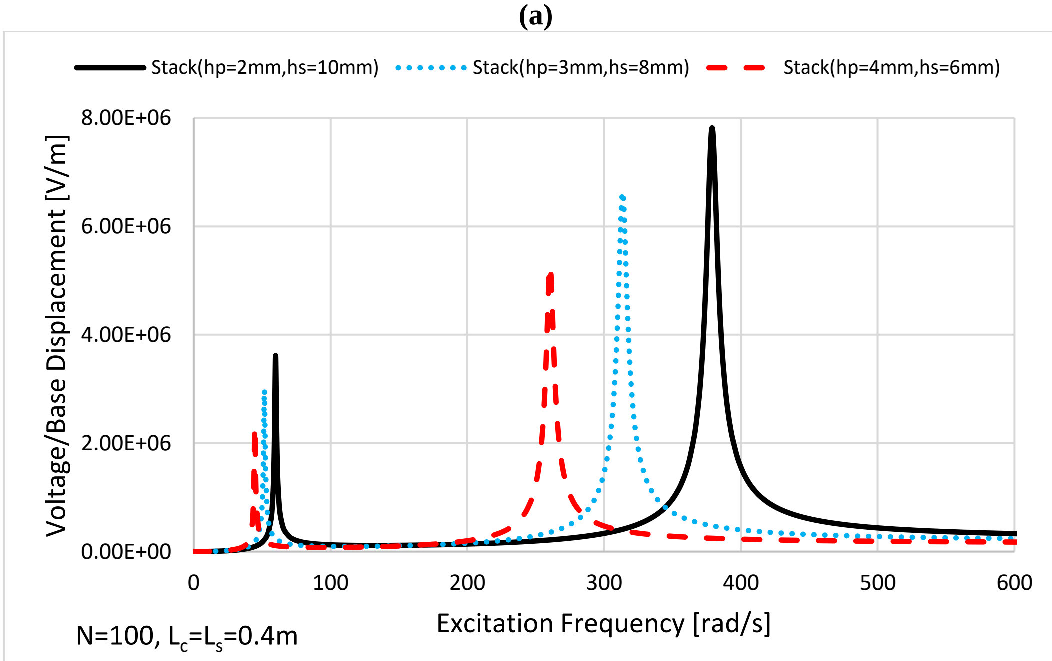

(b)

Fig. 6-15 Electric charge and voltage output FRFs for the composite energy harvester with different piezoelectric stacks size [81]. (a) Electric charge FRF. (b) Voltage output FRF.

The electrical outputs of the stack design with various configurations are compared to that of a conventional unimorph harvester with identical geometrical and material properties in Fig. 6-16. As shown in Fig. 6-16(a), the peak electric charge for the stack design can be up to 3.18 and 1.82 times higher than the unimorph for the first and second natural frequencies even by using relatively thick (L_p=2mm, N=200) piezoelectric stacks. This positive effect can be significantly strengthened by using thinner stacks as demonstrated in Fig. 6-13(a). It should be noted that the superior electric charge generation behavior of the unimorph harvester in the higher modes is due to benefiting from the larger strain distribution along the length of the beam. However, this problem can be easily solved by using thinner piezoelectric stacks. On the contrary, significantly superior voltage generation behavior for the stack design compared to the unimoprh can be seen in Fig. 6-16(b). As shown, the peak output voltage for relatively thick (N=200) stack configurations can be up to 5.59 and 4.48 times higher for first and second vibration modes, compared with the unimorph harvester. As previously mentioned, thicker piezoelectric stacks are favorable for larger voltage outputs [81].

It is noted that the analytical model tries to theoretically investigate a new possible design for generating more electrical outputs. It does not necessarily lead to higher power generation in all of the possible cases. In fact, depending on the electrical requirements on the other side of the circuit, higher electric charge or voltage can be generated by deploying the proposed design compared to the unimorph harvester with identical geometrical and material properties [81].

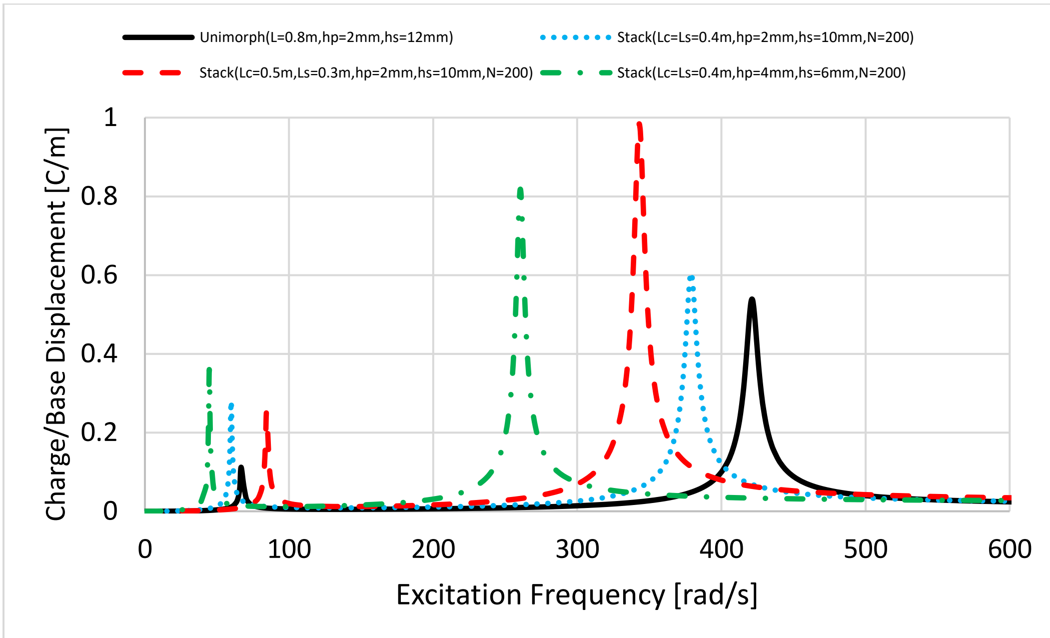

(a)

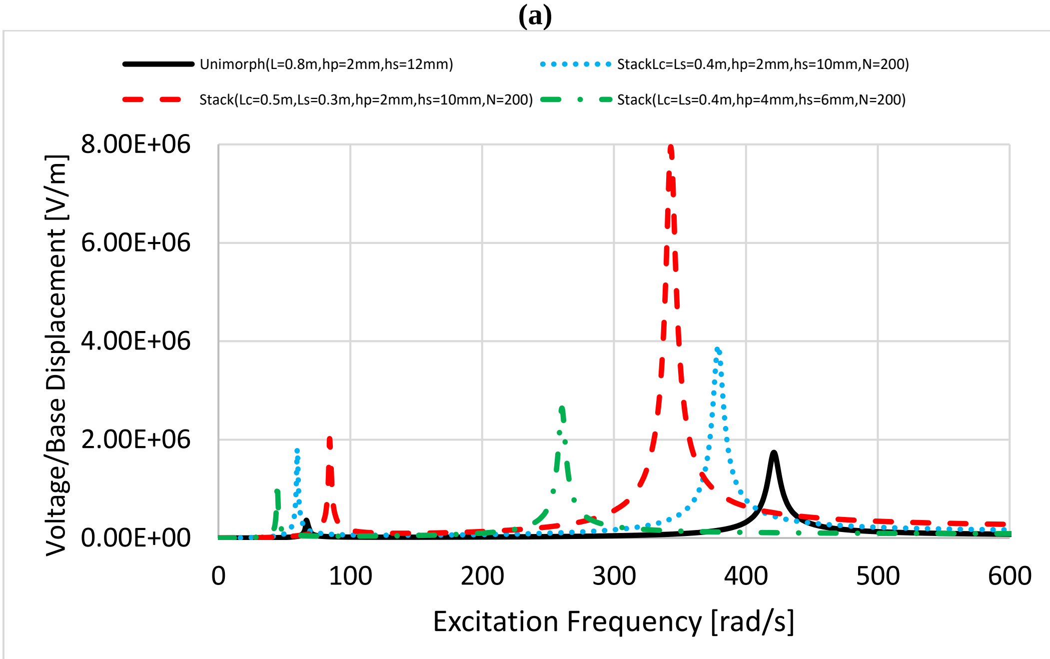

(b)

Fig. 6-16 Electric charge and voltage output FRFs for the composite energy harvester with different configurations compared to the electrical outputs of the identical unimorph harvester design [81]. (a) Electric charge FRF. (b) Voltage output FRF.

6.3.3 Conclusion

This section of the thesis presented a new analytical model for a composite energy harvester with embedded piezoelectric stacks using the pure in-plane polarization. Depending on the electrical requirements, higher electric charge or voltage can be generated by deploying the proposed design [81].

Based on the parametric study, effects of piezoelectric stacks number, length and size as well as the excitation frequency on the electric charge and output voltage are comprehensively investigated and the following results are concluded [81]:

- Embedding thinner piezoelectric stacks in the structure results in higher produced electric charge due to larger electrode area. Conversely, thicker piezoelectric stacks are more favorable for higher voltage outputs because of the smaller piezoelectric capacitance.
- Increasing the length of the piezoelectric embedded section leads to higher charge and voltage outputs, especially for higher vibration modes.
- Higher piezoelectric size means larger electric charge which is achieved through greater electrode area. On the contrary, larger piezoelectric size leads to lower neutral axis distance and results in lower generated voltage.
- The electrical charge and voltage outputs of the new composite design show great improvement compared to that of a conventional unimorph harvester with identical geometrical and material properties.

- By using the stack configuration where strain and piezoelectric polling directions coincide, the in-plane polarization is employed. For piezoelectric materials, the in-plane piezoelectric coefficient is usually larger than the out-of-plane coefficient. Therefore, it is more desirable for an energy harvester to operate in the in-plane polarization mode when the electric field and the strain direction coincide.
- The embedded stack design decreases the natural frequencies of the energy harvester. This is greatly useful for low frequency energy harvesting.

6.4 Energy Harvesting Platform with Piezoelectric Stacks Boundary

This section presents another new design and analytical model for energy harvesting applications. In addition, simulation-based optimization method is utilized to find the optimum mechanical design. It is noted that this is just a preliminary introduction to the simulation-based optimization technique by using machine learning models for the design of piezoelectric energy harvesters. This introductory idea could pave the way for more advanced optimization models and studies in the future. This initial study proves that the proposed optimization model and procedure works efficiently for relatively simple systems with few design variables. As a result, it can be used and tested for more complex systems with more variable parameters.

The in-plane polarization of the piezoelectric stacks is employed to maximize the electrical power output. In the same way, the steady state vibration response of the harvester platform subjected to harmonic base motion is obtained and electrical outputs are analytically derived. Furthermore, a comprehensive parametric study for the proposed energy harvester with various design parameters is done. Finally, simulation-based optimization technique helps to find the optimum structural design with maximum efficiency. To solve the optimization problem, an artificial neural network (ANN) is first trained to replace the simulation model and then a genetic algorithm (GA) is employed to find the optimized design variables.

This section of the thesis is reproduced with some modifications from [A. Keshmiri, S. Bagheri, N. Wu "Simulation-Based Optimization of a Non-Uniform Piezoelectric Energy Harvester with Stack Boundary", in preparation]. This section includes material that is the result of joint research with Shahriar Bagheri in the Sound & Vibrations Lab at the University of Manitoba.

6.4.1 Theoretical Model

The proposed piezoelectric energy harvester platform includes a nonlinearly tapered beam of length L having one free end at $x=L$. The other end of the non-uniform beam at $x=0$ is attached to a piezoelectric stack fixture embedded in a solid platform. Since the piezoelectric polarization direction is along the bending stress in the axial direction, piezoelectric stacks are using in-plane polarization with higher piezoelectric coefficient [81]. The structure is transversely fixed and the piezoelectric stacks connection at the beam joint acts as a torsional spring, like shown in Fig. 6-17.

The non-uniform geometry of the structure is described by an exponential function $R_0e^{mx/L}$ where R_0 is the radius of the circular cross-section of the beam at $x=0$, m is the geometry taper ratio, and L is the length. Moreover, r_o, r_i, and h_p are outer radius, inner radius, and thickness of the piezoelectric ring, respectively. Lastly, it is presumed that the electrode layer is made of a Polyvinylidene thin film

(CuNi, Au, etc.) that means the electrode thickness is negligible [130]. It is noted that the model does not consider the mechanical effect of thin electrode layer.

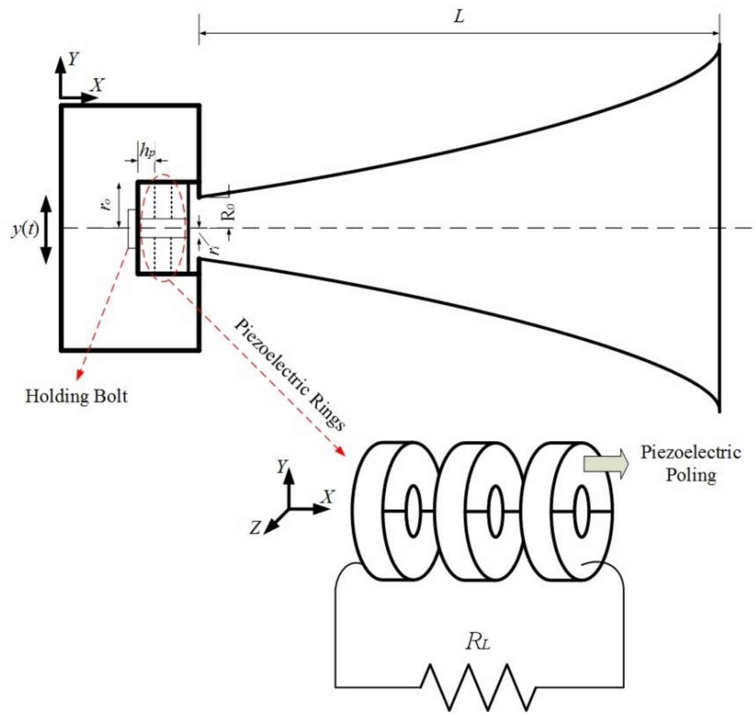

Fig. 6-17 Piezoelectric energy harvester platform with piezoelectric stacks.

The energy harvesting efficiency of the harvester can be investigated by setting the mechanical vibration input for the system in the form of $y(t) = Y \sin \varphi t$, where Y is the amplitude of the base displacement and φ is the angular frequency of the harmonic excitation. Hence, the forced lateral vibration of the non-uniform structure can be expressed by,

$$\rho_s A(x) \frac{\partial^2 w(x,t)}{\partial t^2} + \frac{\partial^2}{\partial x^2}\left[E_s I(x) \frac{\partial^2 w(x,t)}{\partial x^2}\right] = -\rho_s A(x) \varphi^2 Y \sin \varphi t, \quad (6\text{-}45)$$

where x is the position variable along length of the beam, t is the time variable, ρ_s is the density of the beam, $A(x)$ is the cross-sectional area, $w(x,t)$ is the deflection function, E_s is the elasticity modulus of the beam, and $I(x)$ is the second moment of area [46].

In this case, boundary conditions for the non-uniform beam are defined as,

$$[w(x,t)]_{x=0} = \left[E_s I(x)\frac{\partial^2 w(x,t)}{\partial x^2} - K_T\frac{\partial w(x,t)}{\partial \mathrm{x}}\right]_{x=0} = 0,$$
$$\left[E_s I(x)\frac{\partial^2 w(x,t)}{\partial x^2}\right]_{x=L} = \left[\frac{\partial}{\partial x}\left(E_s I(x)\frac{\partial^2 w(x,t)}{\partial x^2}\right)\right]_{x=L} = 0, \tag{6-46}$$

where K_T is the equivalent torsional stiffness of the piezoelectric stack rings. By considering the rotation of the ring cross-section in its plane, the equivalent torsional stiffness of the stack can be expressed as $K_T=[EI/r_o]_{\text{ring}}$ [132].

Following the same analytical process from Eq. (4-4) to Eq. (4-10), mass normalized normal mode eigenfunctions in the recurrence format are derived as,

$$X_0(x) = C_1 + C_2 x + C_3\frac{x^2}{2!} + C_4\frac{x^3}{3!},$$
$$X_{k+1}(x) = -O_x^{-1}\left[2\left(\frac{\frac{dI(x)}{dx}}{I(x)}\right)\frac{\mathrm{d}^3 X_k(x)}{\mathrm{d}x^3} + \left(\frac{\frac{d^2 I(x)}{dx^2}}{I(x)}\right)\frac{\mathrm{d}^2 X_k(x)}{\mathrm{d}x^2} - \omega^2\left(\frac{\rho_s A(x)}{E_s I(x)}\right)X_k(x)\right] \quad k \geq 0. \tag{6-47}$$

Then, the modal participation coefficients $T_i(t)$ are the solution of the ordinary differential equation,

$$\frac{\mathrm{d}^2 T_i(t)}{\mathrm{d}t^2} + \omega_i{}^2 T_i(t) = -\rho_s\varphi^2 Y\left(\int_0^L X_i(x)A(x)\mathrm{d}x\right)\sin\varphi t. \tag{6-48}$$

The steady state solution of Eq. (6-48) can be expressed by,

$$T_i(t) = \frac{\rho_s\varphi^2 Y\left(\int_0^L X_i(x)A(x)\mathrm{d}x\right)}{\omega_i^2-\varphi^2}\sin\varphi t. \tag{6-49}$$

As a result, normal mode eigenfunctions in Eq. (6-47) and modal participation coefficients in Eq. (6-49) are used to derive the dynamic steady state response of the non-uniform structure relative to its base as,

$$w(x,t) = \sum_{i=1}^{\infty} X_i(x) T_i(t) = \sum_{i=1}^{\infty} X_i(x) \frac{\rho_s \varphi^2 Y\left(\int_0^L X_i(x) A(x) \mathrm{d}x\right)}{\omega_i^2 - \varphi^2} \sin \varphi t. \tag{6-50}$$

At that point, the piezoelectric base is subjected to an external stress field and generates electrical charge in response [46]. Following the distributed model presented by Erturk and Inman [126], the sensor constitutive relation reduces to,

$$D_3(x,t) = d_{33} \sigma_3(x,t) + \varepsilon_{33}^{\sigma} E_3, \tag{6-51}$$

where D_3 is the electrical displacement, d_{33} is the in-plane piezoelectric coefficient, σ_3 is the stress acted on the piezoelectric stacks, $e_{33}{}^{\sigma}$ is the permittivity at constant stress, and E_3 is the electrical field along 3-axis. It is noted that 3-axis for piezoelectric patches is aligned with *x* direction along the length of the beam, Fig. 6-17.

The axial stress acting on the piezoelectric stacks along their thickness direction can be expressed in terms of bending strain at the root of the beam. Therefore, the electrical displacement in Eq. (6-51) can be rewritten as,

$$D_3(t) = d_{33} E_s \frac{r_o + r_i}{2} \left(\frac{\partial^2 w(x,t)}{\partial x^2} \Big|_{x=0} \right) - \varepsilon_{33} \frac{V(t)}{N_p h_p}, \tag{6-52}$$

where N_p is the number of piezoelectric stacks, h_p is the piezoelectric stack thickness, ε_{33} is the permittivity component at constant strain, and $V(t)$ is the voltage across the piezoelectric rings.

It is assumed that the piezoelectric rings are thin which means the cross-section dimensions are small compared with the radius [132]. Furthermore, the electrode area covers the surface of each stack and they are connected in series, Fig. 6-17. Consequently, the total electric charge on the electrode of piezoelectric rings considering only half of the area that is under the compression load can be estimated as,

$$q(t) = d_{33} E_s \frac{r_o + r_i}{2} \frac{\pi\left(r_o^2 - r_i^2\right)}{2} \left(\frac{\partial^2 w(x,t)}{\partial x^2} \Big|_{x=0} \right) - \varepsilon_{33} \frac{V(t)}{N_p h_p}. \tag{6-53}$$

Then, the generated electric current can be expressed as,

$$i(t) = \frac{dq(t)}{dt} = d_{33} E_s \frac{r_o + r_i}{2} \frac{\pi\left(r_o^2 - r_i^2\right)}{2} \left[\frac{d}{dt} \left(\frac{\partial^2 w(x,t)}{\partial x^2} \Big|_{x=0} \right) \right] - \frac{\varepsilon_{33} \pi\left(r_o^2 - r_i^2\right)}{2 N_p h_p} \frac{dV(t)}{dt}. \tag{6-54}$$

Based on Erturk and Inman [126], the calculated electric current in Eq. (6-54) is a function of the non-uniform beam vibration and the voltage across piezoelectric rings. As shown in Fig. 6-17, the piezoelectric rings with the capacitance of $\frac{\varepsilon_{33} \pi\left(r_o^2 - r_i^2\right)}{2 N_p h_p}$ are directly connected to the resistive load R_L as a current source. Therefore, the generated voltage across the resistive load is given by,

$$V(t) = R_L i(t) = R_L d_{33} E_s \frac{r_o + r_i}{2} \frac{\pi\left(r_o^2 - r_i^2\right)}{2} \left[\frac{d}{dt} \left(\frac{\partial^2 w(x,t)}{\partial x^2} \Big|_{x=0} \right) \right] - \frac{R_L \varepsilon_{33} \pi\left(r_o^2 - r_i^2\right)}{2 N_p h_p} \frac{dV(t)}{dt}. \tag{6-55}$$

In other words, the electrical differential equation can be rewritten as,

$$\frac{R_L \varepsilon_{33} \pi (r_o^2 - r_i^2)}{2 N_p h_p} \frac{d}{dt} V(t) + \frac{1}{R_L} V(t) = d_{33} E_s \frac{r_o + r_i}{2} \frac{\pi (r_o^2 - r_i^2)}{2} \left[\frac{d}{dt} \left(\frac{\partial^2 w(x,t)}{\partial x^2} \mid_{x=0} \right) \right]. \tag{6-56}$$

By using Eq. (6-50) in Eq. (6-56) and solving the first order differential equation of the electrical circuit, the steady state voltage and then electric current can be found. Lastly, the output electrical power of the energy harvester is calculated as the multiplication of output voltage and charge.

The presented analytical model can be easily used for parametric study to find the effects of various parameters on the efficiency of the energy harvesting system. Here, the efficiency factor η is defined in Eq. (6-57) as the ratio of the root mean square (RMS) of the output electrical power $P_{rms}{}^{e}$ to the RMS of the input mechanical power $P_{rms}{}^{m}$ when the piezoelectric capacitor is charged for the period of T.

$$\eta = \frac{P_{rms}^{e}}{P_{rms}^{m}} = \frac{\sqrt{\frac{1}{T} \int_0^T [V(t) i(t)]^2 dt}}{\sqrt{\frac{1}{T} \int_0^T \left\{ \left[\int_0^L \rho_s A(x) dx \right] \varphi^3 Y^2 \sin \varphi t \cos \varphi t \right\}^2 dt}}. \tag{6-57}$$

According to Eq. (6-57), the efficiency factor is dependent on so many parameters including the vibrational and electromechanical properties of the piezoelectric rings and the non-uniform beam, the resistive load, and also the base excitation amplitude and frequency.

6.4.2 Optimization Model

Depending on the design requirements, certain objectives and parameters should be carefully considered in the optimization process of a mechanical design. The optimization procedure for a mechanical system can result in a complex objective function with a large number of design parameters.

During the past decades, the optimum values of an engineering objective function have been calculated by applying analytical or numerical methods. These classical approaches perform well in some situations, but they mostly fail in practical complex design cases due to large number of design parameters and their nonlinear effect. Thus, advanced optimization algorithms are employed to evaluate the optimization solution within a feasible time and computational cost [133].

In order to offer the optimized design of the proposed harvester, simulation-based optimization technique is used. Here, simulation model is the mathematical model of the electromechanical response of the harvesting system under base motion. One way to find the optimized design is to run the simulation for all possible input parameters. Generally, this approach is not practical in the case of complex simulation models or timely and computationally expensive ones. Therefore, it is more effective to find optimal values for the inputs instead of trying all probable cases. This process without explicitly calculating all of the possibilities is called simulation-based optimization [134]. In order to efficiently find the optimal solution, the mathematical model is resolved by iterative methods that generate sequences of progressively improved approximations, which eventually satisfies the optimal condition [135].

For the presented harvester design, the simulation model running process is timely and computationally complex and expensive. So, it is not reasonable and efficient to use the physical simulation model to find the optimized configuration. Therefore, a small dataset is produced by the simulation model and used to train the ANN, which replaces the simulation model during optimization process.

First, a small database of the design parameters is produced, randomly shuffled, and loaded to train the ANN. Then, the properly trained neural network that is far more computationally efficient compared with the physical simulation model is used to evaluate the objective function during the optimization process. Last of all, GA solves the optimization problem and delivers the optimal design parameters.

6.4.2.1 Artificial Neural Network

Inspired by biological neural networks in the brain, ANN is presented as a computational model to process information [136]. It was noticed that the biological neuron in human brain can conceptualize and learn from large amount of data. This characteristic was used and modelled in machines to create identical capability [137].

Therefore, the neuron was abstracted into a model of inputs, weights, and outputs [137]. The neurons receive input from a dataset they have been given and compute the outputs. To initiate the learning process, initial weights are chosen randomly. Then, the network iteratively updates each of input weights and gradually approximates the primary relationship in the dataset [137]. The errors from each classification of record are returned to the network and used to revise the algorithm for the next round and so on for several iterations [138]. Once the neural network is properly trained, it can be used to generate new accurate dataset.

Here in this model, a dataset of variable design parameters and energy harvesting efficiency is loaded and randomly shuffled to prevent any biased conclusions based on the order of the samples. In order to train the neural network, the steps represented in Fig. 6.18 are followed.

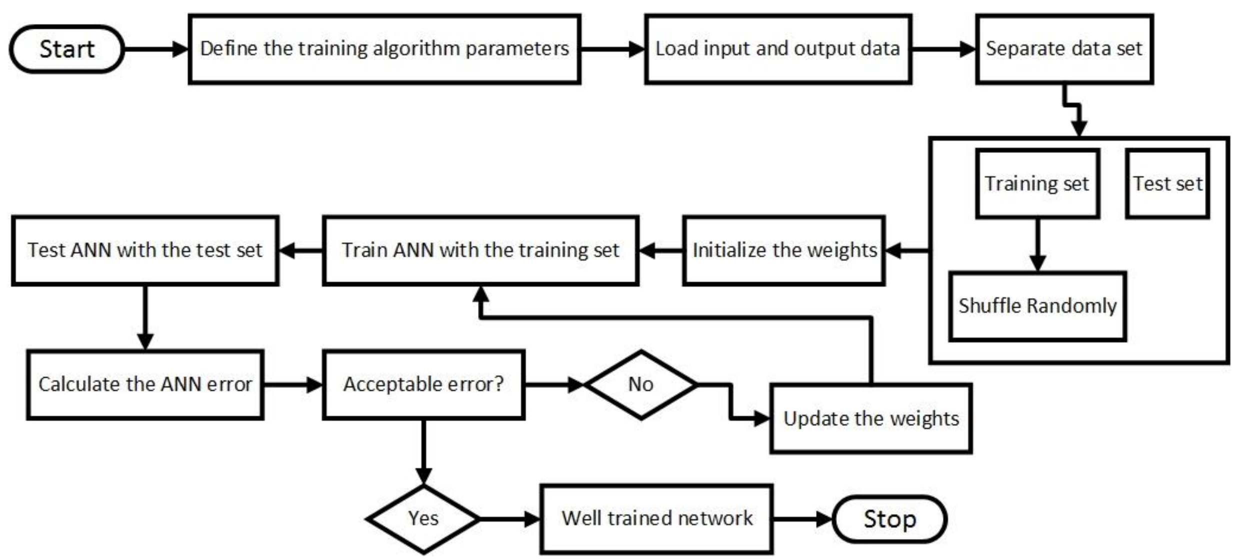

Fig. 6-18 The training steps of the ANN structure.

6.4.2.2 Genetic Algorithm

GA is a type of optimization and search technique based on the principles of genetics and natural selection. According to the indicated selection rules, a population of numerous individuals evolves to maximize the fitness or objective function [139]. The historical information is efficiently investigated to find new search points with expected improved performance [140].

In order to solve an optimization problem with GA and maximize the objective function, several steps should be followed. First, initial set of points generates the initial population. Then, the objective function is evaluated. Based on this evaluation, a new population is created. The second population is created from the initial one by certain operations called mutation. The goal is to create a new population with higher objective function value. The entire procedure is iteratively repeated and new populations are generated until the benchmark or certain number of iterations is reached and termination criterion is met [141]. Based on the procedure perfectly defined by [142], the optimization process by using GAs includes the steps represented in Fig. 6.19.

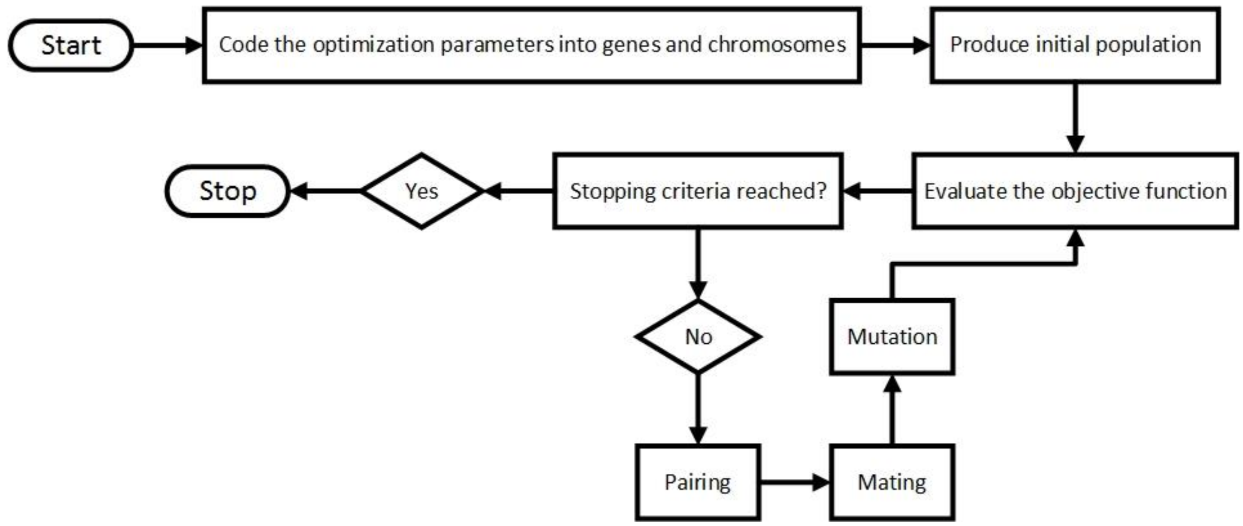

Fig. 6-19 The optimization procedure by using the GA.

6.4.3 Simulations, Optimization, and Discussion

Based on the developed model, the energy efficiency factor of the energy harvester is analytically obtained to examine the effect of various parameters. As an illustration, a beam like Fig. 6-17 with PIC252 piezoelectric stacks embedded in the base is considered with geometric dimensions, material properties, and electromechanical coefficients listed in Table 6-4. Additionally, the upper and lower bounds for each optimization parameter is defined.

The excitation of the piezoelectric energy harvester is due to the harmonic base translation and the steady state dynamic response of the system is of interest. Based on the convergence study for vibration analysis of non-uniform beams, 20 terms of mode shape function series (n=20) are used to accurately present the final vibration mode shape function for the first three vibration modes [1], [22].

Table 6-4 Geometry and material properties of the energy harvester platform.

Non-uniform beam				
Taper ratio	Length (m)	Radius (mm)	Elasticity (GPa)	Density (kg/m^3)
$0 \leq m \leq 0.6$	$0.45 \leq L \leq 0.55$	$3 \leq R_0 \leq 5$	$E_s = 68.9$	$\rho_s = 2700$

Piezoelectric stack ring							
Inner radius (mm)	Outer radius (mm)	Thickness (mm)	Number	Elasticity (GPa)	Density (kg/m^3)	Piezoelectric coefficient (pm/V)	Permittivity coefficient (nF/m)
$1 \leq r_i \leq 2$	$3 \leq r_o \leq 5$	$h_p = 0.1$	$N = 4$	$E_p = 48.3$	$\rho_p = 7800$	$d_{33} = 400$	$\varepsilon_{33} = 15.494$

External load	Excitation	
Electrical resistance (kΩ)	Amplitude (m)	Frequency (rad/s)
$R_L = 10$	$Y = 0.001$	$\varphi_1 = 100$, $\varphi_2 = 200$

For instance, Fig. 6-20 shows the electrical power output for various beam taper ratios ($0 \leq m \leq 0.6$), beam lengths ($0.45\text{m} \leq L \leq 0.55\text{m}$), and two excitation frequencies (φ=100rad/s and 200rad/s) by considering other optimization parameters to be constant. In this particular case, r_i=1mm, r_o=5mm, and T=0.1s. It is noted that all the beams have equal volume and mass.

As can be seen in Table 6-4 and Fig. 6-20, there is a huge number of possible combinations for optimization parameters to find the most efficient design. The output electrical power depends on many different parameters and factors that their effect should be measured and studied carefully. Due to large number of design variables and their impact on the objective function, the simulation model running procedure is complicated and expensive in terms of time and computation power. Thus, it is not practical to use the simulation-based optimization methods to find the optimized design. In order to remedy this problem, an ANN replaces the simulation model. The ANN is used during the optimization process instead of the original timely and computationally expensive simulation model. Then, the genetic algorithm solves the optimization problem. The objective function here in this design is the efficiency factor η in Eq. (6-57).

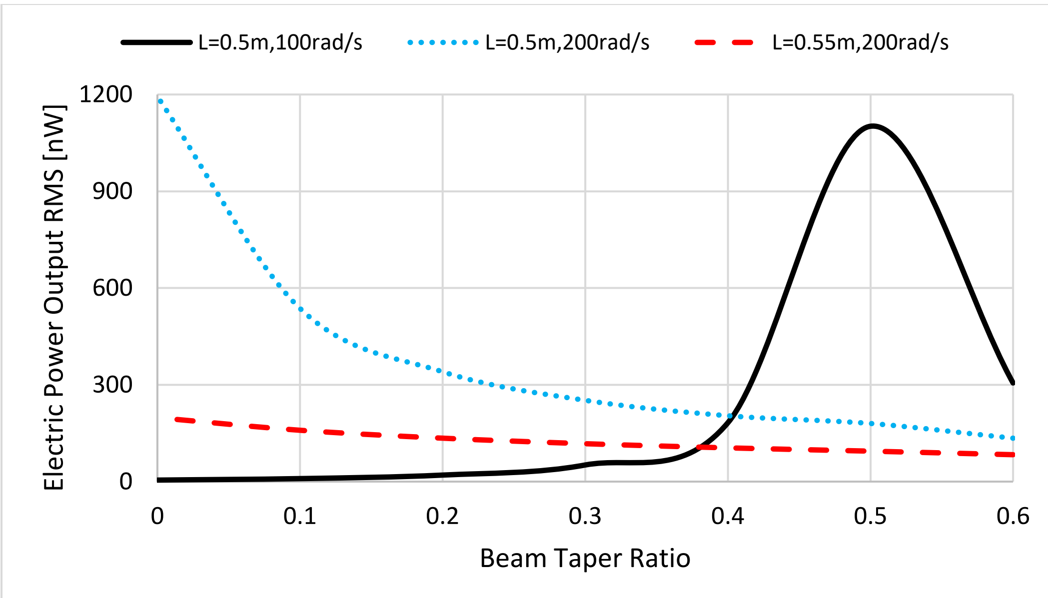

Fig. 6-20 The electrical power output for the platform energy harvester with various beam taper ratios, lengths, and excitation frequencies.

The first and simplest kind of ANNs, feedforward backpropagation architecture, is used here. A typical feedforward backpropagation neural network consists of one input layer, at least one hidden layer, and one output layer. Although the hidden layers are not theoretically limited, they usually are one or two [138]. For the current model, one input layer with four nodes corresponding to four design parameters, two hidden layers, and one output layer with one node corresponding to the efficiency of the harvester is chosen. Additionally, the machine-learning technique used for designing the ANN is the regression model. Regression models define the relationship among a set of inputs and an output [143].

First, a small dataset of the input parameters and the corresponding efficiency output is produced, randomly shuffled, and loaded to train the ANN. A training set is defined which contains 75% of the dataset and is used to train the ANN. The remained 25% of the dataset is used as the test set. The test set evaluates the precision and accuracy of the trained neural network. The measure for performance evaluation of the ANN regression model is calculated by R^2 which is defined as,

$$R^2 = 1 - \frac{\sum_{i=1}^{n} e_i^2}{\sum_{i=1}^{n}(y_i - \bar{y})^2}. \tag{6-58}$$

where $e_i = y_i - \hat{y}_i$ is the residual prediction error, y_i is the test set output obtained from the physical simulation model, $\hat{y}_i$ is the predicted output by ANN, n is total number of test data, and $\bar{y}$ is the mean of the test data outputs.

It is noted that the ANN performance and accuracy totally depends on the number of the training data points. Enlarging the initial dataset increases the ANN performance, which eventually results in a more accurate optimization results. On the other hand, generating a large initial dataset is timely and computationally long and expensive. As can be seen, the optimization process could be challenging when the level of electromechanical complexity increases in the harvester design. Additionally, the optimization procedure can get mathematically more complicated by considering more variable design parameters.

Finally, the successfully trained neural network replaces the simulation model. Fig. 6-21 depicts the neural network structure and also shows the design parameters considered for the training and optimization process.

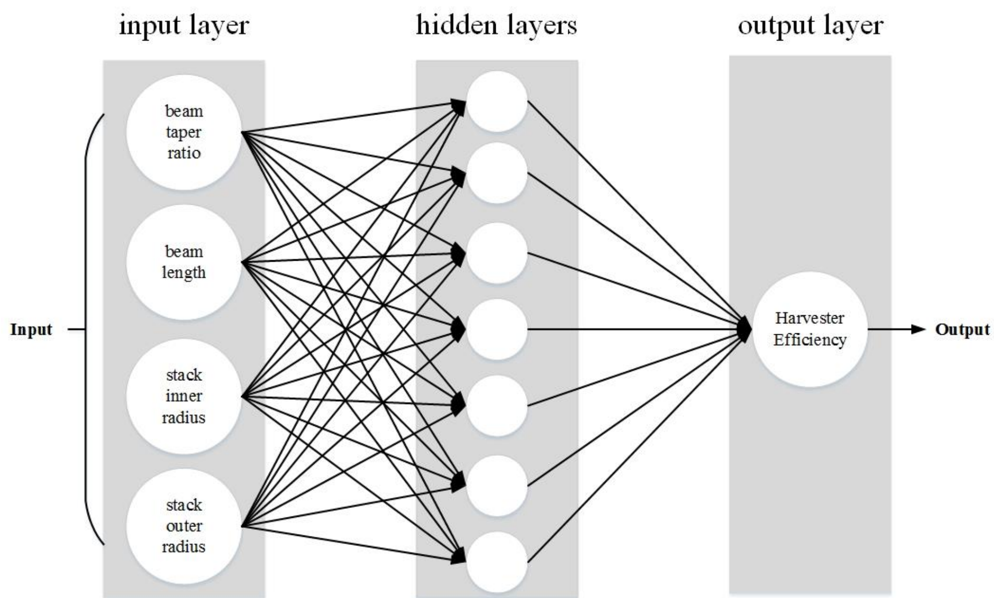

Fig. 6-21 The ANN structure with input and output variables.

Figs. 6-22 and 6-23 show the ANN training regression with two hidden layers and ten neurons for the model with base excitation frequencies φ_1=100rad/s and φ_2=200rad/s. Four plots represent the training, validation, testing, and global data. The dashed lines in the plots show the target result. The solid lines show the best fit linear regression line between output and target. Moreover, *R* is an indication value that expresses the relationship between output and target. When there is an exact linear relationship between output and target, the indication value is one. On the other hand, there is no linear relationship when *R* is close to zero.

As shown in Figs. 6-22 and 6-23, the training data shows a very good fit. In addition, the validation and test results indicate close to one *R* values.

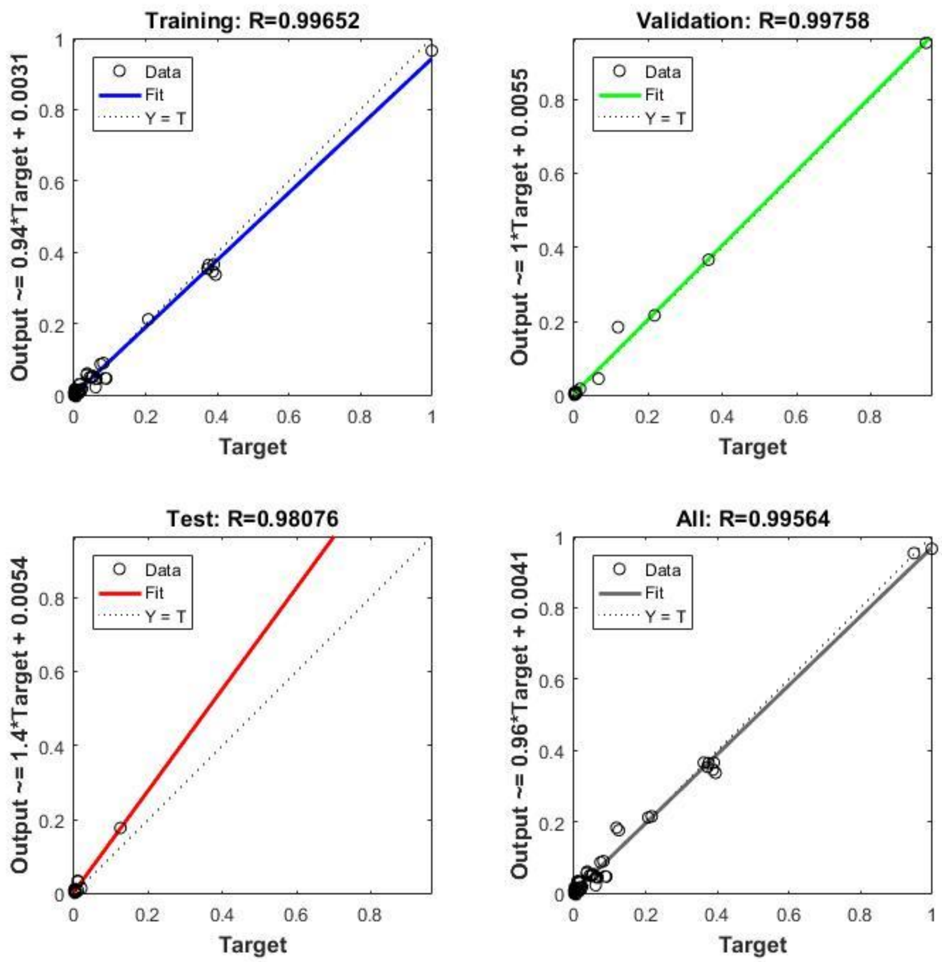

Fig. 6-22 The ANN training regression with base excitation frequency φ_1=100rad/s.

Fig. 6-24 displays the performance functions during ANN training process. The train, validation, and test curves are very close which indicates that the ANN is successfully trained for two design cases.

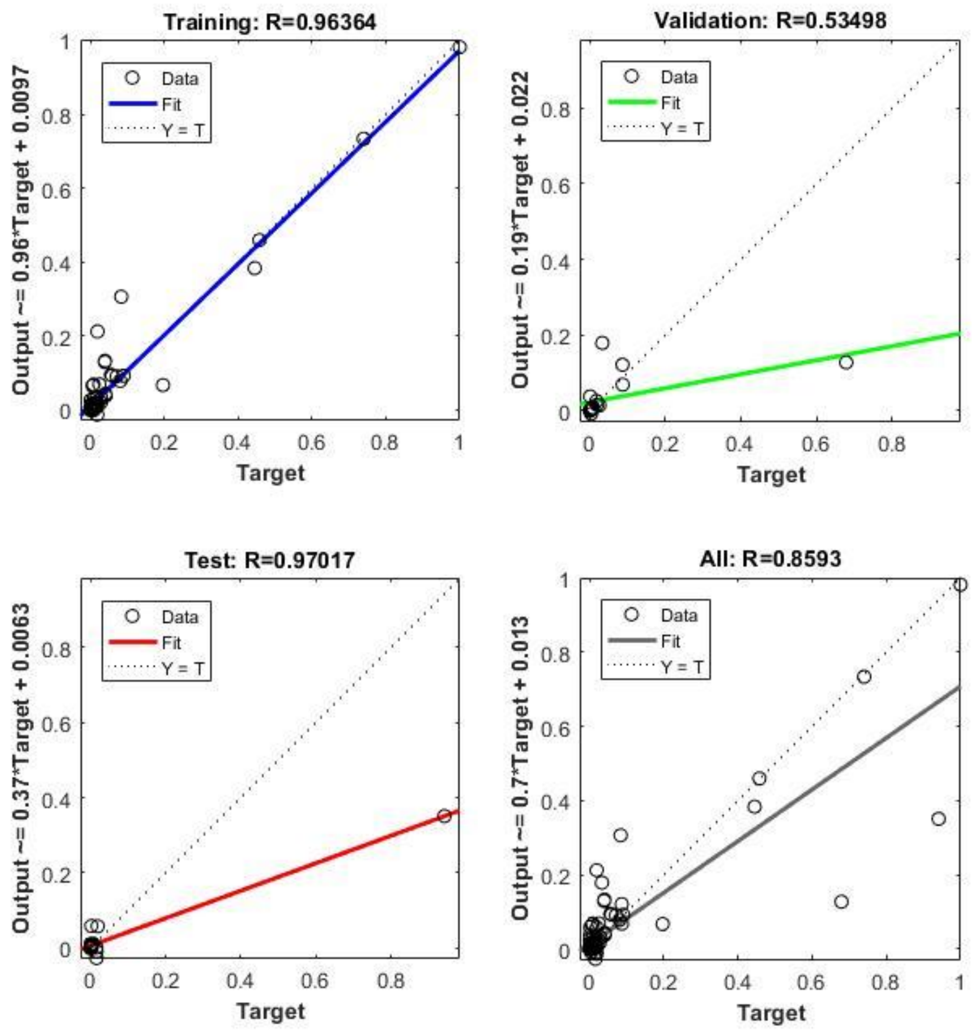

Fig. 6-23 The ANN training regression with base excitation frequency φ_2=200rad/s.

Lastly, the performance comparison between ANN predictions and numerical simulation results is represented in Fig. 6-25. As can be seen, the neural network perfectly predicts the test set simulation outputs for two design cases.

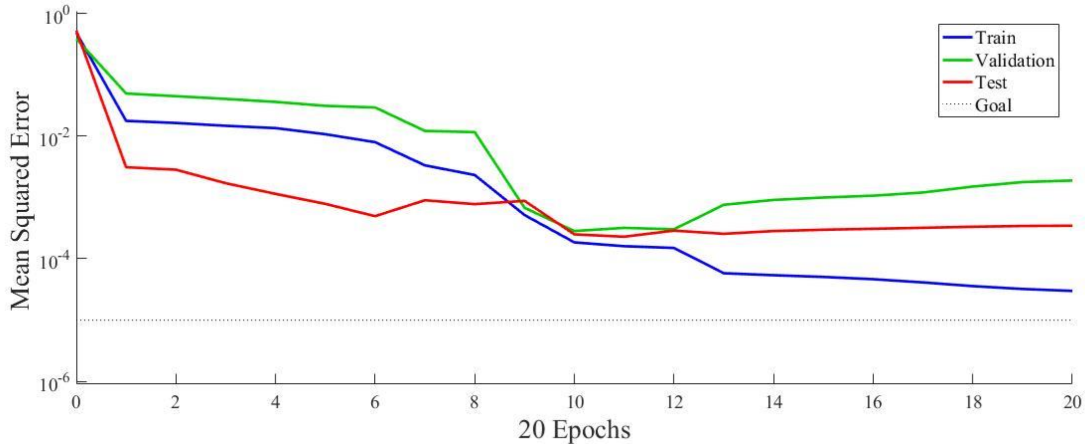

(a)

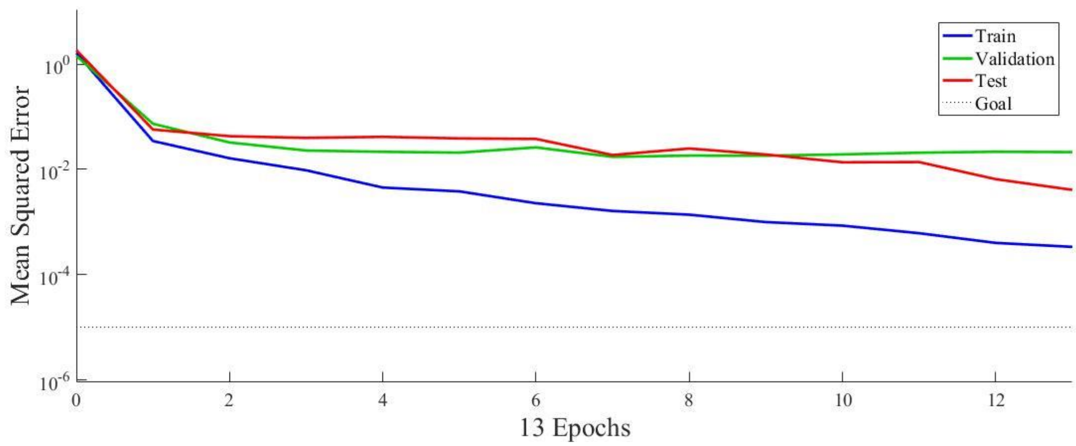

(b)

Fig. 6-24 Performance functions during ANN training. (a) Base excitation frequency φ_1=100rad/s. (b) Base excitation frequency φ_2=200rad/s.

As a conclusion for the ANN training part, four approaches can be followed to improve the training results [143].

1. Initializing the network and the training again. In a feedforward network, parameters are different each time and might generate different output.

2. Increasing the number of hidden neurons. Generally, more neurons in the hidden layer give more flexibility to the ANN because it has more parameters to optimize.

3. Trying a different training function.

4. Providing additional training data.

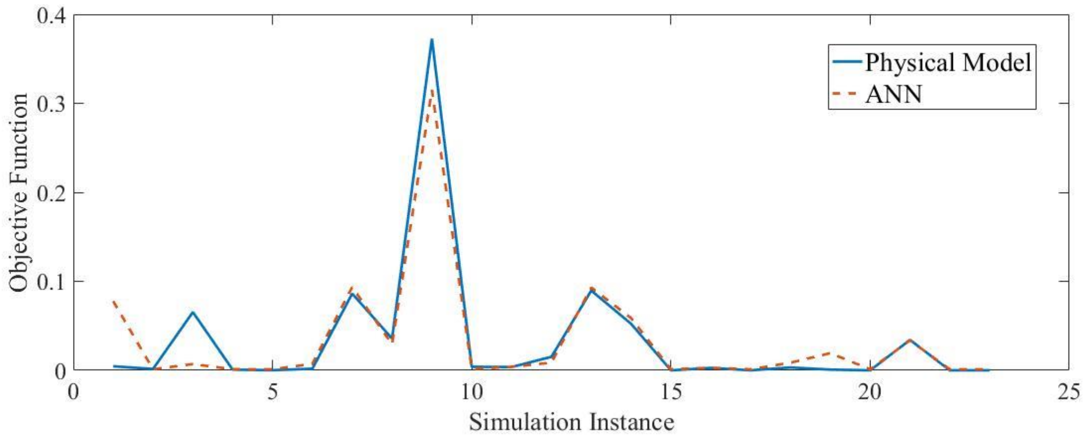

(a)

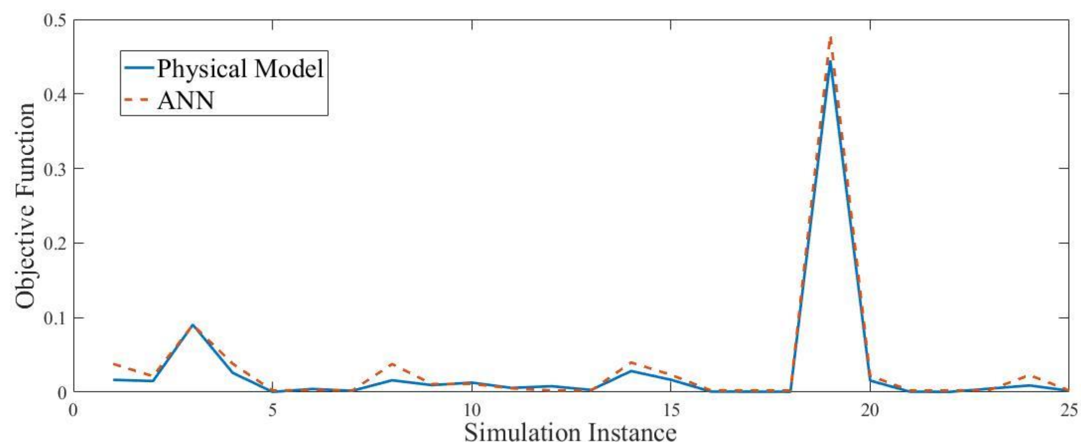

(b)

Fig. 6-25 ANN and numerical simulation performance comparison. (a) Base excitation frequency φ_1=100rad/s. (b) Base excitation frequency φ_2=200rad/s.

Once the ANN is successfully trained, it replaces the simulation model in the GA optimization procedure. This simulation model substitution simply changes the optimization running time from weeks to seconds. In addition, there is no doubt that the required computational power is much less too.

Based on [142] and as shown in Fig. 6-19, the first step is the coding of optimization parameters into genes and chromosomes. Generally, this step deals with arrangement of optimization parameters or chromosomes in a systematic way. For the optimization problem here, four optimization parameters consisting of beam taper ratio, beam length, piezoelectric ring inner radius, and piezoelectric ring outer radius are considered. These parameters are chosen because they have considerably greater influence on the energy harvester performance. Besides, ambient vibration parameters such as vibration amplitude and frequency are not involved in the optimization problem because the designer cannot control these environmental parameters.

The next step is creating the initial population from huge number of chromosomes. The objective function is then evaluated for each chromosome. The outputs and the corresponding chromosome are ranked and the best candidates are chosen through natural selection. Here, natural selection rate of 50% is selected. It means that at each iteration, half of the chromosomes with the highest efficiencies are nominated to continue to the next step. It is noted that better performance means higher ANN efficiency outputs. Due to the large random quantity of the dataset, the chance of finding the global extremum is high. Obviously, larger initial population has better chance of finding the optimization solution.

As the GA process continues, pairing, mating, and mutation happens and the population decreases. In order to prevent the convergence to a local solution, a 5% portion of the population is mutated to search new traits. Finally, at some point, the objective function satisfies the stopping criteria and the GA gives the optimized variables. The GA convergence graph toward a global solution is plotted in Fig. 6-26 for two design cases.

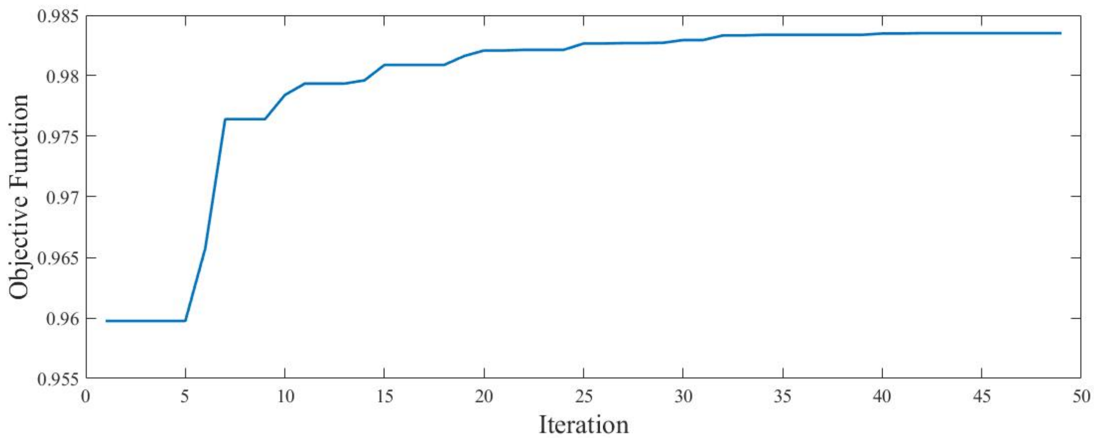

(a)

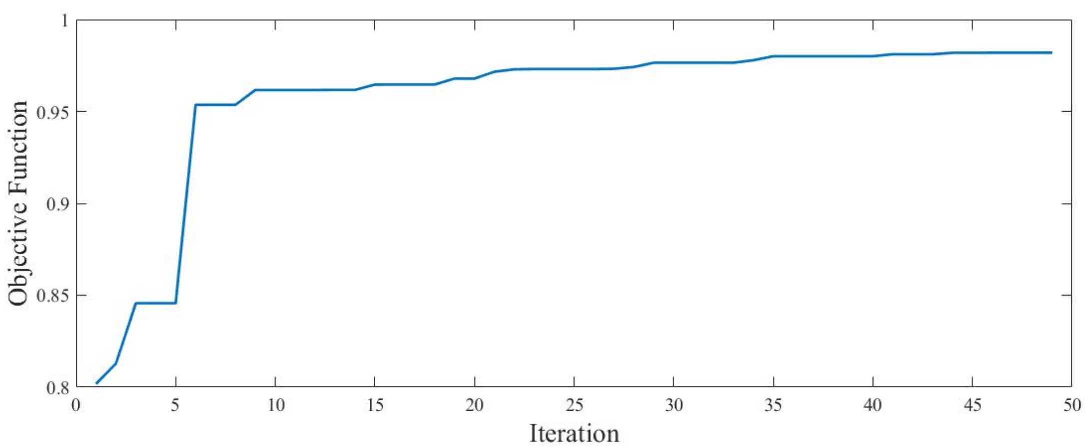

(b)

Fig. 6-26 GA convergence graph. (a) Base excitation frequency φ_1=100rad/s. (b) Base excitation frequency φ_2=200rad/s.

The optimized design parameters evaluated from the GA for two optimization cases are tabulated in Table 6-5. As can be seen, the reported optimized values for taper ratio, beam length, and piezoelectric ring size are completely dependent on the ambient vibration frequency. For lower excitation frequencies ($\varphi \approx 100$rad/s), higher nonlinearity in the design delivers better energy harvesting efficiency. The higher geometrical non-uniformity and length of the beam lowers the structure natural frequency and generates larger bending moment that directly applies to the piezoelectric stacks and produces higher power output. In contrast, for higher excitation frequencies ($\varphi \approx 200$rad/s), a structure with smaller nonlinearity generates more electrical power. The lower geometrical non-uniformity and smaller length of the beam increases the structure natural frequency to match the ambient frequency. Last of all, radius of the beam cross-section was not considered as an independent parameter in the design since the volume of the structure was set to be a constant value in all possible configurations. By considering the constant piezoelectric material volume used for the energy generation, the power density generated from the optimized piezoelectric patch is 576.179W/m^3 or 0.074W/kg.

Table 6-5 GA optimization setting and results.

<table>
<tr><td colspan="7">Excitation frequency φ_1=100rad/s</td></tr>
<tr><td colspan="4">Artificial neural network parameters</td><td colspan="3">Genetic algorithm parameters</td></tr>
<tr><td>Dataset</td><td>Hidden layers</td><td>Neurons</td><td>R^2</td><td>Initial population</td><td>Mutation rate</td><td>Maximum iteration</td></tr>
<tr><td>100</td><td>2</td><td>10</td><td>0.9081</td><td>1000</td><td>5%</td><td>50</td></tr>
<tr><td colspan="7">Optimized design values</td></tr>
<tr><td>Taper ratio</td><td>Length (m)</td><td>Inner radius (m)</td><td>Outer radius (m)</td><td>Power RMS (μW)</td><td colspan="2">Efficiency</td></tr>
<tr><td>0.3</td><td>0.55</td><td>0.002</td><td>0.005</td><td>4.8395</td><td colspan="2">0.000072</td></tr>
<tr><td colspan="7">Excitation frequency φ_2=200rad/s</td></tr>
<tr><td colspan="4">Artificial neural network parameters</td><td colspan="3">Genetic algorithm parameters</td></tr>
<tr><td>Dataset</td><td>Hidden layers</td><td>Neurons</td><td>R^2</td><td>Initial population</td><td>Mutation rate</td><td>Maximum iteration</td></tr>
<tr><td>100</td><td>2</td><td>10</td><td>0.9854</td><td>1000</td><td>5%</td><td>50</td></tr>
<tr><td colspan="7">Optimized design values</td></tr>
<tr><td>Taper ratio</td><td>Length (m)</td><td>Inner radius (m)</td><td>Outer radius (m)</td><td>Power RMS (μW)</td><td colspan="2">Efficiency</td></tr>
<tr><td>0.1</td><td>0.45</td><td>0.002</td><td>0.005</td><td>15.1973</td><td colspan="2">0.000023</td></tr>
</table>

6.4.4 Conclusion

This section of the thesis presented the analytical model and optimized design of a new energy harvesting system. The steady state vibration response of the harvester platform subjected to a harmonic base motion was obtained and electrical outputs were analytically derived. Moreover, the in-plane polarization of the piezoelectric materials was used to maximize the energy harvesting efficiency. Finally, machine-learning models were developed to find the optimum mechanical design following the simulation-based optimization technique.

Since the running procedure of the presented simulation model was very complex and expensive in terms of time and computation power, a properly trained feedforward backpropagation ANN replaced the simulation model. A training set was generated, randomly shuffled, and loaded to train the neural network. Then, a test set was used to evaluate the performance of the trained ANN. As the final point, the properly trained neural network replaced the physical simulation model. Finally, the GA was employed to find the global optimized design parameters.

For the proposed energy harvesting platform optimization problem, beam taper ratio, beam length, and piezoelectric ring size were selected as the optimization parameters. These parameters were chosen because they have significantly superior effect on the energy harvester performance. Moreover, ambient vibration parameters such as vibration amplitude and frequency are not involved in the optimization problem because the designer cannot control these environmental parameters. It was demonstrated that the optimal values of the design parameters completely depends on the ambient vibration parameters. Considering a specific ambient vibration characteristics, the presented model can deliver the optimum design of the piezoelectric energy harvester platform to generate the highest possible electrical power.

6.5 Summary and Conclusion

This chapter of the thesis presented the theoretical development of four different piezoelectric energy harvesting systems. First, the electromechanical solution of a nonlinearly tapered FGM cantilever energy harvester was analytically presented. It was demonstrated that the new non-uniform configuration of the piezoelectric harvester results in higher electrical outputs compared to the conventional uniform ones. Then the non-uniform harvester concept was used to configure a wideband energy harvesting system. This novel wideband harvesting system was the combination of multiple non-uniform bimorphs with identical mass, volume, and length that significantly increased the electrical outputs. Afterward, a composite energy harvester with embedded piezoelectric stacks was investigated to benefit from the more desirable in-plane piezoelectric polarization mode. Depending on the electrical requirements, greater electric charge or voltage can be produced by using the recommended configuration. Lastly, the optimum design of an energy harvesting platform system by stacking up piezoelectric rings in the boundary of a non-uniform beam with machine-learning models was presented. The piezoelectric stack design inside the platform can help to realize the larger strain values and subsequently harvest more electrical power.

Chapter 7

7 Conclusions and Future Works

Dynamic analysis of non-uniform structures in an effort to achieve a superior design and optimize weight and strength has been of interest for many years and is still receiving attention. To model and derive the dynamic response of such a design, a powerful mathematical method is required. Once the mathematical method is developed and the dynamic behavior is accurately modeled, it can be used to study the vibration and stability of non-uniform piezoelectric coupled structures.

In this research, an analytical model to solve the vibration of non-uniform slender beams with general geometry and FGM variation profiles is presented for the first time in the literature. Then, this effective methodology is employed to study the stability enhancement and energy harvesting of piezoelectric coupled non-uniform structures. It has been demonstrated that non-uniform piezoelectric coupled geometry of the beam not only fulfils architectural and functional design requirements, but also significantly increases the system stability. On the other hand, the new non-uniform configuration has proved to be capable of considerably increasing the electromechanical outputs of the piezoelectric energy harvester in a wide frequency domain.

7.1 Thesis Summary and Conclusions

In this thesis, an analytical model for the vibration analysis of nonlinearly tapered beams with axially FGM properties subjected to general boundary conditions within the Euler–Bernoulli beam theory framework valid for any slender beam was provided. The effects of geometry and material properties variation were comprehensively investigated. For various non-uniform beams, natural frequencies and corresponding vibration mode shape functions were calculated. Furthermore, efficiency and effectiveness of the methodology were confirmed by experimental test and comparison with existing numerical results. It is noted that due to some technical limitations and lack of necessary equipment, it was not possible to experimentally validate the vibration mode shapes of the nonlinearly tapered beam. However, the very small error (less than 3%) comparing the first two natural frequencies calculated from experiment and theory clearly demonstrates the accuracy and precision of the presented model.

Next, it was demonstrated that piezoelectric layers and their coupling effect in addition to the non-uniform geometry, significantly enhance the stability of the structure. Effects of compressive follower force, geometry taper ratio, boundary condition, and external piezoelectric voltage on flutter and buckling capacities of non-uniform piezoelectric coupled beams were thoroughly examined. According to the presented numerical studies, the non-uniform design could have higher flutter and buckling capacities for different restraint degrees at the boundary. In other words, a non-uniform piezoelectric coupled beam with lighter mass can deliver identical flutter and buckling capacities to that of a uniform one. It is noted that the presented model is applicable to beams with continuous profile variation. As a result, local damage or buckling in the structure cannot be modelled and analyzed.

The model was also used to analytically develop a non-uniform piezoelectric energy harvester. It was applied to surface bonded piezoelectric beams with non-uniform geometry and material variation profiles to derive the dynamic response of the structure to external environmental excitations and harvest the subsequent mechanical vibration energy. Based on the parametric study, effects of non-uniform geometry, FGM variation profile, and excitation frequency on the voltage output and beam tip displacement FRFs were studied. It was proved that the new non-uniform configuration increases the electromechanical outputs.

Moreover, a group of non-uniform harvesters was used to configure a wideband piezoelectric energy harvesting system. It was demonstrated that with the proposed combination of multiple nonlinearly tapered beams with slight variation in the geometry profile but the same volume, mass, and length, the system could effectively and optimally function over a wide frequency range and also increase the electrical outputs.

Then, a new composite energy harvester with embedded piezoelectric stacks was presented. In order to increase the electrical outputs, the in-plane polarization of the piezoelectric elements was used. The steady state vibration response of the composite harvester subjected to a harmonic base motion was obtained and electrical outputs were analytically derived. Effects of embedded piezoelectric stacks number, length, and thickness in a wide frequency domain were studied. The comparison of results proved better electrical outputs of the proposed design.

Lastly, the optimum design of an energy harvesting platform by stacking up piezoelectric rings in the boundary of a non-uniform beam was presented. By using the in-plane polarization, the piezoelectric stack design inside the platform can help to realize larger strain values and subsequently generate higher electrical power. The optimization process was performed by using ANN and GA. It is noted that the precision of the optimization results completely depends on the number of the training data points collected. Enlarging the initial dataset improves the ANN performance that ultimately results in a more accurate optimization outputs. On the other hand, producing a big enough primary dataset is timely and computationally expensive. Therefore, the optimization process could be challenging when the level of electromechanical complexity increases in the design. Moreover, optimization procedure can get mathematically more difficult by considering more variable design parameters.

One last important thing to consider is the manufacturing process. Obviously, producing beams with variable cross-sectional profile has some manufacturing challenges. However, it was proved that a non-uniform beam/column with lighter mass can deliver identical flutter and buckling capacities to that of a uniform one. Moreover, in the case of piezoelectric energy harvesting, improved power density for the proposed non-uniform configurations was shown. Still, attaching piezoelectric patches on surface of the beam's variable profile could be puzzling. One easy way to solve this problem could be using small piezoelectric elements with higher flexibility.

7.2 Future Works

This thesis presented a very powerful mathematical model to solve partial differential equations with nonlinear variable coefficients. The model was used to derive the dynamic response of non-uniform beams within the framework of Euler–Bernoulli theory. Undoubtedly, the mathematical approach can be further developed for advanced beam theories such as Timoshenko beams and even more complex engineering structures such as plates and shells. Therefore, more theoretical and mathematical improvements can be made in order to optimize and further advance the analytical model presented in this thesis.

The proposed non-uniform configuration coupled with piezoelectric materials demonstrated better characteristics compared to a conventional uniform design in terms of stability and energy harvesting. For different geometries, material properties, loading patterns, boundary conditions, and engineering applications, various machine learning techniques and approaches can be utilized to find the optimized configuration in order to considerably enhance the structural stability or increase the energy harvesting efficiency.

In addition, the effect of non-uniform design on the local damage and buckling issues can be modelled and investigated by using the method of discrete beam sections. Future studies on this subject can help to further examine impact or high frequency dynamic axial direction loading scenarios.

For the sake of simplicity in the optimization process of the proposed multi-stacked energy harvester platform, only four design parameters were selected. Several other variable design parameters such as layer number and thickness in addition to ambient vibration parameters could also be involved in the optimization problem. Moreover, the power efficiency factor can be replaced by other objective functions such as energy density. Last but not least, other training methods and optimization models can be employed to study the problem and compare the optimized output results.

Lastly, the transient charging process, storage units, and harvesting circuits can be modelled and designed to complete the harvesting system and make use of the regenerated energy. Additionally, further experimental studies can be performed to evaluate the designed non-uniform harvesters and assess system manufacturing, assembly, and integration.

References

[1] A. Keshmiri, N. Wu and Q. Wang, "Vibration analysis of a nonlinearly tapered cone beam using Adomian decomposition method," *International Journal of Structural Stability and Dynamics,* vol. 18, no. 07, p. 1850101, 2018.

[2] G. Kirchhoff, "Uber die Transversalschwingungen eines Stabes yon veranderlichem Ouerschnitt," *Mber. Akad. Wiss. Berlin,* 1879.

[3] J. Morrow, "On the Lateml Vibration of Bars of Uniform and Varying Sectional Area," *Proceedings of the Physical Society of London,* vol. 19, pp. 588-602, 1903.

[4] E. W. Suppiger and N. J. Taleb, "Free Lateral Vibration of Beams of Variable Cross Section," *Journal of Applied Mathematics and Physics,* vol. 7, no. 6, pp. 501-520, 1956.

[5] J. H. Gaines and E. Volterra, "Transverse Vibrations of Cantilever Bars of Variable Cross Section," *Journal of Acoustical Society of America,* vol. 39, no. 4, pp. 674-679, 1965.

[6] E. T. Cranch and A. A. Adler, "Bending Vibration of Variable Section Beams," *Journal of Applied Mechanics,* vol. 34, pp. 702-708, 1967.

[7] H. H. Mabie and C. B. Rogers, "Transverse vibrations of double-tapered cantilever beams with end support and with end mass," *Journal of the Acoustical Society of America,* vol. 55, pp. 986-991, 1974.

[8] L. Klein, "Transverse Vibrations of Non-Uniform Beams," *Journal of Sound and Vibration,* vol. 37, no. 4, pp. 491-505, 1974.

[9] O. O. Ozgumus and M. O. Kaya, "Energy expressions and free vibration analysis of a rotating double tapered Timoshenko beam featuring bending–torsion coupling," *International Journal of Engineering Science,* vol. 45, p. 562–586, 2007.

[10] A. K. Gupta, "Vibration of Tapered Beams," *Journal of Structural Engineering,* vol. 111, no. 1, pp. 19-36, 1985.

[11] S. Y. Lee, H. Y. Ke and Y. H. Kuo, "Analysis of non-uniform beam vibration," *Journal of Sound and Vibration,* vol. 142, no. 1, pp. 15-29, 1990.

[12] S. Naguleswaran, "A Direct Solution for the Transverse Vibration of Euler-Bernoulli Wedge and Cone Beams," *Journal of Sound and Vibration,* vol. 172, no. 3, pp. 289-304, 1994.

[13] S. H. Ho and C. K. Chen, "Analysis of general elastically end restrained non-uniform beams using differential transform," *Applied Mathematical Modelling,* vol. 22, no. 3-4, pp. 219-234, 1998.

[14] A. R. Sahu, "2000 Theoretical Frequency Equation of Bending Vibrations of an Exponentially Tapered Beam Under Rotation," *Journal of Vibration and Control*, vol. 7, no. 6, pp. 775-780, 2001.

[15] C. Y. Wang and C. M. Wang, "Exact Vibration Solution for Exponentially Tapered Cantilever With Tip Mass," *Journal of Vibration and Acoustics*, vol. 134, no. 4, pp. 041012(1-4), 2012.

[16] D. Garijo, "Free Vibration Analysis of Non-Uniform Euler-Bernoulli Beams by Means of Bernstein Pseudospectral Collocation," *Engineering with Computers*, vol. 31, no. 4, pp. 813-823, 2015.

[17] S. Karparvarfard, M. Asghari and R. Vatankhah, "A geometrically nonlinear beam model based on the second strain gradient theory," *International Journal of Engineering Science*, vol. 91, pp. 63-75, 2015.

[18] G. Adomian, Solving Frontier Problems of Physics: The Decomposition Method, Boston, MA: Academic Publisher, 1994.

[19] J. C. Hsu, H. Y. Lai and C. K. Chen, "Free vibration of non-uniform Euler–Bernoulli beams with general elastically end constraints using Adomian modified decomposition method," *Journal of Sound and Vibration*, vol. 318, no. 4-5, pp. 965-981, 2008.

[20] H. Y. Lai, J. C. Hsu and C. K. Chen, "An Innovative Eigenvalue Problem Solver for Free Vibration of Euler-Bernoulli Beam by Using the Adomian Decomposition Method," *Computers and Mathematics with Applications*, vol. 56, no. 12, pp. 3204-3220, 2008.

[21] Q. Mao, "Free Vibration Analysis of Multi-Stepped Beams by Using Adomian Decomposition Method," *Mathematical and Computer Modelling*, vol. 54, no. 1-2, pp. 756-764, 2011.

[22] A. Keshmiri, N. Wu and Q. Wang, "Vibration analysis of non-uniform tapered beams with nonlinear FGM properties," *Journal of Mechanical Science and Technology*, vol. 32, no. 11, p. 5325–5337, 2018.

[23] C. T. Loy, K. Y. Lam and J. N. Reddy, "Vibration of functionally graded cylindrical shells," *International Journal of Mechanical Sciences*, vol. 41, p. 309–324, 1999.

[24] J. Ying, C. F. Lu and W. Q. Chen, "Two-dimensional elasticity solutions for functionally graded beams resting on elastic foundations," *Composite Structures*, vol. 84, p. 209–219, 2008.

[25] S. A. Sina, H. M. Navazi and H. Haddadpour, "An analytical method for free vibration analysis of functionally graded beams," *Materials and Design*, vol. 30, p. 741–747, 2009.

[26] X. F. Li, "A unified approach for analyzing static and dynamic behaviors of functionally graded Timoshenko and Euler–Bernoulli beams," *Journal of Sound and Vibration*, vol. 318, p. 1210–1229, 2008.

[27] X. F. Li, Y. F. Kang and J. X. Wu, "Exact frequency equations of free vibration of exponentially

functionally graded beams," *Applied Acoustics,* vol. 74, p. 413–420, 2013.

[28] M. Aydogdu, "Semi-inverse Method for Vibration and Buckling of Axially Functionally Graded Beams," *Journal of Reinforced Plastics and Composites,* vol. 27, no. 7, pp. 683-691, 2008.

[29] I. Elishakoff and S. Candan, "Apparently first closed-form solution for vibrating: inhomogeneous beams," *International Journal of Solids and Structures,* vol. 38, pp. 3411-3441, 2001.

[30] Y. Huang and X. F. Li, "A new approach for free vibration of axially functionally graded beams with non-uniform cross-section," *Journal of Sound and Vibration,* vol. 329, p. 2291–2303, 2010.

[31] A. Shahba, R. Attarnejad, M. Tavanaie Marvi and S. Hajilar, "Free vibration and stability analysis of axially functionally graded tapered Timoshenko beams with classical and non-classical boundary conditions," *Composites: Part B,* vol. 42, pp. 801-808, 2011.

[32] A. E. Alshorbagy, M. A. Eltaher and F. F. Mahmoud, "Free vibration characteristics of a functionally graded beam by finite element method," *Applied Mathematical Modelling,* vol. 35, pp. 412-425, 2011.

[33] A. Shahba and S. Rajasekaran, "Free vibration and stability of tapered Euler–Bernoulli beams made of axially functionally graded materials," *Applied Mathematical Modelling,* vol. 36, p. 3094–3111, 2012.

[34] J. Fang and D. Zhou, "Free vibration analysis of rotating axially functionally graded-tapered beams using Chebyshev–Ritz method," *Materials Research Innovations,* vol. 19, pp. 1255-1262, 2015.

[35] H. Li, C. Tian and D. Z. Deng, "Energy harvesting from low frequency applications using piezoelectric materials," *Applied Physics Reviews,* vol. 1, p. 041301, 2014.

[36] S. R. Anton and H. A. Sodano, "A review of power harvesting using piezoelectric materials," *Smart Materials and Structures,* vol. 16, pp. 1-21, 2007.

[37] J. Sirohi and I. Chopra, "Fundamental understanding of piezoelectric strain sensors," *Journal of Intelligent Material Systems and Structures,* vol. 11, pp. 246-257, 2000.

[38] N. G. Elvin, A. A. Elvin and M. Spector, "A self-powered mechanical strain energy sensor," *Smart Materials and Structures,* vol. 10, pp. 293-299, 2001.

[39] D. J. Inman, J. J. Dosch and E. Garcia, "A Self-Sensing Piezoelectric Actuator for Collocated Control," *Journal of Intelligent Materials and Smart Structures,* vol. 3, pp. 166-185, 1992.

[40] B. Z. Janos and N. w. Hagood, "Overview of active fiber composites technologies," in *6th International Conference on New Actuators*, Bremen, 1998.

[41] R. B. Williams, G. Park, D. J. Inman and W. K. Wilkie, "An overview of composite actuators with

piezoceramic fibers," in *IMAC-XX: Conf. on Structural Dynamics,* Los Angeles, 2002.

[42] X. J. Lin, K. C. Zhou, X. Y. Zhang and D. Zhang, "Development, modeling and application of piezoelectric fiber composites," *Transactions of Nonferrous Metals Society of China,* vol. 23, no. 1, pp. 98-107, 2013.

[43] H. A. Sodano, J. Lloyd and D. J. Inman, "An experimental comparison between several active composite actuators for power generation," *Smart Materials and Structures,* vol. 5, p. 1211–1216, 2006.

[44] IEEE, IEEE Standard on Piezoelectricity, New York: IEEE, 1987.

[45] E. F. Crawley and J. de Luis, "Use of piezoelectric actuators as elements of intelligent structures," in *Structural Dynamics and Materials Conference*, San Antonio, TX, US, 1986.

[46] A. Keshmiri, N. Wu and Q. Wang, "A new nonlinearly tapered FGM piezoelectric energy harvester," *Engineering Structures,* vol. 173, pp. 52-60, 2018.

[47] V. Bolotin, Nonconservative problems of the theory of elastic stability, London: Pergamon press, 1963.

[48] O. Seresta, "Buckling, flutter, and postbuckling optimization of composite structures," Virginia Polytechnic Institute and State University, Blacksburg, Virginia, 2007.

[49] Q. Wang and S. Quek, "Enhancing flutter and buckling capacity of column by piezoelectric layers," *International Journal of Solids and Structures,* vol. 39, pp. 4167-4180, 2002.

[50] A. Keshmiri and N. Wu, "Structural stability enhancement by nonlinear geometry design and piezoelectric layers," *Journal of Vibration and Control,* 2018.

[51] R. Ahuja and R. Duffield, "Parametric instability of variable cross-section beams resting on an elastic foundation," *Journal of Sound and Vibration,* vol. 39, no. 2, pp. 159-174, 1975.

[52] M. O'rourke and T. Zebrowski, "Buckling load for nonuniform columns," *Computers and Structures,* vol. 7, pp. 717-720, 1977.

[53] H. Matsuda, T. Sakiyama and C. Morita, "Variable cross sectional Beck's column subjected to nonconservative load," *Journal of Applied Mathematics and Mechanics,* vol. 73, no. 12, pp. 383-385, 1993.

[54] Q. Li, "Non-conservative stability of multi-step non-uniform columns," *International Journal of Solids and Structures,* vol. 39, no. 9, pp. 2387-2399, 2002.

[55] A. Leung, "Dynamic axial-moment buckling of linear beam systems by power series stiffness," *Journal of Engineering Mechanics ASCE,* vol. 135, no. 8, pp. 852-861, 2009.

[56] L. Marques, A. Taras, L. Simoes da Silva, R. Greiner and C. Rebelo, "Development of a consistent buckling design procedure for tapered columns," *Journal of Constructional Steel Research,* vol. 72, p. 61–74, 2012.

[57] Z. Lei and T. Shu, "Lateral buckling of web-tapered I-beams: A new theory," *Journal of Constructional Steel Research,* vol. 64, p. 1379–1393, 2008.

[58] A. Beyer, Y. Galea, A. Bureau and N. Boissonnade, "Elastic stability of uniform and non-uniform members with arbitrary boundary conditions and intermediate lateral restraints," in *Annual Stability Conference Structural Stability Research Council,* Nashville, Tennessee, 2015.

[59] D. Karabalis and D. Beskos, "Static, dynamic and stability analysis of structures composed of tapered beams," *Computers and Structures,* vol. 16, no. 6, pp. 731-748, 1983.

[60] M. Eisenberg and Y. Reich, "Static, vibration and stability of non-uniform beams," *Computers and Structures,* vol. 31, no. 4, pp. 567-573, 1989.

[61] H. Ozturk, I. Yesilyurt and M. Sabuncu, "In-plane stability analysis of non-uniform cross-sectioned curved beams," *Journal of Sound and Vibration,* vol. 296, p. 277–291, 2006.

[62] T. Irie, G. Yamada and I. Takahashi, "Vibration and stability of a non-uniform Timoshenko beam subjected to a follower force," *Journal of Sound and Vibration,* vol. 70, no. 4, pp. 503-512, 1980.

[63] E. Esmailzadeh and A. Ohadi, "Vibration and stability analysis of non-uniform Timoshenko beams under axial and distributed tangential loads," *Journal of Sound and Vibration,* vol. 236, no. 3, pp. 443-456, 2000.

[64] N. Auciello and A. Ercolano, "A general solution for dynamic response of axially loaded non-uniform Timoshenko beams," *International Journal of Solids and Structures,* vol. 41, no. 18-19, pp. 4861-4874, 2004.

[65] Q. Wang, "A comprehensive stability analysis of a cracked beam subjected to follower compression," *International Journal of Solids and Structures,* vol. 41, p. 4875–4888, 2004.

[66] N. Wu and Q. Wang, "Repair of vibrating delaminated beam structures using piezoelectric patches," *Smart Materials and Structures,* vol. 19, no. 3, pp. 1-8, 2010.

[67] Q. Wang and N. Wu, "A review on structural enhancement and repair using piezoelectric materials and shape memory alloys," *Smart Materials and Structures,* vol. 21, pp. 1-23, 2012.

[68] H. S. Kim, J. H. Kim and J. Kim, "A review of piezoelectric energy harvesting based on vibration," *International Journal of Precision Engineering and Manufacturing,* vol. 12, no. 6, p. 1129–1141, 2011.

[69] S. Roundy, P. K. Wright and J. Rabaey, "A study of low level vibrations as a power source for

wireless sensor nodes," *Computer and Communications,* vol. 26, p. 1131–1144, 2003.

[70] T. Sterken, K. Baert, C. Van Hoof, R. Puers, G. Borghs and P. Fiorini, "Comparative modelling for vibration scavengers," in *IEEE Sensors,* Vienna, 2004.

[71] G. Poulin, E. Sarraute and F. Costa, "Generation of electrical energy for portable devices: comparative study of an electromagnetic and a piezoelectric system," *Sensors Actuators A,* vol. 116, p. 461–471, 2004.

[72] P. Niu, P. Chapman, R. Riemer and X. Zhang, "Evaluation of motions and actuation methods for biomechanical energy harvesting," in *IEEE 35th Annual Power Electronics,* Aachen, 2004.

[73] N. V. Viet, N. Wu and Q. Wang, "A review on energy harvesting from ocean waves by piezoelectric technology," *Journal of Modeling in Mechanics and Materials,* vol. 1, no. 2, pp. 2328-2355, 2017.

[74] S. Roundy, "On the effectiveness of vibration-based energy harvesting," *Journal of Intelligent Material Systems and Structures,* vol. 16, p. 809–823, 2005.

[75] S. Roundy, P. K. Wright and J. Rabaey, "A study of low level vibrations as a power source for wireless sensor nodes," *Computer Communications,* vol. 26, no. 11, pp. 1131-1144, 2003.

[76] M. Stewart, P. M. Weaver and M. Cain, "Charge redistribution in piezoelectric energy harvesters," *Applied Physics Letters,* vol. 100, p. 073901, 2012.

[77] S. Pobering and N. Schwesinger, "Power supply for wireless sensor systems," in *IEEE Sensors,* Lecce, Italy, 2008.

[78] T. Hehn and Y. Manoli, CMOS Circuits for piezoelectric energy harvesters, Netherlands: Springer, 2015.

[79] H. A. Sodano, D. J. Inman and G. Park, "A review of power harvesting from vibration using piezoelectric materials," *The Shock and Vibration Digest,* vol. 36, no. 3, pp. 197-205, 2004.

[80] D. Zhu, M. J. Tudor and S. P. Beeby, "Strategies for increasing the operation frequency range of vibration energy harvesters: a review," *Measurement Science and Technology,* vol. 21, pp. 022001-29, 2010.

[81] A. Keshmiri, X. Deng and N. Wu, "New energy harvester with embedded piezoelectric stacks," *Composites Part B: Engineering,* vol. 163, pp. 303-313, 2019.

[82] M. Umeda, K. Nakamura and S. Ueha, "Analysis of the Transformation of Mechanical Impact Energy to Electric Energy Using Piezoelectric Vibrator," *Japanese Journal of Applied Physics,* vol. 35, pp. 3267-3273, 1996.

[83] C. B. Williams and R. B. Yates, "Analysis of a micro-electric generator for microsystems," *Sensors and Actuators A,* vol. 52, pp. 8-11, 1996.

[84] L. A. Weinstein, M. R. Cacan, P. M. So and P. K. Wright, "Vortex Shedding induced energy harvesting from piezoelectric materials in heating, ventilation and air conditioning flows," *Smart Materials and Structures,* vol. 21, p. 045003, 2012.

[85] J. Ajitsaria, S. Y. Choe, D. Shen and D. J. Kim, "Modeling and analysis of a bimorph piezoelectric cantilever beam for voltage generation," *Smart Materials and Structures,* vol. 16, no. 2, p. 447–454, 2007.

[86] L. Dhakar, H. Liu, F. E. Tay and C. Lee, "A new energy harvester design for high power output at low frequencies," *Sensors and Actuators A: Physical,* vol. 199, pp. 344-352, 2013.

[87] A. Erturk and D. J. Inman, "On mechanical modeling of cantilevered piezoelectric vibration energy harvesters," *Journal of Intelligent Material Systems and Structures,* vol. 19, no. 11, pp. 1311-1325, 2008.

[88] T. J. Johnson, D. Charnegie, W. W. Clark, M. Buric and G. Kusic, "Energy harvesting from mechanical vibrations using piezoelectric cantilever beams," in *Smart Structures and Materials Conference SPIE,* San Diego, 2006.

[89] L. Beker, H. Kulah and A. Muhtaroglu, "Piezoelectric cantilever prototype for energy harvesting in computing applications," in *International Conference on Energy Aware Computing,* Istanbul, 2011.

[90] X. Gao, W. H. Shih and W. Y. Shih, "Vibration energy harvesting using piezoelectric unimorph cantilevers with unequal piezoelectric and nonpiezoelectric lengths," *Applied Physics Letters,* vol. 97, no. 23, p. 233503, 2010.

[91] Y. Minami and E. Nakamachi, "Development of enhanced piezoelectric energy harvester induced by human motion," in *Annual International Conference of the IEEE Engineering in Medicine and Biology Society*, San Diego, 2012.

[92] M. S. Lee, J. S. Yun, W. I. Park, Y. W. Hong, J. H. Cho, J. H. Paik, Y. H. Park, C. M. Son and Y. H. Jeong, "Fabrication and energy harvesting characteristics of unimorph piezoelectric cantilever generators with interdigitated electrode lead zirconate titanate laminates," *Japanese Journal of Applied Physics,* vol. 56, pp. 127101(1-6), 2017.

[93] H. A. Sodano, G. Park and D. J. Inman, "Estimation of Electric Charge Output for Piezoelectric Energy Harvesting," *Journal of Strain,* vol. 40, no. 2, p. 49–58, 2004.

[94] T. H. Ng and W. H. Liao, "Sensitivity Analysis and Energy Harvesting for a Self-Powered Piezoelectric Sensor," *Journal of Intelligent Material Systems and Structures,* vol. 16, no. 10, pp. 785-797, 2005.

[95] S. Jiang, X. Li, S. Guo, Y. Hu, J. Yang and Q. Jiang, "Performance of a piezoelectric bimorph for scavenging vibration energy," *Smart Materials and Structures,* vol. 14, p. 769–74, 2005.

[96] A. Erturk and D. J. Inman, "An experimentally validated bimorph cantilever model for piezoelectric energy harvesting from base excitations," *Smart Materials and Structures,* vol. 18, pp. 025009(1-18), 2009.

[97] S. Priya, C. T. Chen, D. Fye and J. Zahnd, "Piezoelectric Windmill: A Novel Solution to Remote Sensing," *Japanese Journal of Applied Physics,* vol. 44, no. 3, pp. 104-107, 2005.

[98] S. Pobering and N. Schwesinger, "Power supply for wireless sensor systems," in *IEEE Sensors*, Lecce, 2008.

[99] G. W. Taylor, J. R. Burns, S. A. Kammann, W. B. Powers and T. R. Welsh, "The Energy Harvesting Eel: a small subsurface ocean/river power generator," *IEEE Journal of Oceanic Engineering,* vol. 26, no. 4, pp. 539 - 547, 2001.

[100] A. S. Zurkinden, F. Campanile and L. Martinelli, "Wave Energy Converter through Piezoelectric Polymers," in *Proceedings of the COMSOL users conference*, Grenoble, 2007.

[101] S. Roundy, E. S. Leland, J. Baker, E. Carleton, E. Reilly, E. Lai, B. Otis, J. M. Rabaey and P. K. Wright, "Improving power output fpr vibration-based energy scanvengers," *Energy Harvesting and Conservation,* vol. 4, no. 1, pp. 28-36, 2005.

[102] L. Mateu and F. Moll, "Optimum piezoelectric bending beam structures for energy harvesting using shoe inserts," *Journal of Intelligent Material Systems and Structures,* vol. 16, p. 835–845, 2005.

[103] J. Baker, S. Roundy and P. Wright, "Alternative geometries for increasing power density in vibration energy scavenging for wireless sensor networks," in *3rd International Energy Conversion Engineering Conference*, San Francisco, 2005.

[104] M. Goldfarb and L. D. Jones, "On the Efficiency of Electric Power Generation With Piezoelectric Ceramic," *Journal of Dynamic Systems, Measurement, and Control,* vol. 121, no. 3, pp. 566-571, 1999.

[105] S. R. Platt, S. Farritor and H. Haider, "On low-frequency electric power generation with PZT ceramics," *IEEE/ASME Transactions on Mechatronics,* vol. 10, no. 2, p. 240–252, 2005.

[106] S. Adhikari, M. I. Friswell and D. J. Inman, "Piezoelectric energy harvesting from broadband random vibrations," *Smart Materials and Structures,* vol. 18, pp. 115005(1-7), 2009.

[107] Y. Wang, W. Chen and P. Guzman, "Piezoelectric stack energy harvesting with a force amplification frame: Modeling and experiment," *Journal of Intelligent Materials Systems and Structures,* vol. 27, no. 17, pp. 2324-2332, 2016.

[108] X. Wang, Z. Shi, J. Wang and H. Xiang, "A stack-based flex-compressive piezoelectric energy harvesting cell for large quasi-static loads," *Smart Materials and Structures,* vol. 25, pp. 055005(1-8), 2016.

[109] S. Shevtsov and M. Flek, "Random Vibration Energy Harvesting by Piezoelectric Stack Charging the Battery," *Procedia Engineering,* vol. 144, pp. 645-652, 2016.

[110] G. Adomian, "A Review of the Decomposition Method in Applied Mathematics," *Journal of Mathematical Analysis and Applications,* vol. 135, pp. 501-544, 1988.

[111] A. M. Wazwaz, "Analytic Treatment for Variable Coefficient Fourth-Order Parabolic Partial Differential Equations," *Applied Mathematics and Computation,* vol. 123, pp. 219-227, 2001.

[112] G. Adomian and R. Rach, "Noise Terms in Decomposition Series Solution," *Computers & Mathematics with Applications,* vol. 24, no. 11, pp. 61-64, 1992.

[113] A. M. Wazwaz, "A Reliable Modification of Adomian Decomposition Method," *Applied Mathematics and Computation,* vol. 102, pp. 77-86, 1999.

[114] D. Adair and M. Jaeger, "Simulation of tapered rotating beams with centrifugal stiffening using the Adomian decomposition method," *Applied Mathematical Modelling,* vol. 40, p. 3230–3241, 2016.

[115] X. Tong and B. Tabarrok, "Vibration Analysis of Timeshenko Beams with Non-Homogeneity and Varying Cross-Section," *Journal of Sound and Vibration,* vol. 186, no. 5, pp. 821-835, 1995.

[116] M. C. Ece, M. Aydogdu and V. Taskin, "Vibration of a Variable Cross-Section Beam," *Mechanics Research Communications,* vol. 34, pp. 78-84, 2007.

[117] S. Kumar, A. Mitra and H. Roy, "Geometrically nonlinear free vibration analysis of axially functionally graded taper beams," *Engineering Science and Technology, an International Journal,* vol. 18, pp. 579-593, 2015.

[118] A. Shahba, R. Attarnejad and S. Hajilar, "A Mechanical-Based Solution for Axially Functionally Graded Tapered Euler-Bernoulli Beams," *Mechanics of Advanced Materials and Structures,* vol. 20, p. 696–707, 2013.

[119] E. F. Crawley and J. Luis, "Use of piezoelectric actuators as elements of intelligent structures," *The American Institute of Aeronautics and Astronautics,* vol. 25, no. 10, p. 1373–1385, 1987.

[120] Q. Wang, "On buckling of column structures with a pair of piezoelectric layers," *Engineering Structures,* vol. 24, p. 199–205, 2002.

[121] A. Keshmiri and N. Wu, "A wideband piezoelectric energy harvester design by using multiple non-uniform bimorphs," *Vibration,* vol. 1, no. 1, pp. 93-104, 2018.

[122] H. T. Banks and D. J. Inman, "On Damping Mechanisms in Beams," *Transactions of the ASME*, vol. 58, pp. 716-723, 1991.

[123] R. W. Clough and J. Penzien, Dynamics of Structures, New York: John Wiley and Sons, 1975.

[124] T. K. Caughey and M. E. O'Kelly, "Classical normal modes in damped linear dynamic systems," *ASME Journal of Applied Mechanics,* vol. 32, pp. 583-588, 1965.

[125] J. L. Humar, Dynamics of Structures, London, UK: Taylor & Francis Group, 2012.

[126] A. Erturk and D. J. Inman, "A distributed parameter electromechanical model for cantlievered piezoelectric energy harvesters," *Journal of Vibration and Acoustics,* vol. 130, pp. 1-14, 2008.

[127] X. D. Xie, A. Carpinteri and Q. Wang, "A theoretical model for a piezoelectric energy harvester with a tapered shape," *Engineering Structures,* vol. 144, pp. 19-25, 2017.

[128] S. Shahruz, "Design of mechanical band-pass filters for energy scavenging," *Journal of Sound and Vibration,* vol. 292, pp. 987-998, 2006.

[129] B. Xu, R. G. Polcawich, S. Trolier-McKinstry, Y. Ye and L. E. Cross, "Sensing characteristics of in-plane polarized lead zirconate titanate thin films," *Applied Physics Letters,* vol. 75, no. 26, pp. 4180-4182, 1999.

[130] P. Ceramic, "PI Piezo Technology," PI Ceramic GmbH, 2018. [Online]. Available: https://www.piceramic.com/.

[131] H. C. Song, H. C. Kim, C. Y. Kang, H. J. Kim, S. J. Yoon and D. Y. Jeong, "Multilayer piezoelectric energy scavenger for large current generation," *Journal of Electroceramics,* vol. 23, p. 301–304, 2009.

[132] W. Flügge, Stresses in Shells, Berlin: Springer, 1973.

[133] R. V. Rao and V. J. Savsani, Mechanical design optimization using advanced optimization techniques, London: Springer-Verlag, 2012.

[134] Y. Carson and A. Maria, "SIimulation optimization: methods and applications," in *Proceedings of the 29th conference on Winter simulation*, IEEE Computer Society, 1997.

[135] A. T. Nguyen, S. Reiter and P. Rigo, "A review on simulation-based optimization methods applied to building performance analysis," *Applied Energy,* vol. 113, p. 1043–1058, 2014.

[136] U. Karn, "The data science blog," 9 August 2016. [Online]. Available: https://ujjwalkarn.me/2016/08/09/quick-intro-neural-networks/.

[137] D. Guliani, "Own shares in hackernoon," 22 June 2018. [Online]. Available:

https://hackernoon.com/a-hands-on-introduction-to-neural-networks-6a03afb468b1.

[138] F. S. Inc., "Frontline Solvers," 2018. [Online]. Available: https://www.solver.com/training-artificial-neural-network-intro.

[139] R. L. Haupt and S. E. Haupt, Practical genetic algorithms, Hoboken, New Jersey: John Wiley & Sons, INC., 2004.

[140] D. E. Goldberg, Genetic algorithms in seach, optimization & machine learning, US: Addison-Wesley Publishing Company, Inc., 1989.

[141] E. K. Chong and S. H. Zak, "An introduction to optimization," John Wiley & Sons, Inc., US, 2001.

[142] S. Filizadeh, "Optimization-enabled electromagnetic transient simulation," University of Manitoba, Winnipeg, 2004.

[143] T. MathWorks, "MathWorks Documentation," The MathWorks, Inc., 2018. [Online]. Available: https://www.mathworks.com/help/deeplearning/ug/analyze-neural-network-performance-after-training.html.

List of Publications in PhD Research

Journal Papers:

1. A. Keshmiri, N. Wu, Q. Wang "Vibration analysis of a nonlinearly tapered cone beam using Adomian decomposition method", International Journal of Structural Stability and Dynamics, 18(7), 1850101, 2018.
2. A. Keshmiri, N. Wu, Q. Wang "Vibration analysis of non-uniform tapered beams with nonlinear FGM properties", Journal of Mechanical Science and Technology, 32(11), 5325-5337, 2018.
3. A. Keshmiri, N. Wu "Structural stability enhancement by nonlinear geometry design and piezoelectric layers", Journal of Vibration and Control, 25(3) 695–710, 2019.
4. A. Keshmiri, N. Wu, Q. Wang "A new nonlinearly tapered FGM piezoelectric energy harvester", Engineering Structures, 173, 52-60, 2018.
5. A. Keshmiri, N. Wu "A wideband piezoelectric energy harvester design by using multiple non-uniform bimorphs", Vibration, 1(1), 93-104, 2018.
6. A. Keshmiri, X. Deng, N. Wu "New energy harvester with embedded piezoelectric stacks", Composites Part B: Engineering, 163, 303-313, 2019.

Conference Paper:

1. A. Keshmiri, N. Wu "A new mechanical band pass filter design for energy harvesting", CSME-SCGM, Canadian Society of Mechanical Engineers (CSME) International Congress, Toronto, Canada, May 2018.